UNIVERSITY OF GRONINGEN

MASTER THESIS

Metal Enrichment of the Intergalactic Medium in Cold and Warm Dark Matter Cosmologies

Author:
Jonas BREMER

Supervisor:
Dr. Pratika DAYAL

Kapteyn Institute

August 14, 2017

University of Groningen

Abstract

Faculty of Science & Engineering
Kapteyn Institute

Master of Astronomy

Metal Enrichment of the Intergalactic Medium in Cold and Warm Dark Matter Cosmologies

by Jonas BREMER

The nature of dark matter remains a key question in astrophysics, since the current Lambda Cold Dark Matter (ΛCDM) paradigm exhibits a number of discrepancies between predictions of structure on sub-galactic scales and observations. An alternative to CDM is Warm Dark Matter (WDM) consisting of $\mathcal{O}$(keV) particles. In WDM, small scale structure is suppressed resulting in a dearth of low mass $\mathrm{M_h} < 10^9 \mathrm{M_\odot}$ halos. As galaxies residing in low mass halos are effective at polluting the intergalactic medium (IGM) with metals, one naturally expects less metals in the IGM in WDM compared to CDM. Therefore we study the impact of WDM on the metal enrichment of the IGM. In this work we focus on WDM consisting of 1.5 keV particles, as it is this cosmology that harbors a significant dearth of low mass halos. To do this, we use a semi-analytical model in which we explore several feedback scenarios consisting of internal (supernova) and external (ultraviolet) feedback. In both CDM and 1.5 keV WDM, the effect of feedback on the Ultra Violet luminosity function, stellar mass density, ejected gas mass density and eventually on the cosmological mass density of $\mathrm{C_{IV}}$ in the IGM is explored. We find the metal enrichment of the IGM in 1.5 keV WDM to be delayed and accelerated with respect to CDM. In addition, we note that the effect of baryonic feedback is degenerate with the effect of WDM. Observed $\mathrm{C_{IV}}$ densities are only reproduced in the case of CDM without any external feedback, and therefore within the caveats of this model, we can rule out 1.5 keV WDM and all CDM scenarios except the fiducial one.

Contents

Chapter 1

Introduction

At 13.8 billion years back in time, the universe originated in the a big bang shorty after which the universe underwent a phase of rapid expansion, also known as *"inflation"*. At 1 s to 3 min after the big bang, the conditions where such that besides hydrogen, D,^{3}He, ^{4}He and ^{7}Li were formed (Fields, 2011). When the age of the universe reached a few thousand years, it consisted of a hot and dense plasma mainly composed of protons and electrons embedded in a dense radiation field. At this stage the universe was highly opaque to radiation as it scattered with the free electrons. As the universe expanded, the density of the universe reduced as $(1 + z)^3$ and in turn the temperature dropped. When the universe reached an age of approximately 300000 years, it reached a temperature of $T \sim 1000K$ at which the protons and electrons started to combine to form neutral hydrogen (A.Peacock, 2010). The universe started to become more and more neutral and in turn more transparent as a consequence of the rapid decreasing number of free electrons. This era at $z \sim 1100$ is also known as recombination (A.Peacock, 2010). The radiation that emerges after this epoch is referred to as the Cosmic Microwave Background (CMB) and provides valuable information about the very early universe. The CMB has been studied thoroughly over the years (*Cosmic Background*

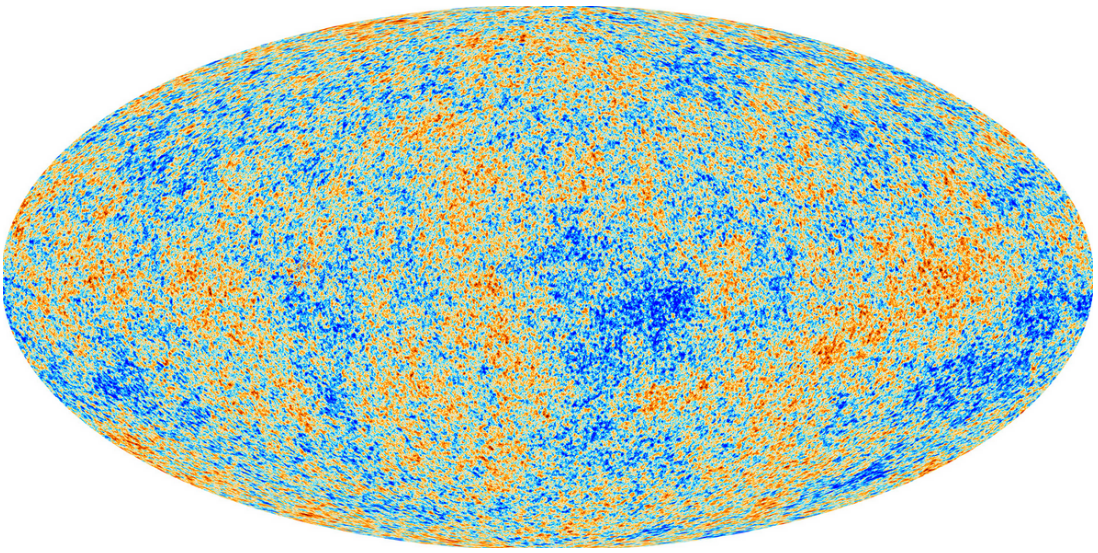

FIGURE 1.1: All sky temperature map the Cosmic Microwave Background measured by Planck (Esa, 2017).

Explorer (COBE), *Wilkinson Microwave Anisotropy Probe* (WMAP)), and an all sky map of the most recent and detailed CMB temperature obtained by the Planck satellite is shown in Figure 1.1. This shows that the early universe was not smooth but already hosted fluctuations. The anisotropies in the CMB have an amplitude of order $\frac{\delta T}{T} \approx 10^{-5}$ and highlight the underlying fluctuations in the density field generated by inflation. The distribution of the fluctuations

suggests a Gaussian distribution, and provides strong evidence for the cosmological principle that states that the universe is homogeneous and isotropic at large scales. These small scale fluctuations are the seeds for the large scale structure observed in the present universe. After the era of recombination, the universe was neutral without any sources producing light because gas not yet started to fall inside dark matter halos to form stars. The absence of any source of light - the *"dark ages"* - ended with the formation of the first stars when the age of the universe was on the order of a few hundred Myrs. Star formation in the first galaxies, produced photons of energy > 1 Rydberg that started to re-ionize the neutral hydrogen present in the universe. Initially each galaxy is surrounded by its own region of ionized hydrogen that is growing over time as the ionization front proceeds further into the neutral IGM. Eventually, ionized regions from individual galaxies will start to overlap. As more galaxies are embedded in a single ionized region, the background of > 1 Rydberg photons is larger. Overlapping of ionized regions will speed up the transition from a neutral to an ionized universe. This phase marks the last global phase transitions of the universe and is called the *"epoch of reionization"*. Observed quasar spectra indicate this is a patchy process (Becker et al., 2015). With time, small structures assemble to form large structures under the force of gravity. As a consequnce, the density contrast between over and under dense regions increases. This result in the formation of large scale filamentary structure -the *cosmic web*- that we observe today (Colless, 1999; Stoughton et al., 2002).

1.1 Lambda Cold Dark Matter (ΛCDM)

The most accepted and widely used cosmological paradigm is the one referred to as Lambda Cold Dark Matter (ΛCDM). In this paradigm, the universe consists mainly of dark matter, baryonic matter and dark energy and originated from a big bang. It contains cold dark matter with an accelerated expansion at $z \leq 1$ related to dark energy (cosmological constant). This paradigm assumes the universe to be homogeneous and isotropic (Friedmann-Robertson-Walker metric) on large scales. The seeds for any structure are the small initial density fluctuations are described by a random Gaussian field. In ΛCDM structure forms hierarchically in which small objects collapse first and the merge together under to force of gravity to form large structures as explained in detail in Section 1.2.

In view of general relativity, the metric for space-time that is spatially homogeneous and isotropic is given by the Friedman-Robertson-Walker metric,

$$ds^2 = c^2dt^2 - a(t)^2(dr^2 + S_k(r)^2[d\theta^2 + sin^2\theta d\phi^2]) \tag{1.1}$$

in which $a(t)$ is the scale factor of the universe (that takes into account the expansion) and (r, θ, ϕ) are spherical co-moving[1] coordinates. This metric can have three different geometries as given by S_k, where

$$S_k(r) = \begin{cases} R_0 sin(\frac{r}{R_0}) & k = +1 \quad closed\ universe\ \ (positive\ curvature) \\ r & k = 0 \quad flat\ universe \quad (zero\ curvature) \\ R_0 sinh(\frac{r}{R_0}) & k = -1 \quad open\ universe\ (negative\ curvature). \end{cases} \tag{1.2}$$

Having a flat universe, results in a specific density that is known as the critical density ρ_{crit} and follows from the Friedman equation that relates the matter energy density of the universe to its expansion. The critical density at any given redshift[2] z is given by

$$\rho_{crit}(z) = \frac{3H^2(z)}{8\pi G} \tag{1.3}$$

[1] Co-moving refers to a quantity that does not change with the expansion of the universe e.g. a physical distance r is related to a co-moving distance x as $r = a(t)x$ in which a is the scale factor.

[2] Redshift is a measure of time of the universe in terms of the expansion of space-time and can be quantified in terms of the wavelength of radiation that expands along with the universe as $\lambda_{obs} = (1 + z)\lambda_{em}$. Time is related to redshift as $t \approx \frac{2}{3H_0\sqrt{\Omega_m(1+z)^3}}$ which is valid for a matter dominated universe, which is justified for high z.

in which $H(z)$ is the Hubble parameter at redshift z and G is the gravitational constant. In cosmology, one often defines the cosmological density (of a component i) in terms on the critical density as

$$\Omega_i = \frac{\rho_i}{\rho_{crit}} \tag{1.4}$$

in which Ω expresses the total matter-energy density of content i. The different contributions are matter Ω_m (both baryonic and dark matter), radiation Ω_r, vacuum energy Ω_Λ and spatial curvature density Ω_k.

$$\Omega = \Omega_m + \Omega_R + \Omega_\Lambda + \Omega_k \tag{1.5}$$

Combining the above, one finds that $\Omega > 1$ corresponds to a closed universe, $\Omega < 1$ to an open one, and $\Omega = 1$ resembles a flat universe. With the aid of the necessary expressions, the Hubble parameter can now be expressed in terms of the matter-energy density of the universe and highlights its evolution with time in terms of redshift according to

$$H(z) = H_0\sqrt{\Omega_R(1+z)^4 + \Omega_m(1+z)^3 + \Omega_K(1+z)^2 + \Omega_\Lambda} \tag{1.6}$$

where H_0 represents the present day Hubble constant, and is often expressed as $H_0 = 100h\mathrm{kms}^{-1}\mathrm{Mpc}^{-1}$. As already mentioned, a wealth of information is provided by the CMB, including the energy-matter densities of the universe. The most recent and accurate measurements of the CMB by Planck Collaboration et al. (2016) are shown in Table. 1.1.

TABLE 1.1: Cosmological ΛCDM parameters estimated by Planck

Total matter density	Ω_m	0.3089 ± 0.0062
Baryonic density	Ω_b	0.0486
Dark energy density	Ω_Λ	0.6911 ± 0.0062
Hubble constant	H_0	67.74± 0.46 $kms^{-1}Mpc^{-1}$
$\sigma(M)$ at $8h^{-1}Mpc$	σ_8	0.8159 ± 0.0086
Spectral index	n_s	0.9667 ± 0.0040

Planck Collaboration et al. (2016)

These measurements show that the observed Ω is close to unity, which implies that we live in a flat universe with a critical density corresponding to Eq. 1.3. One can ask what the nature is of the density fluctuations and how these evolve over time to eventually form galaxies, this is discussed in what follows.

From the CMB we have seen that density perturbations were already present in the early universe. An intuitive and often used way to describe these density perturbations is through the density contrast of some local density with respect to the background density of the universe and is expressed as

$$\delta(x,t) = \frac{\Delta\rho}{\rho_u} = \frac{\rho(x,t) - \rho_u(t)}{\rho_u(t)} \tag{1.7}$$

where $\rho(x,t)$ represents the local and $\rho_u(t)$ represents the background density. In the early universe perturbations were small, such that $\delta << 1$. In this regime, perturbations can be regarded as linear. Once they have grown to a sufficient extent (when the density contrast $\rightarrow 1$), these fluctuations evolve towards bound structures as the self gravity overcomes the Hubble expansion. In the linear regime, density perturbations can described analytically using linear perturbations theory as an analogue to the Jeans mass which is the mass that needs to be exceeded in order for collapse to occur (Section. 1.3). In the case of a spherical collapse in a matter dominated Universe, linear theory predicts that fluctuations collapse at an over-density of $\delta_c = 1.686$. Using linear perturbation theory, it can be shown how these fluctuations evolve over time. How fluctuations evolve, depends on the state of the universe. In a radiation dominated universe, they evolve differently from those in a matter dominated universe. Before matter-radiation equality at z_{eq} perturbations evolve according to

$$\delta \propto (1+z)^{-2} \qquad z > z_{eq} \tag{1.8}$$

whereas after matter-radiation equality, the evolve as

$$\delta \propto (1+z)^{-1} \qquad z < z_{eq}. \tag{1.9}$$

Before the epoch of recombination, dark matter density fluctuations evolve differently than baryonic fluctuations. Since DM only interacts through gravity, whereas radiation and matter are coupled until recombination. Before recombination, baryonic perturbations remain to have an amplitude of $\approx 10^{-5}$ and are unable to follow the growing DM perturbations. This is because the pressure from the radiation field to which matter is coupled prevents baryons from collapsing into the DM potential wells. This is illustrated in Figure 1.2 that shows the evolution of the density contrast of DM and baryons. As soon as the universe enters the era of recombination in which the universe becomes neutral and hence transparent to radiation, baryons start couple to the DM density contrast. After recombination, this process occurred fairly quickly leading to a matching density contrast between DM and baryons.

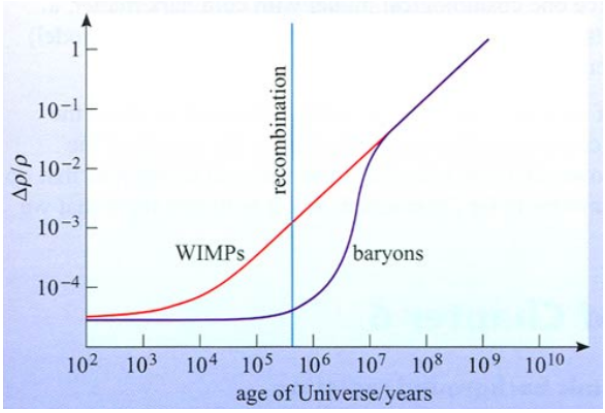

FIGURE 1.2: Density contrast of CDM (red line) and baryons (purple line) as a function of the age of the universe. The vertical blue line indicates the time at which the era of recombination occurs. (Dayal, 2016)

The nonlinear evolution of a dark matter density perturbation will eventually lead to the formation of a dark matter halo, a concentration of dark matter.

1.2 Nature of Dark Matter Halos

Having studied the properties of density fluctuations that evolve into dark matter halos, a key quantity to understand the formation of structure and its evolution over cosmic time, is the number density of dark matter halos for a given mass M at any given redshift z. The latter is referred to as the halo mass function (HMF). First of all, to determine the properties of objects of a given size or mass, one has to determine the variance of mass fluctuations filtered on a particular scale. The mass variance is expressed as

$$\sigma^2(M) = \frac{1}{2\pi^2}\int_0^\infty 4\pi k^2 P(k)\hat{W}^2(k|M)dk \tag{1.10}$$

in which k is the wavenumber that is given by $k = 2\pi/\lambda$ (λ is the size of the perturbation), $P(k)$ is the power spectrum that sets the amount of power regarding fluctuations on a particular scale and $\hat{W}(k|M)$ is the filter or window function that filters the density field on a given scale. A first analytical description of the number density of dark matter halos was provided by Press and Schechter (1974). In their work, they assume that the density perturbations are Gaussian randomly distributed, assume linear gravitational growth and spherical collapse. In this model, they stated that *"the fraction of mass elements with $\delta_M > \delta_c(t)$ is equal to the mass fraction that at time t resides in halos with mass $> M$"*. The distribution for a given δ_M as a

function of mass M is given by

$$p(\delta_M) = \frac{1}{\sqrt{2\pi}\sigma(M)} exp\left[-\frac{\delta_M^2}{2\sigma^2(M)}\right]. \tag{1.11}$$

Then the probability that δ_M is larger than δ_c is given by (Bosch, 2017)

$$P(\delta_M > \delta_c) = \frac{1}{\sqrt{2\pi}\sigma(M)} \int_{\delta_c}^{\infty} exp\left[-\frac{\delta_M^2}{2\sigma^2(M)}\right] d\delta_M = \frac{1}{2} erfc\left[-\frac{\delta_c}{2\sigma(M)}\right] \tag{1.12}$$

in which erfc is the complementary error function [3]. This shows that as a consequence of their statement never more then half of the mass is situated in bound objects. They take into account the possibility that under densities can be located within over-densities by introducing a factor of 2 in Eq. 1.12. From their postulate we find that the fraction of objects with mass $> M$ is thus given by

$$F(> M, t) = erfc\left[-\frac{\delta_c}{2\sigma(M)}\right]. \tag{1.13}$$

One can then define and derive the HMF represented as $n(M,t)$ in the following way (Bosch, 2017). First we have $n(M,t)dM$ which represents the number of halos that have masses in the range $[M, M + dM]$ per co-moving volume. In view of Eq. 1.13, $\frac{\partial F(>M)}{\partial M} dM$ represents the fraction of mass situated in halos with a mass in the range of $[M, M + dM]$. Multiplying the latter by the mean density of the universe $\bar{\rho}$ results in an expression that shows the total mass per unit volume locked up in these halos. Dividing this expression by the mass, results in the HMF

$$n(M,t)dM = \frac{\bar{\rho}}{M} \frac{\partial F(> M)}{\partial M} dM. \tag{1.14}$$

Filling in and evaluating the previous expression results in the following functional form.

$$n(M,t)dM = 2\frac{\bar{\rho}}{M} \frac{\partial P(> \delta_c)}{\partial M} dM = \sqrt{\frac{2}{\pi}} \frac{\bar{\rho}}{M^2} \frac{\delta_c}{\sigma(M)} exp\left(\frac{\delta_M^2}{2\sigma^2(M)}\right) \left|\frac{dln\sigma(M)}{dlnM}\right| dM \tag{1.15}$$

which can be formulated in a more intuitive way as

$$n(M,t) = \frac{1}{2\sqrt{\pi}} \left(1 + \frac{n}{3}\right) \frac{\bar{\rho}}{M^2} \left(\frac{M}{M_*}\right)^{(3+n)/6} exp\left[-\left(\frac{M}{M_*}\right)^{(3+n)/3}\right] \tag{1.16}$$

in which n is the power law index of the power spectrum and M_* denotes the characteristic mass at which the HMF starts to exponentially decrease. This characteristic mass evolves in a matter dominated universe according to

$$M_* = M_*^0 \left(\frac{t}{t_0}\right)^{4/(3+n)} \tag{1.17}$$

in which M_*^0 and t_0 represent the present time and characteristic mass. Eq. 1.16 shows that the shape of the HMF is governed by a power law at low masses and an exponential cutoff at large masses. To obtain a feeling for the nature of the HMF and how it evolves, a range of HMF's are plotted in Fig. 1.3 in the redshift range of $z = 5 - 15$ and are obtained using HMFcalc (Murray, Power, and Robotham, 2013). First of all, it can be seen that low mass halos are the most numerous in the universe as the small scale high sigma fluctuations are the first to collapse. As can be seen, the low mass end is governed by a power law, and at large masses, the number density is exponentially suppressed as these large halos are rare. As time proceeds, the number density of dark mater halos increases and is strongly visible for large halo masses, as these massive halos need time to assemble. This is also why the slope of the HMF is steeper at high redshift, and highlights the fact that low mass halos are most abundant at high redshift. An alternative expression for the HMF that is better in agreement

[3] $erfc(x) = \frac{1}{2}[1 - erf(x)]$

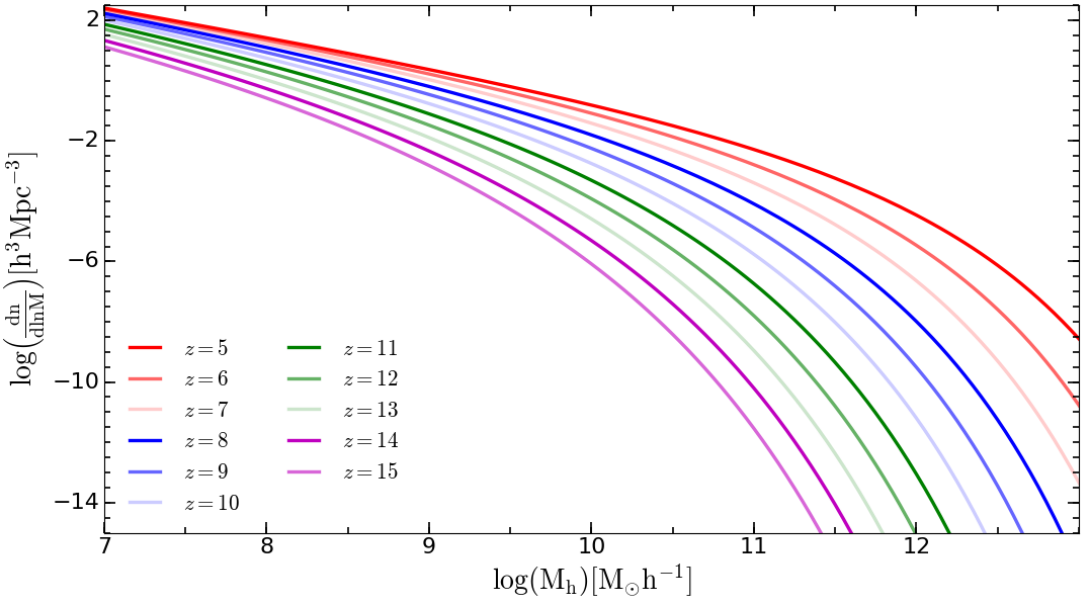

FIGURE 1.3: Press-Schechter halo mass functions (co-moving number density as a function of halo mass) for $z = 5 - 15$, clearly highlighting its evolution with redshift (Murray, Power, and Robotham, 2013).

with N-body simulations is provided by Sheth, Mo, and Tormen (2001) in which they take into account ellipsoidal collapse and is given by

$$n(M,t)dM = \bar{\rho}A\sqrt{\frac{2a}{\pi}}\left[1+\left(\frac{\sigma^2(M)}{a\delta_c^2}\right)^p\right]\frac{\delta_c}{\sigma(M)}exp\left[-\frac{a\delta_c^2}{2\sigma^2(M)}\right]\left|\frac{dln\sigma(M)}{dlnM}\right|dM \tag{1.18}$$

in which $A = 0.3222$, $a = 0.707$ and $p = 0.3$ respectively. Having studied the global properties of dark matter halos as a population, there are some important physical aspects intrinsic to DM halos that will be proven important regarding the formation of galaxies. One of these is the so called virial radius that is defined as the radius in which $\rho \approx 200\rho_{crit}$ times the critical density. This number follows from the virialization of a spherical collapse. A detailed expression of the virial radius is shown below (Barkana and Loeb, 2001).

$$r_{vir} = 0.784\left(\frac{M}{10^8 h^{-1}M_\odot}\right)^{\frac{1}{3}}\left[\frac{\Omega_m}{\Omega_m^z}\frac{\Delta_c}{18\pi^2}\right]^{-\frac{1}{3}}\left(\frac{1+z}{10}\right)^{-1} \quad \mathrm{h^{-1}kpc} \tag{1.19}$$

which is evaluated for the case in which $\rho \approx 178\rho_{crit}$. Another important intrinsic property is the circular velocity v_c of a halo of mass M at a given redshift and is expressed as (Barkana and Loeb, 2001)

$$v_c = \left(\frac{GM}{r_{vir}}\right)^{\frac{1}{2}} = 23.4\left(\frac{M}{10^8 h^{-1}M_\odot}\right)^{\frac{1}{3}}\left[\frac{\Omega_m}{\Omega_m^z}\frac{\Delta_c}{18\pi^2}\right]^{\frac{1}{6}}\left(\frac{1+z}{10}\right)^{\frac{1}{2}} \mathrm{kms^{-1}} \tag{1.20}$$

In particular important as we will see in regards to galaxy formation is the virial temperature of a DM halo and is determined as

$$T_{vir} = \frac{\mu m_p v_c^2}{2k_B} = 1.98\times10^4\left(\frac{\mu}{0.6}\right)\left(\frac{M}{10^8 h^{-1}M_\odot}\right)^{\frac{2}{3}}\left[\frac{\Omega_m}{\Omega_m^z}\frac{\Delta_c}{18\pi^2}\right]^{\frac{1}{3}}\left(\frac{1+z}{10}\right) \quad \mathrm{K} \tag{1.21}$$

in which μ is the mean molecular weight and m_p is the proton mass. In the following we will see how these intrinsic properties of DM halos tie into the theory of galaxy formation.

1.3 Galaxy formation and the role of feedback

It is now known that dark matter halos play a crucial role in the formation of galaxies as these provide gravitational potential wells that accrete gas and in which gas can condensate and cool to form stars. White and Rees (1978) were the first to suggest this scenario in which galaxies form inside dark matter halos. In order for the gas to become denser and eventually to form stars, it needs to cool down. As dark matter halos accrete gas, it gets shock heated as it falls down the potential and approaches virial equilibrium such that the gas approaches the virial temperature of its host halo. A graphical picture of the formation of a galaxy in the latter way is shown in Fig 1.4. The virial temperature of a given halo plays an important role as it sets the dominant mechanism by which the gas cools. Besides the temperature of the gas, the chemical compositions and density also influence the cooling rate. In Figure 1.5 the molecular and atomic cooling rate as a function of the gas temperature is shown. This indicates that $T_{vir} \approx 2 \times 10^4 K$ sets the boundary between the dominant cooling mechanism. Thus in halos with $T_{vir} < 2 \times 10^4 K$ which are the first halos to form, molecular cooling dominates. These halos are the birth place of the first stars that mark the end of dark ages. More massive halos with $T_{vir} > 2 \times 10^4 K$ are dominated by atomic cooling which occurs mainly by recombination radiation, collisional excitation and subsequent decay and Bremsstrahlung (Benson, 2010). Halos with $T_{vir} > 2 \times 10^4 K$ correspond to halo masses with $\geq 10^8 M_\odot [(1+z)/10]^{-3/2}$ (Barkana and Loeb, 2001). As soon as the first stars form in $T_{vir} < 2 \times 10^4 K$ halos, H_2 is photo-dissociated by the UV photons of the newly formed stars and further cooling occurs via atomic cooling.

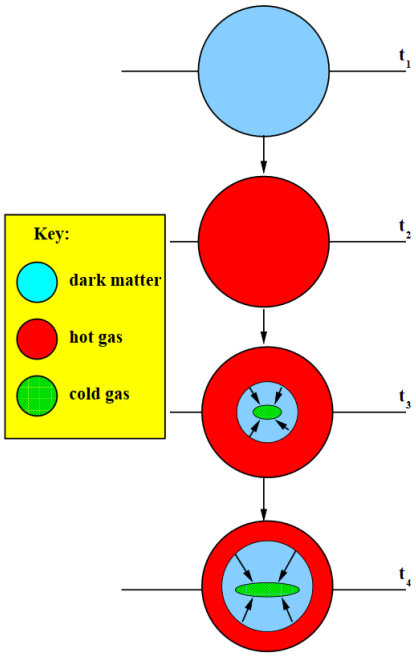

FIGURE 1.4: Graphical illustration of the formation of a galaxy inside a DM halo. Time progresses from top to bottom and colors highlight the different components (Baugh, 2006).

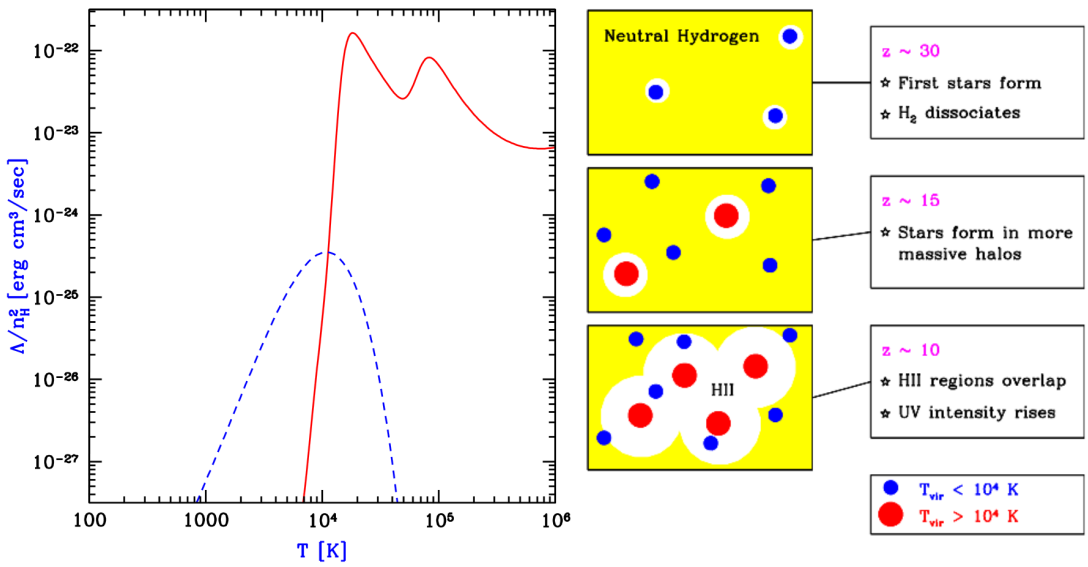

FIGURE 1.5: Left panel: Cooling rate as a function of the temperature for a primordial gas that is composed of hydrogen, helium and molecular hydrogen and no external radiation present. The red line indicates atomic cooling and the dashed line represents the contribution from molecular cooling. Right panel: Schematic illustration of presence of molecular and atomic cooling halos and how these ionize their surrounding neutral hydrogen. (Barkana and Loeb, 2001)

A schematic overview of the evolution in terms of the different cooling halos is shown in Figure. 1.5, which shows that halos $T_{vir} < 2 \times 10^4 K$ harbor the first stars at $z \sim 30$. The first stars in these halos only ionize a small region of the neutral hydrogen (yellow) that surrounds them. At $z \sim 15$, halos with $T_{vir} > 2 \times 10^4 K$ have assembled to form stars. These newly formed stars in these larger halos provide sufficient UV photons to re-ionize the surrounding IGM. These results in overlapping re-ionized regions towards lower redshifts in which the UV background gets stronger and in turn suppresses molecular cooling in $T_{vir} < 2 \times 10^4 K$ halos.

It was found that that the classical picture of White and Rees (1978) regarding the formation of galaxies predicted an excess of the number of faint galaxies as well as bright galaxies. The latter is widely known as the *"over-cooling problem"* which basically points to the fact that in this framework the stars are being produced at an efficiency which is too high w.r.t to observations. This was solved by introducing the notion of *"feedback"* that suppresses the star formation efficiency. A graphical illustration of the over-cooling problem is shown in Figure. 1.6. In order to explain the number of observed faint galaxies, Supernova (SN) feedback (Mac Low and Ferrara, 1999; Springel and Hernquist, 2003; Greif et al., 2007) was introduced in which SN explosions drive gas outflows and thus remove further fuel available for star formation . In addition, SN feedback can also reheat the gas slowing down star formation. The impact of SN feedback on low mass galaxies is further discussed in Chapter 3. An additional source of feedback (UV feedback) is supplied by external UV photons. This effect becomes important once re-ionization has progressed sufficiently, since at this point ionized regions from different galaxies overlap. And in turn, galaxies are exposed to a stronger UV background that can lead to photo-evaporation of large amounts of gas from halos with $< 10^9 M_\odot$ (Susa and Umemura, 2004; Hasegawa and Semelin, 2013). Besides photo-evaporation, the UV background can heat gas in galaxies resulting in a lower star formation efficiency. In addition, UV heating can prevent accretion of gas onto halos with $T_{vir} < 2 \times 10^4 K$. To reduce the number of bright massive galaxies, Active Galactic Nucleus (AGN) feedback (Silk, Di Cintio, and Dvorkin, 2013) has been proposed. AGN can drive powerful outflows that are able to heat the gas inside the halo preventing star formation, and in addition can remove gas from the halo.

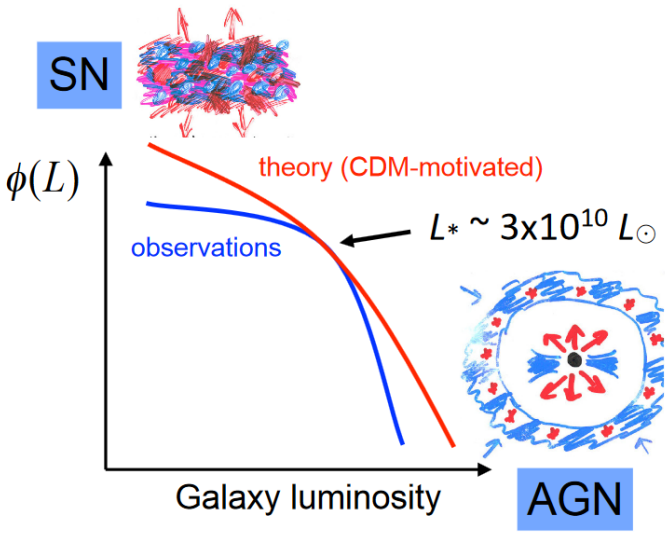

FIGURE 1.6: Schematic illustration of the over-cooling problem, highlighting the excess in the predicted number of faint of bright galaxies. The notion of feedback has been introduced to reduce the number of faint and bright galaxies as highlighted in the figure (Silk and Mamon, 2012).

The cooling timescale for a gas is given by the ratio of the thermal energy density of the gas and its cooling rate. The cooling time for a gas with density ρ_{gas}, temperature T_{vir} and metallicity Z_{gas} is given by (Dayal, 2016)

$$t_{cool} = \left(\frac{3\rho_{gas} k T_{vir}}{2\mu m_H} \right) / \rho_{gas}^2 \Lambda(T_{vir}, Z_{gas}) \tag{1.22}$$

in which $\Lambda(T_{vir}, Z_{gas})$ is the cooling rate. When the the cooling timescale is smaller than the free-fall time scale $t_{cool} < t_{ff}$ ($t_{ff} = (3\pi/32G\rho)^{1/2}$), the gas is able to cool efficiently and fragment and in turn can form stars. Cooling becomes inefficient in the case of $t_{cool} < t_{ff}$ as a critical density is reached at which the gas becomes optically thick to the cooling radiation. Thus when $t_{cool} < t_{ff}$ the gas temperature is unable to decrease, the gas becomes pressure supported (Ciardi and Ferrara, 2005).

However, in order for the gas inside dark matter halos to collapse and form stars, the gas mass needs to exceed the so called Jeans mass, $M_{gas} > M_J$.

$$M_J = \left(\frac{5kT}{Gm_p}\right)^{\frac{3}{2}} \left(\frac{3}{4\pi\rho}\right)^{\frac{1}{2}} \tag{1.23}$$

where ρ is the density of the gas and T the temperature. As the cloud collapses, the density increases, and depending on the cooling efficiency, the temperature drops. As a consequence of the latter, M_J decreases as the cloud collapses and causes the cloud to fragment in a cascade into many small clumps of gas that collapse to form stars. The majority of stellar mass resides in low mass stars as these are present in the largest number, whereas high mass stars are les present. However, the extent to which fragmentation occurs depends on how efficiently gas can cool. And so, more massive stars are thought to form from the metal poor primordial gas as it cools only moderately. A clear picture of the amount of stars that form in a given mass range given by the Initial Mass Function (IMF). The IMF describes the number of stars for a given stellar mass. A widely known and used IMF the the so called Salpeter IMF (Salpeter, 1955a) which is given by

$$\xi(M) = \xi_0 M^{-2.35}. \tag{1.24}$$

which clearly indicates that low mass stars are the most numerous. A more recent IMF is the one given by the Kroupa IMF (Kroupa, 2002) that predicts less low mass stars and consist of three different power laws depending on the mass regime and is represented as

$$\xi(M) = \begin{cases} M^{-0.3} & for \quad M < 0.08M_\odot \\ M^{-1.3} & for \quad 0.08M_\odot < M < 0.5M_\odot \\ M^{-2.3} & for \quad 0.5M_\odot < M \end{cases} \tag{1.25}$$

For any IMF, the total number of stars formed in a certain mass range and the total stellar mass in a given mass range is then given by

$$N = \int_{M_l}^{M_u} \xi(M)dM \qquad and \qquad M_* = \int_{M_l}^{M_u} M\xi(M)dM. \tag{1.26}$$

Most of the stellar mass in galaxies resides in low mass stars, however, after a starburst the luminosity is dominated by massive stars.

1.4 Small Scale Crisis & Alternatives to ΛCDM

The ΛCDM paradigm has been extremely successful in explaining the formation of structure, the large scale matter distribution in the universe, the Lyman-α forest and the temperature anisotropies in the CMB. However, it exhibits a number of discrepancies between predictions of structure on sub-galactic scales in ΛCDM and observations, collectively referred to as the small-scale crisis. While investigating the hierarchical build up of dark matter halo's in a CDM dominated cosmology, Moore et al. (1999b) and Klypin et al. (1999) found that simulations over-predict the number of satellite galaxies with respect to the observed number of the Milky Way. The excess in the numbers of predicted satellite galaxies is referred to as the *missing satellite problem*. Studying the structure of CDM halos, Navarro, Frenk, and White (1996); Moore et al. (1999a) found that predictions of circular velocities in dwarf galaxies overestimate observations. In other words, either cores of the halos are too concentrated or their density profiles are too steep. This inconsistency is known as the *core-cusp problem*. Recently,

Boylan-Kolchin, Bullock, and Kaplinghat (2011) and Boylan-Kolchin, Bullock, and Kaplinghat (2012) found that high resolution ΛCDM simulations predict the MW to have at least 6 massive sub-halos with v_{circ} >30 kms^{-1}. Kinematical observations of MW satellite galaxies have not reported any satellites with v_{circ} >30 kms^{-1} -the *too big to fail problem*-. A detailed summary of the small scale crisis of ΛCDM is given in Weinberg et al. (2015) and Del Popolo and Le Delliou (2017). Various solutions of different nature have been considered in order to resolve the small scale crisis. Aside of solutions that rely baryonic physics, modifications to the nature of dark mater have been proposed. A brief summary of several solutions is given in the following.

At first hand it seems viable to consider baryonic solutions. Since, not observing as many satellite galaxies as ΛCDM predicts does not necessarily imply they do not exist. For this reason baryonic feedback (e.g SN feedback, UV feedback, AGN feedback) is considered in order to suppress star formation within these dwarf galaxies. According to Koposov et al. (2009) a combination of UV feedback in the post reionization era together with a suppression of star formation in halos with $v_{circ} < 10kms^{-1}$ before reionization can solve the missing satellite problem. More recently Del Popolo and Le Delliou (2014) find that all problems can be solved by combining parent satellite interactions through dynamical friction together with UV heating and tidal stripping. In their case dynamical friction flattens inner cusps. As opposed to Garrison-Kimmel et al. (2013) who argue that SN feedback on its own would not be sufficient to solve the core cusp problem, Madau, Shen, and Governato (2014) find that SN feedback can transform cusps in to cores in dwarf spheroidals with $M_* > 10^6 M_\odot$. Studying the coupling between the missing satellite problem and core cusp problem, Peñarrubia et al. (2012) argue that while high star formation efficiency is needed to produce cores, a low star formation efficiency is needed to explain faint dwarfs and the low number of luminous dwarfs that are observed. The recent work of Silk (2017) comes at hand on this issue. According to his work most of the challenges ΛCDM faces are solved if each dwarf galaxy would contain an intermediate mass black hole ($\sim 10^2 - 10^5 M_\odot$) active galactic nucleus (AGN) at its center. Aside of SN feedback, AGN's would provide an additional source of feedback which would further suppress star formation. As SN feedback would be insufficient to starve star formation in massive dwarf galaxies and the fact that outflows can remove dark matter cusps, AGN feedback constitutes a viable explanation for the small-scale crisis.

A different approach is the one in which the nature of dark matter is altered. Since ΛCDM is successful on large scales, this modification to dark matter should only affect sub-galactic scales. A popular candidate is the so called Warm Dark Matter (WDM) that consists of particles that decouple relativistically while in thermal equilibrium and have a mass of $\mathcal{O}$(keV). The idea is that since WDM particles are lighter than CDM ones and decouple relativistically, they have larger free streaming scales that results in a suppression of power below the so called free-streaming scale which largely depends on m_X as shown in paragraph 1.5. Bode, Ostriker, and Turok (2001) find that WDM reduces the number of low mass halos, smoothes cores of massive halos and lowers the characteristic density of low mass halos. On the contrary, Macciò et al. (2012) show that solving the core cusp problem using WDM would require a WDM cosmology suppressing structure to an extent that would prohibit the formation of galaxies at all. Schneider et al. (2014) find that the success in solving the too big too fail problem depends on the WDM particle mass and state that within the WDM particle mass constraints from Lyman α forest and SDSS WDM fails to solve the small scale crisis. Another type of dark matter considered is Fuzzy Cold Dark Matter (FCDM) which consist of ultra light $\mathcal{O}(10^{-22}$eV) boson or scaler particles (Hu, Barkana, and Gruzinov, 2000). In this work, they show that FCDM is able to suppress kpc scale cusps and to reduce the number of low mass halos. In a recent detailed study of the properties and effects of FDM, Hui et al. (2017) find that halos less massive than $10^7(m/10^{-22}eV)^{-3/2}M_\odot$ are unable to form and conclude that if the particle mass lies between 1-10·10^{22}eV FDM would be promising alternative to CDM. However, they stress that there is tension between mass constraints from Lyman-α forest observations that constrain the FDM particle to be 10-20·10^{22}eV or higher. The substructure of fuzzy dark matter halos is studied by Du, Behrens, and Niemeyer (2017) where they explore

the effect from mixtures of CDM and FDM with various mass fractions and also study the effect caused by a variation in FDM particle mass on the small scale suppression. They find that the extent of suppression increases with an increased mass fraction of FDM or decreasing FDM particle mass and may be able to solve the missing satellite problem. Instead of weakly interacting massive particles in the current ΛCDM paradigm, Spergel and Steinhardt (2000) suggest that the small scale crisis can be resolved by introducing self-interacting dark matter (SIDM) particles. Their main findings of SIDM are spherical dark matter halos, the presence of cores in dark matter halos and a lower number of dwarf galaxies.

Many possible explanations for the small scale crisis are offered each with its own distinctive approach, nevertheless there remains debate what the solution is and whether it is baryonic in nature or requires a revision of the nature of dark matter or perhaps a combination of both. Undoubtedly, better observations and research are required to reach a consensus on this matter. In this work, the approach of WDM as an alternative to CDM is considered.

1.5 Warm Dark Matter

A wealth of possible WDM candidates have been proposed of which the most popular ones are WDM in the form of $\mathcal{O}$(10 keV) sterile neutrinos (Dodelson and Widrow, 1994; Adhikari et al., 2017) which are most effectively non-thermally produced through neutrino oscillations as it it hard for sterile neutrinos to thermalize. The other and most widely considered is WDM consisting of $\mathcal{O}$(keV) thermal relic particles that relativistically decoupled while in thermal equilibrium, this form of warm dark matter is assumed throughout this work.

Free-streaming of WDM particles erases power below the free streaming scale which is the typical distance a WDM particle can travel before it is trapped inside a potential well. It is important to note that this free streaming scale strongly depends on the WDM particle mass m_X and increases with decreasing m_X. Implying that the effect WDM has on structure formation strongly depends on m_X. When studying the power spectrum, the supressive nature of WDM becomes evident. The WDM power spectrum can be obtained by applying the WDM transfer function to the power spectrum of CDM as shown below.

$$P_{WDM}(k) = P_{CDM}(k)[T_k^X]^2 \tag{1.27}$$

The transfer function expresses the extent to which power is suppressed on a particular scale with respect to CDM. A widely used transfer function for WDM is obtained in the work of Bode, Ostriker, and Turok (2001) and is given by

$$T_k^X = (1 + (\alpha k)^{2\nu})^{-\frac{5}{\nu}} \tag{1.28}$$

where $\nu = 1.2$ and

$$\alpha = 0.048 \left(\frac{\Omega_X}{0.4}\right)^{0.15} \left(\frac{h}{0.65}\right)^{1.3} \left(\frac{keV}{m_X}\right)^{1.15} \left(\frac{1.5}{g_X}\right)^{0.29}. \tag{1.29}$$

In the latter expression, Ω_X is the cosmological content of the WDM particle X, m_X is the particle mass in keV and g_X is effective number of degrees of freedom of WDM particles. This WDM transfer function takes on values in the range between 0 (maximum suppression) and 1 (no suppression). In view of equations 1.28 and 1.29, the dependence of power suppression on m$_X$ at a certain physical scale becomes evident and is largely set by the αk term in eq. 1.28. As $\alpha \propto m_X^{-1.15}$, either on large scales (small k) or large m$_X$ we have that $1 + (\alpha k)^{2\nu} \approx 1$ and in turn to $T_k^X \approx 1$, this shows that WDM behaves just as CDM on large scales or large m_X. However, as expected, small scales (large k) and small m_X the behavior of WDM diverges from CDM. Another point to make is that for a fixed value of m_X the extent of power suppression is set by the scale k through αk. To appreciate the effect of WDM power suppression due to free-streaming as a function of m_X, halo mass functions for CDM and 0.5, 1.0, 1.5 and 2.0

keV WDM respectively are shown in Fig. 1.7. Comparing these halo mass functions clearly illustrate the strong digression away from CDM with decreasing m_X as the suppression extends to larger scales. A more qualitative picture of the difference between CDM and WDM cosmologies arises from the results of cosmic structure simulations. Figures of simulations for CDM and WDM with particle masses of 2.6, 1.3 and 0.8 keV (Schultz et al., 2014) are shown in figure 1.8 where we find most of the small scale structure being erased for 0.8 keV WDM.

Besides the effect of free-streaming, the velocity dispersion of the WDM particles acts as a pressure which further prohibits the formation structure on small scales. This idea was developed by Barkana, Haiman, and Ostriker (2001) in which they use the pressure analogous of an adiabatic gas to translate this into a pressure of WDM particles and it turn to a Jeans mass below which the pressure can counteract gravity to prevent the formation of a dark matter halo. The effective WDM Jeans mass scale below which the collapse of dark matter is substantially delayed is given by (Pacucci, Mesinger, and Haiman, 2013)

$$M_{\mathrm{J,WDM}} \approx 3.06 \cdot 10^8 \left(\frac{\Omega_X h^2}{0.15}\right)^{\frac{1}{2}} \left(\frac{m_X}{1.0\ \mathrm{keV}}\right)^{-4} \left(\frac{1+z}{3000}\right)^{\frac{3}{2}} \left(\frac{g_X}{1.5}\right)^{-1} M_\odot. \tag{1.30}$$

The $M_{\mathrm{J,WDM}} \propto m_X^{-4}$ scaling renders the dark matter collapse increasingly difficult for low m_X. This additional pressure due to the velocity dispersion of WDM affects the critical density for collapse and makes it mass dependent as opposed to CDM that is mass independent. Benson et al. (2013) find that the results of Barkana, Haiman, and Ostriker (2001) mentioned above are fitted by the following form:

$$\delta_{\mathrm{c,WDM}}(M,z) = \delta_{\mathrm{c,CDM}}(z) \left\{ h(x) \frac{0.04}{\exp(2.3x)} + [1-h(x)] \exp\left[\frac{0.31687}{\exp(0.809x)}\right] \right\} \tag{1.31}$$

where x describes the mass in terms of the Jeans mass for WDM as given below

$$x = \log\left(\frac{M}{M_{\mathrm{J,WDM}}}\right) \tag{1.32}$$

and $h(x)$ is given by

$$h(x) = \left\{1 + \exp\left[\frac{x+2.4}{0.1}\right]\right\}^{-1}. \tag{1.33}$$

This shows that below the Jeans mass, the critical density required for collapse is significantly enhanced with respect to CDM. In Fig. 1.7, WDM halo mass functions are shown that incorporate both the effect of free-streaming and varying δ_c. The latter shows the significant contribution of the variation in δ_c to the suppression of structure on top of the suppression due to free-streaming.

Knowing the suppression of power on a particular scale as a function of m_X is an important tool that allows the possibility of constraining the mass m_X through comparisons of simulations with observations. Extensive research has aimed to constrain m_X over the years. Given the present observational capabilities, one strives to obtain a lower limit on m_X from observations. Several strategies have been invoked in to obtain a lower limit on the particle mass. As a consequence of a delay in structure formation in WDM cosmologies, together with the fact that structure assembles hierarchically (bottom up) in a CDM dominated universe, the high-redshift universe provides an excellent ground to shed light on the nature of WDM. As the Lyman-α forest traces scales that are affected by WDM together with the fact that the amount and quality of quasar spectra have increased in the last years, makes the Lyman-α forest a popular and robust tool to constrain m_X. Using Lyman-α flux power spectra gathered from high resolution spectra of 25 z >4 quasars observed with HIRES and MIKE spectrograph's in combination with high-resolution hydrodynamical simulations, Viel et al. (2013) find a constraint of $m_X \geq 3.3$keV. A limit of $m_X > 4.09$ keV is found using a large sample of medium resolution $2.2 < z < 4.4$ QSO spectra from the ninth data release of SDSS (Baur et al., 2016). After combining their data from the Lyman-α forest with CMB data from Planck 2016, they

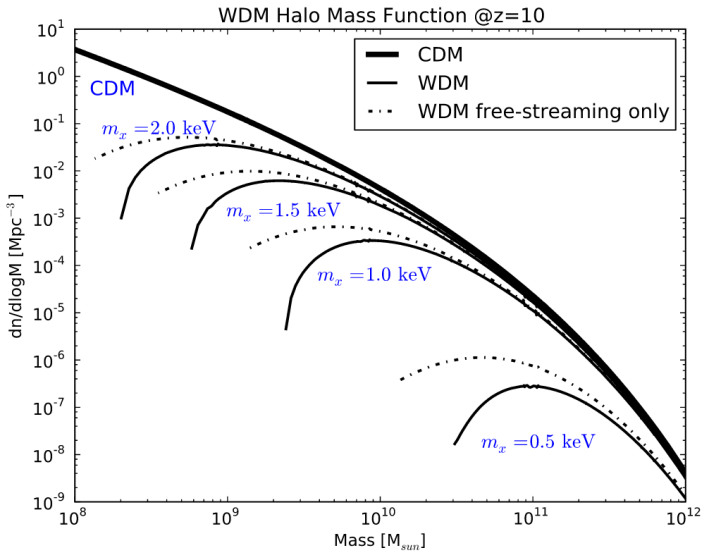

FIGURE 1.7: Sheth Tormen halo mass functions at $z = 10$ for CDM (thick black line) and 0.5, 1.0, 1.5 and 2.0 keV WDM respectively, for free-streaming only (dot-dashed line) and including both free-streaming and the effect of varying δ_c (black line) (Pacucci, Mesinger, and Haiman, 2013).

obtain $m_X > 2.96$ keV. More recently, Iršič et al. (2017) combine high resolution high redshift quasar spectra from Viel et al. (2013) with a sample of medium resolution intermediate redshift QSO spectra from the XQ-100 sample observed with the X-shooter spectrograph and find $m_X > 5.3$ keV using improved modeling of the effect of free streaming of dark matter on the Lyman-α flux power spectrum with hydrodynamic simulations. As previously mentioned, WDM delays the formation of structure and affects the process of re-ionization. This can be used to constrain the nature of WDM trough for example the CMB optical depth. Combining calculations for the Star Formation Rate Density (SFRD), CMB optical depth and ionization fraction $Q_{H_{II}}$ with recent observations including CMB optical depth from Planck, Tan, Wang, and Cheng (2016) constrain the mass to be 1 keV $< m_X <$ 3 keV. Lopez-Honorez et al. (2017) combine simulations of the global fraction of ionized gas and the thermal history of the IGM with observations of these two quantities complemented with the CMB optical depth from Planck and note $m_X > 1.3$ keV. Gravitational lensing has been proven to be a powerful tool to study the number of low mass galaxies at high redshift that are too faint to be directly observed, in addition it is used to obtain information about the DM substructure using anomalous flux ratios. Therefore gravitational lensing provides a sensitive probe to the nature of WDM. Using two $z \approx 10$ lensed galaxies observed with HST in combination with analytical WDM mass functions at $z = 10$, Pacucci, Mesinger, and Haiman (2013) have obtained a bound of $m_X > 0.9$ keV. Combining high-resolution N-body simulations in WDM with four observed quadruple lenses that show anomalous flux ratios, Inoue et al. (2015) find a limit of $m_X > 1.3$ keV. Menci et al. (2016a) compare observed UV luminosity functions of ultra faint galaxies at $z \approx 6$ in the Hubble Frontier Fields with the maximum number density of dark matter halos in WDM cosmologies resulting in $m_X \geq 2.1$ keV. In addition, the same authors constrain the WDM particle mass by comparing computed mass functions in various WDM cosmologies to Ultra Deep UV luminosity functions at $z \approx 2$ and find $m_X \geq 1.8$ keV (Menci et al., 2016b). More recently Birrer, Amara, and Refregier (2017) use a merger tree in combination with detailed lens modeling to quantify the observed substructure in the RXJ1131-1231 lens and rule out $m_X < 2$ keV. A different approach is used by de Souza et al. (2013) where they find that $m_X \geq 1.6$-1.8 keV by using high-redshift long gamma-ray bursts. Besides the high redshift universe, the local universe presents additional ways to constrain the nature of WDM e.g through the abundance of MW satellites. Using a semi-analytic model of galaxy formation, Kennedy et al. (2014) predict satellite luminosity functions and compare them to the observed data for the MW dwarf spheroidals and obtain a limit of $m_X > 3.3$ keV for a MW halo mass $> 1.4 \cdot 10^{12} M_\odot$. More recently, Jethwa, Belokurov, and Erkal (2016) investigated the connection between galaxies and dark matter halos at the lowest mass scales

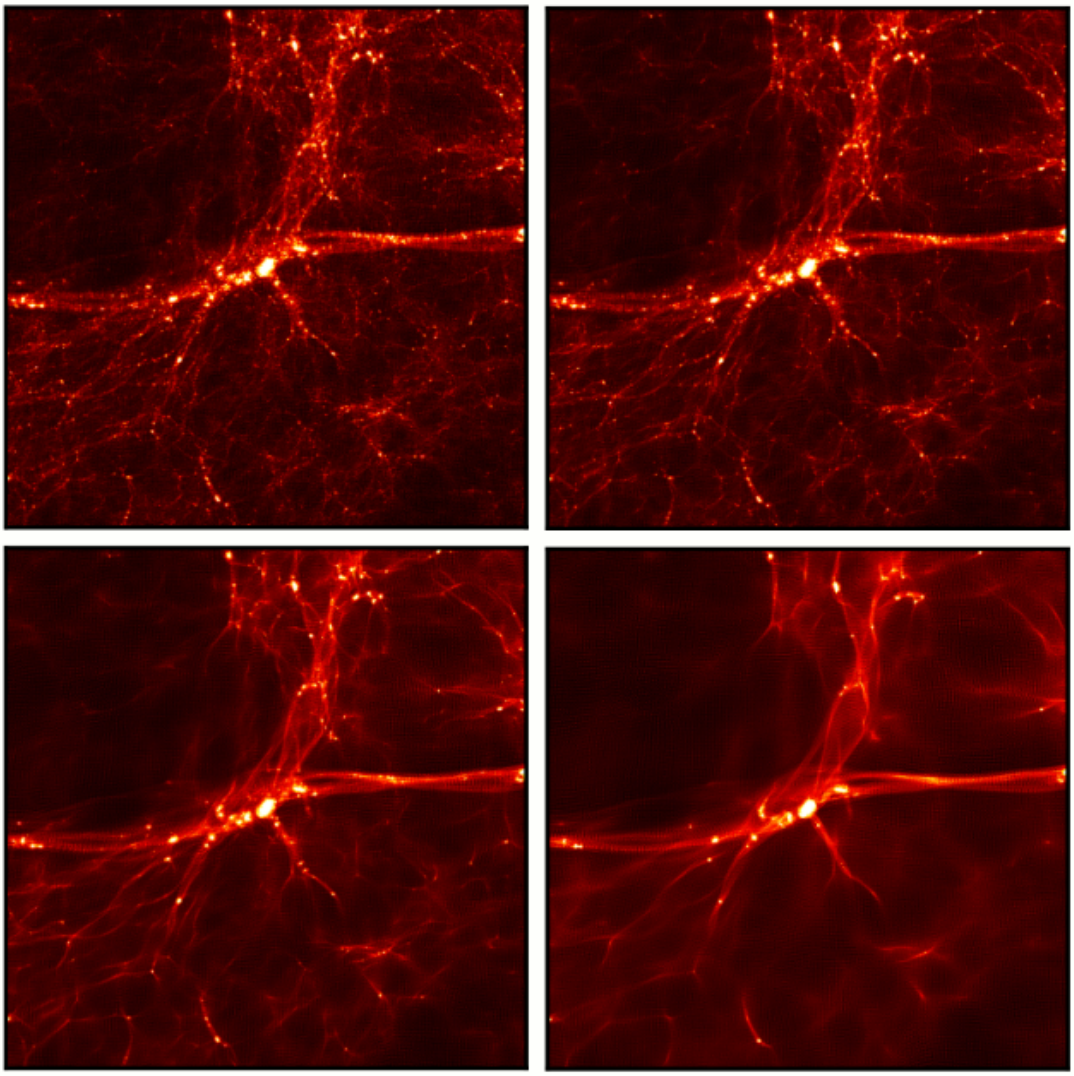

FIGURE 1.8: Simulations for CDM and WDM at $z = 6$ with the same initial conditions for each cosmology. The dimensions of these panels are $10\text{h}^{-1}Mpc$ square and $6\text{h}^{-1}Mpc$ deep. Upper left panel represents CDM while the upper right panel gives the result of WDM 2.6 keV. Bottom panels show 1.3 keV (left) and 0.8 keV (right). These results are form the work of Schultz et al. (2014).

through modeling the luminosity function of MW satellite galaxies and find that $m_X > 2.9$ keV.

1.6 Metals in the Intergalactic Medium & our Motivation

In order to study the presence of metals and its evolution in the IGM, one needs a way to probe the IGM at high redshift. The main method to study the IGM is through the absorption features along the line of sight between a bright sources at high redshift and us. A powerful tool to study the IGM, is through observing high redshift quasars (QSO's). These are highly luminous AGN's that produce energetic radiation and are visible at large distances. The method to probe the IGM using quasars in shown in Fig. 1.9. This shows the absorption features in the QSO spectrum due to the intervening neutral hydrogen clouds that are situated at different redshifts along the line of sight. As the universe becomes more neutral towards high redshifts, more and more intervening clouds are present that in turn result in a forest of absorption features -the *"Lyman-α forest"*. This then allows to study the evolution of the presence of metals in the IGM. The most commonly observed metal line in quasar absorption spectra is that of Carbon in its triply ionized state C_{IV} and consists of the $\lambda = (1548, 1551)$ Å

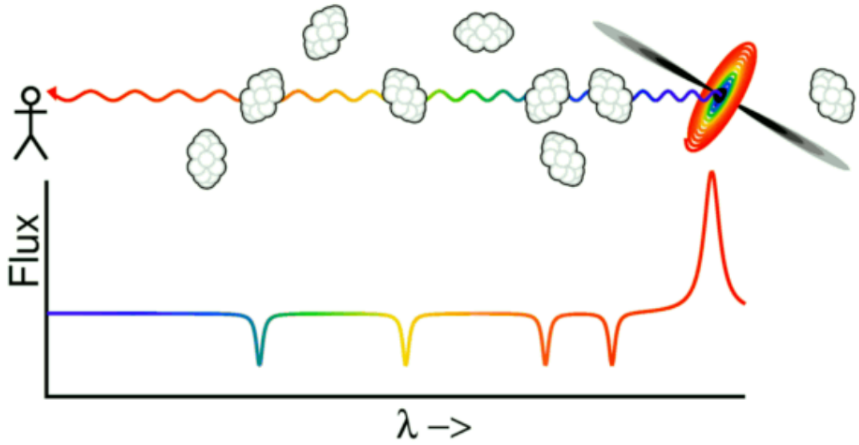

FIGURE 1.9: Representation of the method to probe the IGM along the line of sight of a distant Quasar. The absorption features shown in the spectrum are a consequence of the intervening neutral hydrogen clouds, and are collectively referred to as the Lyman-α forest. `http://www.astro.ucla.edu/~wright/Lyman-alpha-forest.html`

doublet (Ryan-Weber et al., 2009). A lot of work has been devoted to study the cosmic history of the C_{IV} content of the IGM in terms of $\Omega_{C_{IV}}$ as shown in Fig. 4.10.

In this work, the impact of WDM cosmologies on the metal enrichment of the IGM is investigated to find whether these differences can be used as a tracer to disentangle the nature of DM. The metal enrichment is quantified in terms of C_{IV} that is accessible to observations. The idea to study the impact of WDM on the metal enrichment of the IGM is motivated by the fact that the number of low mass halos is suppressed in light particle WDM cosmologies. As low mass galaxies are believed to be efficient metal polluters of the IGM (in view of their shallow potential wells) Mac Low and Ferrara (1999), Greif et al. (2007), and Oppenheimer, Davé, and Finlator (2009), one naturally expects the IGM to harbor less metals in WDM cosmologies as a consequence of the dearth in low mass halos which increases with lower WDM particle mass m_X. This motivation is illustrated by considering the DM halo mass density in 1.5, 3 and 5 keV WDM with respect to CDM. This highlights the effect WDM has on the presence of low mass halos. The DM halo mass density ratio is divided in the following two mass regimes with $M_h < 10^{9.5} M_\odot$ and $M_h > 10^{9.5} M_\odot$. These DM halo mass densities in WDM with respect to CDM are shown in Figure. 1.10. Regarding the DM halo mass densities with $M_h > 10^{9.5} M_\odot$, we find that in 5 keV WDM, roughly 50 $\%$ of the mass with respect to CDM has been assembled at $z \approx 12$ increasing to 100 $\%$ at $z \approx 5$. In 1.5 keV WDM on the other hand, the assembled halo mass with respect to CDM reduces to $\approx 18\%$ at $z \approx 12$ and becomes roughly 75% at $z \approx 5$. As expected, the impact of 3 keV WDM lies in between that of 5 and 1.5 keV.

The impact of WDM is most clear in the case of the DM halo mass density of halos with $M_h < 10^{9.5} M_\odot$. In 1.5 keV WDM only 1% of the halo mass with respect to CDM has been assembled at $z \approx 10$ increasing to 6% at $z \approx 5$. Comparing to 5 keV WDM, this difference reduces to $\approx 40\%$ at $z \approx 10$ and roughly 70% at $z \approx 5$. This result highlights the large dearth of low mass halos in 1.5 keV WDM.

The first part of this work consists of an analytic approach to get a rough estimate of the impact of different WDM cosmologies on the metal mass density in the IGM and in addition to gain familiarity with the physics involved in galaxy formation. Most of this work is devoted to study the impact of 1.5 keV WDM on the UV LF, SMD, ejected gas mass density and in turn the metal enrichment of the IGM using a semi-anlaytic model in which the assembly of each galaxy is tracked. This is then compared to observations. Throughout this work, the following cosmological parameters are adopted $(\Omega_\mathrm{m}, \Omega_\Lambda, \Omega_\mathrm{b}, h, n_s, \sigma_8) = (0.3089, 0.6911, 0.0486, 0.6774, 0.9667, 0.8159)$ that are measured by the Planck satellite (Planck

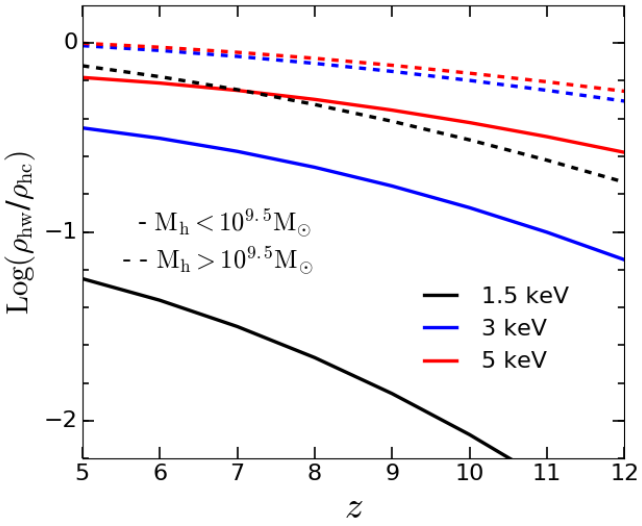

FIGURE 1.10: Log of the total DM mass density bound in WDM halos (ρ_{hw}) relative to CDM (ρ_{hc}) for 1.5 kev (black), 3 keV (blue) and 5 keV (red) WDM. Solid lines indicate the DM mass density bound in halos with $M_h < 10^{9.5} M_\odot$ and dotted lines indicate that of $M_h > 10^{9.5} M_\odot$.

Collaboration et al., 2016) unless stated otherwise.

Chapter 2

Observing high-z galaxies

In order to study the formation and evolution of galaxies and the corresponding cosmic star formation history over the first billions of years of the universe, one needs to detect high-z galaxies. There are two major techniques to detect high z galaxies, one of them is based on broad band filters to detect Lyman Break Galaxies (LBGs), and the other relies on narrow band filters and detects Lyman-α Emitters (LAEs). Both techniques are explained below followed by a discussion of the key observables shaping the early universe.

2.1 Detection techniques

A popular method of finding galaxies at $z > 5$ is the so called Lyman-break technique. This method is based on the fact that light blue ward of $\lambda_{rest} = 1216$Å is absorbed by the ISM and intervening neutral IGM at high redshift either by ionizing hydrogen or via Lyman-α absorption. This causes a characteristic break at a rest frame wavelength of 912Å at low-z and shifts to 1216Å Lyman-α at high-z below which the flux is diminished by 2-3 orders of magnitude. These galaxies are referred to as LBGs (Steidel et al., 1999; Dunlop, 2013).

This property of LBGs in combination with broad band filters (cover a wide range of wavelengths) is used to find high-z LBGs. As one observes a particular region on the sky with different broad band filters, galaxies can suddenly disappear in a filter short-ward of a particular wavelength depending on the redshift of the galaxy. This then indicates the wavelength range of the Lyman break and is also referred to as the dropout technique. At redshift $z \approx 7$ for example, the Lyman break is red-shifted to $\lambda_{obs} \approx 1\mu$m which causes the galaxy to disappear in filters that cover shorter wavelengths. To clarify this method, an illustration is shown in Figure 2.2 of two LBGs spectral energy distributions (SEDs) in different filters spanning a wavelength range of $\approx 0.3 - 1.7\mu$m. At observed wavelengths short ward of the Lyman-break, no galaxy is visible in the filter as most emission is absorbed. However, in the filter that matches the red-shifted wavelength of the Lyman break, flux of a galaxy starts to appear. This provides a photometric redshift that is as uncertain as the width of the filter. The advantage of this method is that large volumes can be sampled, the redshift information on the other hand is not accurate.

It is believed that young star forming galaxies with star formation rates of $1-10\,\mathrm{M_\odot yr^{-1}}$ make up LAEs (IYE, 2011). The strong UV radiation produced by young hot massive stars ionizes the interstellar neutral hydrogen. This ionized hydrogen in turn recombines and eventually cools via the emission Ly-α photons which results in a strong Ly-α emission from these galaxies. High redshift $z > 5$ LAE have a characteristic asymmetric emission profile because of absorption by the IGM blue wards of $\lambda_{rest} = 1216$ Å. Compared to LBGs, LAEs have a much weaker stellar continuum. An example spectrum of a $z = 5.7$ LAE is shown in Fig. 2.1 clearly highlighting its characteristic features and its different nature with respect to LBGs (Dunlop, 2013). Regardless of the strong Lyman-α, LAEs are difficult to detect because of the fact that

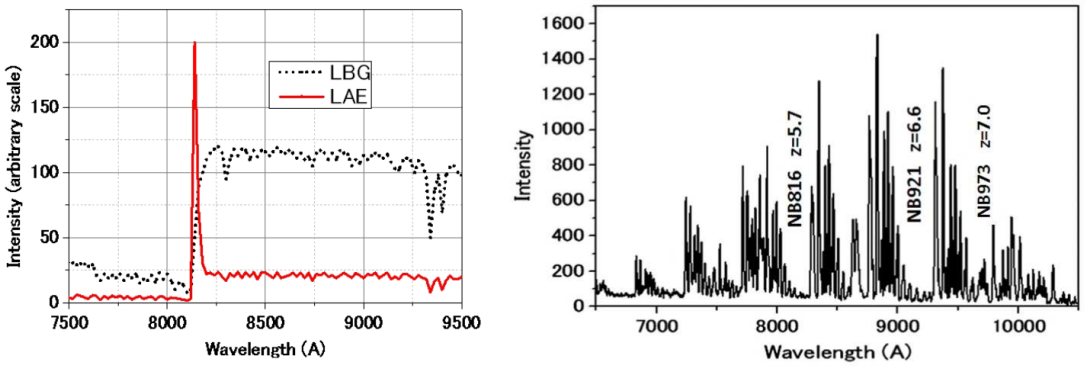

FIGURE 2.1: Left: Typical spectrum of a $z = 5.7$ LAE (red solid line) and a LBG (black dotted line) clearly indicating the characteristics of these two classes of galaxies. The wavelength indicates the observed wavelength. Right: Night sky OH emission lines, with several windows in between, which are used to detect LAE with narrow band filters specifically designed to match these windows as highlighted in the figure (Dunlop, 2013).

Ly-α is easily scattered or absorbed by dust and HI in the ISM and HI in the IGM.

Because of their characteristic nature, LAEs are detected using narrow band filters that are carefully designed to avoid night sky emission lines. Several narrow band filters for the SUBARU telescope that lie in between the sky emission lines are shown in Fig. 2.1. This technique provides accurate redshift information, but it can only sample small volumes.

What one can learn from these detected high-z galaxies will be discussed in the following.

2.2 UV Luminosity Function

Schechter (1976) proposed an analytical expression for the number density of galaxies as a function of their luminosity, the Luminosity Function. In terms of absolute magnitudes, the luminosity function is given as

$$\phi(M) = 0.4ln(10)\phi^* \left(10^{0.4(M^*-M)}\right)^{(\alpha+1)} \exp\left[-10^{0.4(M^*-M)}\right] \tag{2.1}$$

in which $\phi(M)dM$ represents the number-density of galaxies in the absolute magnitude range dM, ϕ^* is the normalization number density, M^* is the characteristic magnitude and α sets the slope of the faint end (low mass galaxies) of the LF. For high-z, it is generally defined as the number density of galaxies per rest frame UV magnitude M_{UV} at $\lambda_{rest} \approx 1500$ Å or $\lambda_{rest} \approx 1600$ Å, known as the UV LF. As the emission of young stars is dominated by the ultraviolet emission, UV emission a good tracer of recent star formation (Madau and Dickinson, 2014). Therefore, the UV LF provides insight in the formation and evolution of galaxies in the early universe.

Having discovered high-z galaxies, their rest frame UV magnitude $\mathrm{M_{UV}}$ can then be determined as explained in Chapter 3.1. The number density is then evaluated from the volume that has been sampled to select these galaxies. Several observed UV LFs are shown in Fig. 2.3 for redshifts of $4 - 10$. These observations clearly highlight the evolution in the number density of galaxies with redshift and show the underlying Schechter distribution. In addition, the slope α of the faint end is seen to steepen as in the case of the Schechter HMF and ranges from -2.27 at $z \approx 10$ to -1.64 at $z \approx 4$ (Bouwens et al., 2015). The normalization number density ϕ_* ranges from $\approx\ 0.008 \times 10^{-3}\mathrm{Mpc}^{-3}$ at $z \approx 10$ to $\approx\ 1.97 \times 10^{-3}\mathrm{Mpc}^{-3}$ at $z \approx 4$. $\mathrm{M^*_{UV}}$ remains close to -21 in the redshift range $z \approx 4 - 10$ (Bouwens et al., 2015). As observations provide better constraint on the UV LF, it provides a key feature to test galaxy formation models.

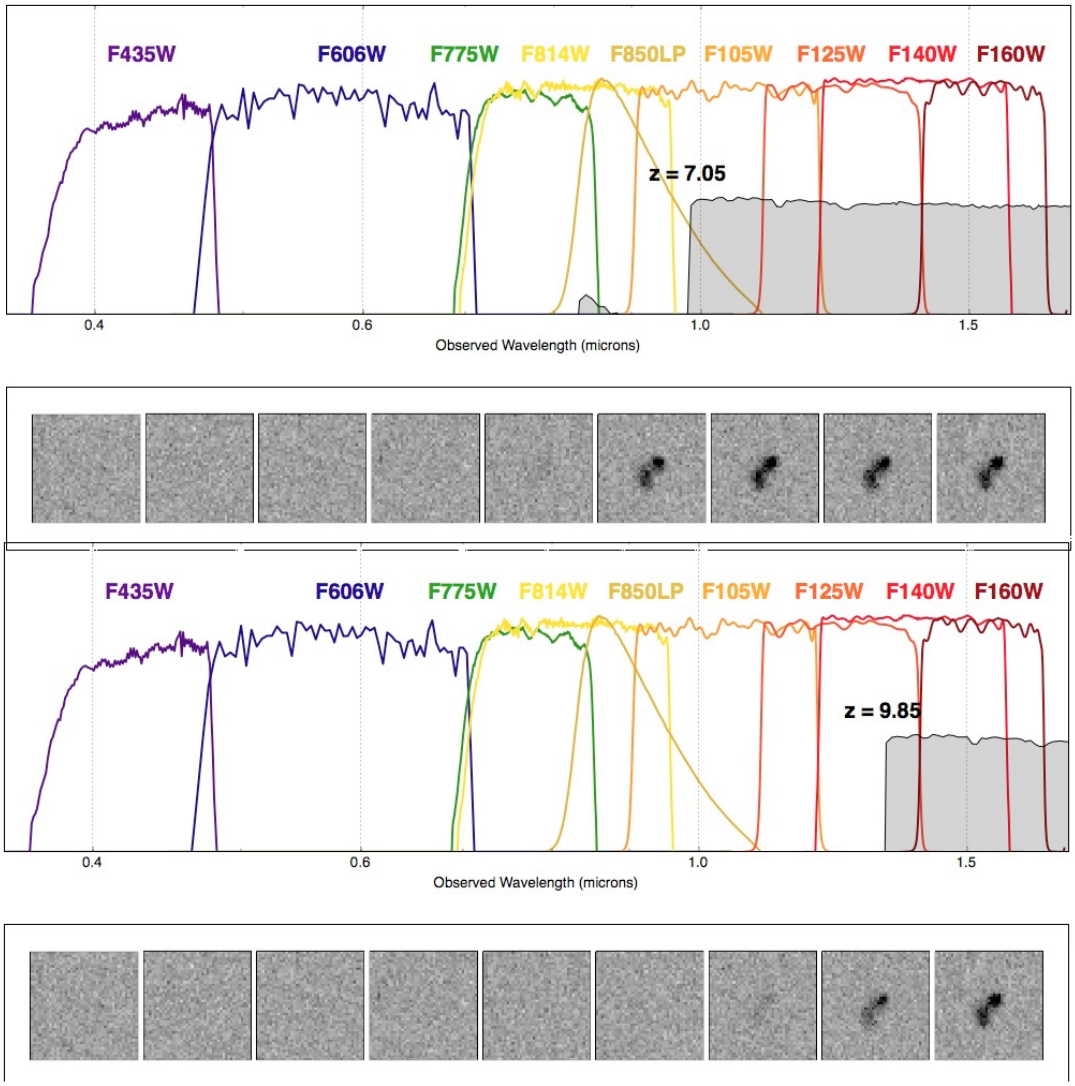

FIGURE 2.2: This figure highlights the dropout technique used to find LBGs. The figure on top of each panel represents the SED of the galaxy together with a set of broad band filters that are over-plotted. The figure on the bottom of both panels shows the visibility of the galaxy in each different filter covering a different wavelength range. The top panel shows a LBG at $z \approx 7$ and the bottom one at $z \approx 10$, respectively (XDF, 2017). `http://xdf.ucolick.org/xdf.html`

2.3 Star formation rate density

A key quantity in terms of the evolution of the universe is the rate of which stellar mass is assembled. This is quantified as the Star Formation Rate Density (SFRD) and has units of $\mathrm{M_{\odot} yr^{-1} cMpc^{-3}}$. Since UV emission is a good tracer of recent star formation, it has been shown that the UV luminosity can be directly related to the SFR (Madau and Dickinson, 2014), using the factor shown in Eq 3.16. From the evolution of the comoving UV luminosity density that is obtained by integrating the evolving UV LF, one thus obtains the SFRD as traced by UV emission. One has to bear in mind that UV is not representing the total of star formation rate since UV photons are absorbed by dust and re-emitted in the IR. Better estimates of the evolution of the SFRD thus require IR measurements of high-z galaxies that can be converted into a SFRD that is traced by IR. The total star formation rate density is then given by sum of the contributions from UV and IR. Another technique that is generally applied to correct for the effects of dust in high-z galaxies is by measuring the slope of the UV continuum which gives an indication for the effects of dust (Dunlop, 2013). However, the presence of less dust at the highest redshift requires less dust correction (Bouwens et al., 2014a). In Fig. 2.4 the

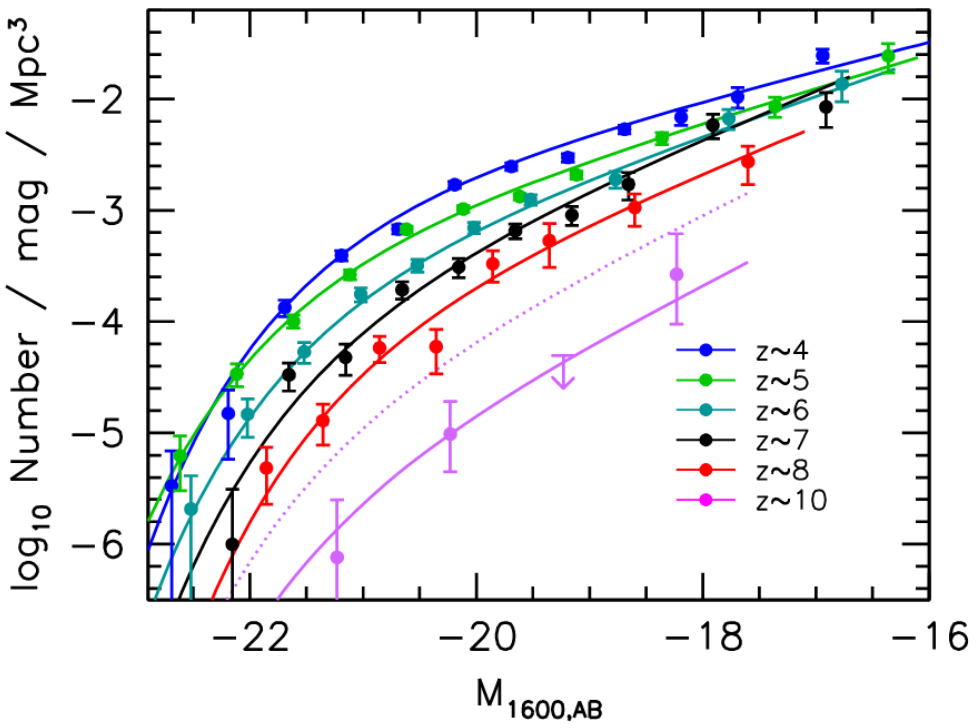

FIGURE 2.3: Observed UV LFs (points) at $\lambda_{rest} \approx 1600$ Å in the redshift range of $z = 4 - 10$ as highlighted by the different colors. The solid line indicate Schechter fits the data with the following parameters: the slope α of the faint end ranges from -2.27 at $z \approx 10$ to -1.64 at $z \approx 4$. The normalization number density ϕ_* ranges from $\approx \ 0.008 \times 10^{-3}\mathrm{Mpc}^{-3}$ at $z \approx 10$ to $\approx \ 1.97 \times 10^{-3}\mathrm{Mpc}^{-3}$ at $z \approx 4$. $\mathrm{M^*_{UV}}$ remains close to -21 in the redshift range $z \approx 4 - 10$ (Bouwens et al., 2015).

evolution of the UV and IR SFRD and of the combined SFRD is shown. This shows that the rate at which stellar mass assembles in the universe increases up to the peak at $z \approx 2$ and then decreases. To date, the SFRD has been measured extensively at $z > 8$ up to $z \approx 11$ as shown in Fig. 10 of Bouwens et al. (2014a).

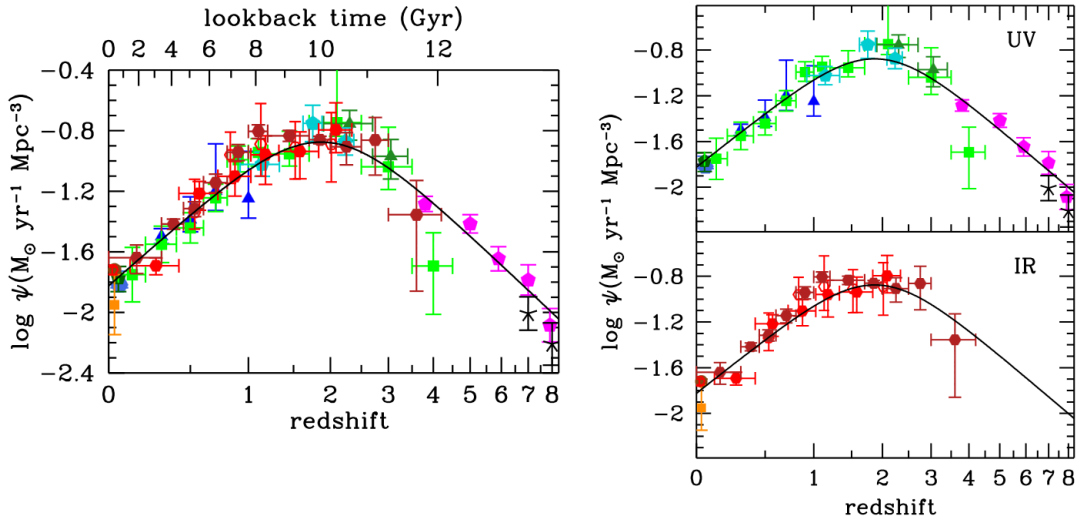

FIGURE 2.4: Star formation rate density from UV+IR rest frame observations (left panel), UV (top right panel) and IR (lower right panel). The solid curve shows the best fit to the data (Madau and Dickinson, 2014).

2.4 Stellar Mass Density

The Stellar Mass Density (SMD) or stellar mass per comoving volume sheds light on how much star formation has taken place in the universe up to the point at which it has been observed. And so it resembles a powerful tool to understand early galaxy formation and provides a solid test for galaxy formation models. To determine the SMD, one first needs to determine the stellar mass of high-z galaxies. Since the stellar mass of a galaxy is dominated by cool low mass stars that mainly emit light in the optical to NIR regime, observations in the latter two wavelength regimes are thus essential to determine stellar masses (Madau and Dickinson, 2014). Even though the optical and NIR trace the majority of the stellar mass, in general the stellar mass of a galaxy is determined from the observed spectral energy distribution (SED) of a galaxy. This is achieved by the use of stellar population synthesis models that simulate SEDs for galaxies. The SMD is then obtained by integrating the galaxy stellar mass function (number density of galaxies as a function of their stellar mass). Observationally determined SMDs are shown in Fig 2.5 clearly highlighting the build up of stellar mass over cosmic time. and shows that only a small fraction of stellar mass in the universe was assembled over the first billion years of the universe.

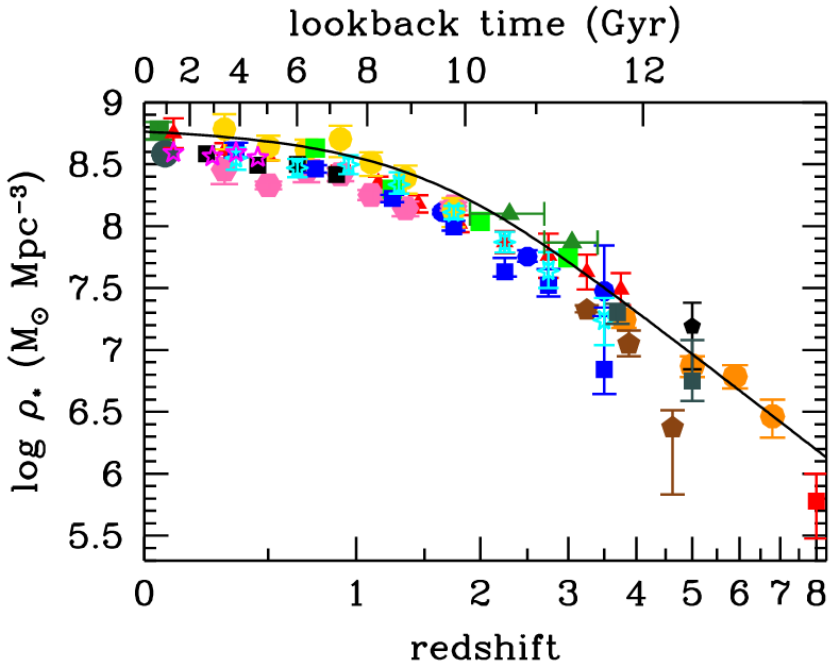

FIGURE 2.5: Evolution of the observed stellar mass density with redshift (Madau and Dickinson, 2014).

Chapter 3

Analytical Approach

To gain an understanding and intuition in the key physics involved in galaxy formation, and how these connect to observables such as the UV LF or SMD , an analytical model is considered in this chapter before the more complicated nature and physics of the merger tree is discussed in Chapter 4. In addition, this provides first insights in the effect of different warm dark matter cosmologies on the former quantities and on the metal mass ejected into the IGM. The simplicity of this approach lies in the fact that each galaxy population is assembled and studied independently at each redshift without taking any galaxy evolution into account. In this approach, we assign a gas mass to each dark matter halo that in turn is converted into stars. Feedback is only applied in the form of internal SNII feedback whereas external feedback such as UV feedback is ignored here. The internal feedback prescription is based on the balance between the SNII energy available to drive outflows and the binding energy of a given dark matter halo. The above is then applied for each redshift to all dark matter halos in the mass range of the Shet-Tormen halo mass functions from which the UV LF, SMD, SFRD, ejected gas mass density and in turn ejected metal mass density are inferred. This analytical model is applied to CDM and 1.5, 3 and 5 keV WDM respectively.

3.1 Model

In this approach of galaxy formation, we only consider internal SNII feedback, where we compare the energy input of SNII explosions that cause gas outflows to the gravitational potential of the host halo. Either the SNII energy available to drive outflows exceeds the binding energy and all gas is ejected, or the binding energy is larger and only part of the gas mass is ejected. The formalism and concept of this approach is based on the work of Dayal et al. (2014). First of all, the assembly of stellar mass is treated using the formalism for the star formation efficiency as described in detail in the following.

The total amount of SNII energy available from an assembled stellar $M_*(z)$ mass at redshift z that acts as the driver of outflows is given by

$$E_{SN} = f_w E_{51} \nu M_*(z) = f_w v_s^2 M_*(z) \tag{3.1}$$

where f_w is the fraction of SNII every that is turned into kinetic energy to drive outflows, where the assumption is made that each SNII explosion transfers an energy of $E_{51} = 10^{51}$erg to the ISM and the amount of SNII explosions per stellar mass is given by $\nu = [134 M_\odot]^{-1}$ for a Salpeter IMF (Salpeter, 1955b) in the range of 0.1-100 $M_\odot$. Then from Eq.3.1 a value of $v_s = 611$ kms^{-1} is obtained for the SNII ejecta velocity. The binding energy of the remaining gas that is left after a star formation episode or equivalently, the energy needed to eject this remaining gas for any given halo is given by

$$E_{ej} = \frac{1}{2}[M_{g,i}(z) - M_*(z)] v_e^2 \tag{3.2}$$

in which $M_{g,i}$ is the initial gas mass present and $M_{g,i}(z) - M_*(z)$ represents the ISM mass present after the formation of stars has taken place. v_e is the escape velocity that is related to the circular velocity of a given dark matter halo through $v_e = \sqrt{2}v_c$. In this model, the expression of eq. 1.20 is used for the circular velocity. Combining all the above, the star formation efficiency required to eject the remaining gas that has not been turned into stars can be calculated. The latter is also defined as the ejection efficiency f_*^{ej} and can be written as

$$f_*^{ej}(M_h, z) = \frac{v_c(M_h, z)^2}{v_c(M_h, z)^2 + f_w v_s^2}. \tag{3.3}$$

Because of the redshift dependence of the circular velocity, f_*^{ej} changes with redshift for a particular halo mass. To obtain a better view of this dependence, f_*^{ej} as a function of M_h is shown in Fig. 3.1 for various redshifts. This shows that at high redshift a higher star formation efficiency is required to eject the remaining gas mass for a given halo mass as compared to lower redshifts. This is a consequence of the redshift scaling of the virial radius $r_{vir} \propto (1+z)^{-1}$ (translating to $v_c \propto (1+z)^{\frac{1}{2}}$) that causes the potentials of dark matter halos to be deeper with increasing redshift. The latter is illustrated in Fig. 3.1 by over-plotting a line corresponding to a single value of f_*^{ej}, which clearly indicates the shift towards larger M_h with decreasing redshift.

Having an expression for f_*^{ej}, we use the expression for the effective star formation efficiency f_*^{eff} (Dayal et al., 2014) as given by

$$f_*^{eff} = min\left[f_*, f_*^{ej}(M_h, z)\right]. \tag{3.4}$$

Thus, the latter implies that low mass galaxies form stars at their maximum efficiency, meaning that $f_*^{eff} \rightarrow f_*^{ej}$ wheres massive galaxies can form stars with a higher efficiency of $f_*^{eff} \rightarrow f_*$ (since $f_*^{ej} > f_*$) and in turn ejecting only small fractions of their gas.

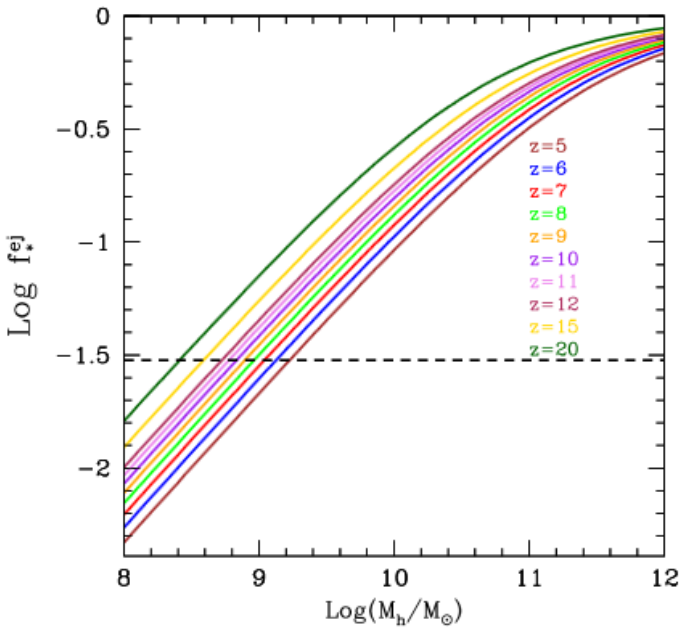

FIGURE 3.1: The ejection efficiency f_*^{ej} required to unbind the remaining ISM after the assembly of stellar mass as a function of halo mass M_h is shown for redshifts $z = 5 - 20$ as indicated by the different colors. The deepening of the potentials is clearly visible through the upwards shift in f_*^{ej} with increasing redshift. The constant horizontal line corresponds to $f_*^{ej} \approx 3\%$ (Dayal et al., 2014).

Next, we populate populate each dark matter halo with an initial gas mass that is obtained

assuming a cosmological baryon to matter fraction for each halo as shown below.

$$M_{g,i}(z) = \frac{\Omega_b}{\Omega_m} M_h(z) \tag{3.5}$$

For each halo, part of this gas mass is then assembled into a stellar mass according to f_*^{eff} as

$$M_*(z) = f_*^{eff}(z) M_{g,i}. \tag{3.6}$$

Having assigned a stellar mass to each dark matter halo, it is now possible to quantify the ejected gas mass due to the formation of this stellar mass. As already mentioned, this is evaluated through a comparison of the SN II energy available to produce outflows with the energy required for complete removal of the remaining gas. The expression for the ejected gas mass, which distinguishes between the regimes of complete and partial removal of gas is given below.

$$M_{g,ej}(z) = \begin{cases} M_{g,i}(z) - M_*(z) & \frac{E_{SN}}{E_{ej}} \geq 1 \\ [M_{g,i}(z) - M_*(z)] \frac{E_{SN}}{E_{ej}} & \frac{E_{SN}}{E_{ej}} < 1 \end{cases} \tag{3.7}$$

The latter simply translates into the gas mass that remains bound for a given halo

$$M_{g,bound}(z) = \begin{cases} 0 & \frac{E_{SN}}{E_{ej}} \geq 1 \\ [M_{g,i}(z) - M_*(z)] \left(1 - \frac{E_{SN}}{E_{ej}}\right) & \frac{E_{SN}}{E_{ej}} < 1 \end{cases}. \tag{3.8}$$

An illustration of this is shown in Fig. 3.2, where the stellar and ejected gas mass as a function of halo mass are shown at $z = 5 - 12$ for the parameters $f_* = 0.04$ and $f_w = 0.1$. This figure beautifully shows that for low halo masses the stellar mass changes notably with redshift whereas the ejected gas mass barely shows any difference. The change in slope indicates the transition from $f_*^{eff} = f_*^{ej}$ to $f_*^{eff} = f_*$ and shifts to larger halo masses with decreasing redshift. For large halos on the other hand, the stellar mass is independent of redshift. The opposite trend occurs in the case of the ejected gas mass, where for low mass halos there is a minor change with redshift since all gas is ejected. In the case of large halos, there is a significant difference with redshift as $f_*^{eff} = f_*$.

To evaluate the ejected metal mass, the metallicity of the gas with the newly formed stellar population for each halo is calculated first. In this approach, the gas is assumed to be perfectly mixed with metals. The metallicity X of the ISM is then computed by simply diving the metal mass produced by the newly formed stars by the total gas mass left after the stars have formed as given by

$$X = \frac{y(1-R)M_*(z)}{M_{g,i}(z) - M_*(z)} = \frac{y(1-R)f_*^{eff}}{1 - f_*^{eff}} \tag{3.9}$$

in which y is the net yield or the metal mass produced by stars and ejected into the ISM per unit mass in stars and R is the return fraction or the mass fraction of a stellar population that is returned to the ISM. For the yield, a value of 0.0871 is used and a returned fraction of 0.79 (Dayal, Ferrara, and Dunlop, 2013). Under the assumption of perfect mixing, the ejected metal mass is then simply computed as

$$M_{X,ej} = X M_{g,ej}. \tag{3.10}$$

In order to relate the model described above to observational quantities such as the UV LF and SFRD, the UV luminosity and correspondingly the UV magnitude M_{UV} are determined for each galaxy. The stellar population synthesis code STARBURST99 (Leitherer et al., 1999) is used to quantify the initial UV luminosity of a given stellar mass. A fixed metallicity of 5 $\%Z_\odot$ and a Salpeter IMF in the range 0.1-100 $M_\odot$ is assumed. The age of each newly formed stellar population is assumed to be 2 Myr. This results in the following conversion factor from

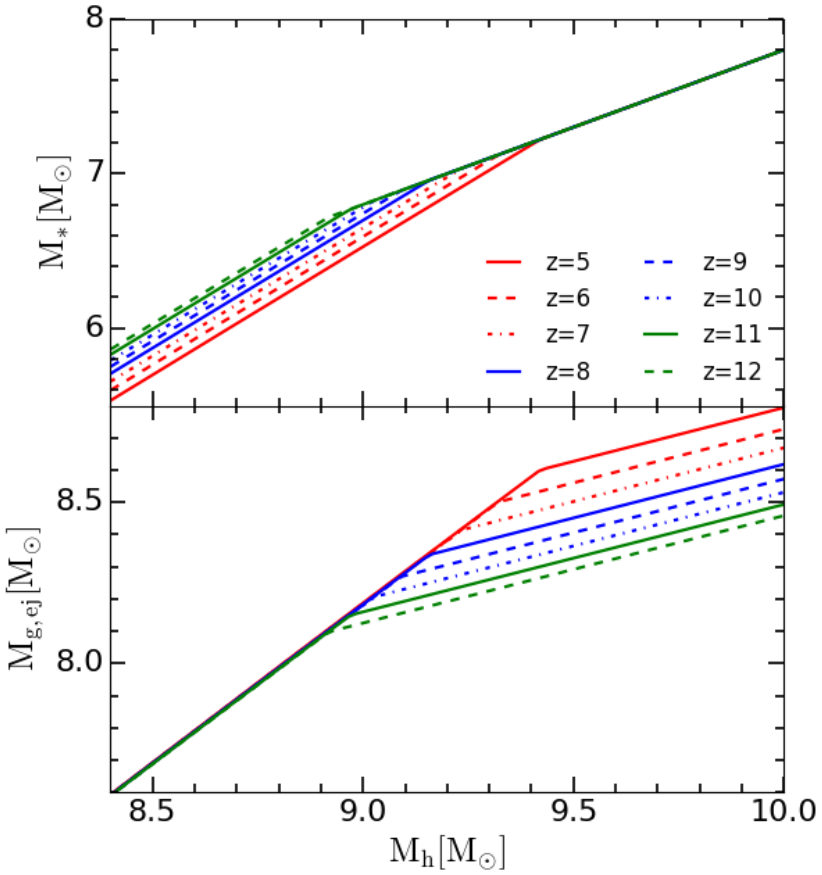

FIGURE 3.2: Stellar mass (upper panel) and ejected gas mass (bottom panel) as a function of halo mass for a star formation star formation efficiency of $f_* = 0.04$ and $f_w = 0.1$, respectively. Both cases are shown for redshifts $z = 5 - 12$ clearly indicating the variation of the depth of the potential of dark matter halos with redshift.

stellar mass to initial UV luminosity per unit wavelength at 1500 Å

$$L_{\lambda,UV} = 10^{33.077} \left(\frac{M_*}{M_\odot}\right) \quad \text{ergs}^{-1}\text{A}^{-1}. \tag{3.11}$$

This can then be converted into a UV luminosity per unit frequency on the ground of dimensional analysis by introducing the conversion factor λ^2/c

$$L_{\nu,UV} = \frac{\lambda^2}{c} L_{\lambda,UV} \quad \text{ergs}^{-1}\text{Hz}^{-1} \tag{3.12}$$

which evaluated at 1500 Å. The received spectral flux density can then be calculated using the expression from Hogg et al. (2002)

$$f_\nu = \frac{(1+z)L_{\nu,UV}}{4\pi D_L^2} \quad \text{ergs}^{-1}\text{Hz}^{-1}\text{cm}^{-2} \tag{3.13}$$

where D_L is the luminosity distance and the factor $(1+z)$ accounts for the change in frequency due to the expansion of the universe. The luminosity distances were obtained from Ned Wright's cosmology calculator (Wright, 2006). In this work, the AB magnitude system is used [1]. Having evaluated the received spectral flux density, the apparent magnitude m_{UV} is evaluated as

[1]The AB magnitude system is defined as the logarithm of the spectral flux density with a zero point at 3631 Jy.

$$m_{UV} = -\frac{5}{2} log(f_\nu) - 48.6 \tag{3.14}$$

in which f_ν has to be in cgs units ($ergs^{-1}Hz^{-1}cm^{-2}$). Using the distance modulus and the K-correction factor (third term on the right) that corrects for differences in flux for a given bandpass caused by the expansion of the universe, the absolute UV magnitude M_{UV} is calculated corresponding to

$$M_{UV} = m_{UV} - 5log(\frac{D_L}{10pc}) + 2.5log(1+z). \tag{3.15}$$

The remaining physical quantity to be determined for each galaxy is the star formation rate. The star formation rate is directly obtained (eq. 3.16) from the UV luminosity using a conversion factor of $\kappa_{UV} = 1.15 \cdot 10^{-28}$ $\mathrm{M_\odot yr^{-1}erg^{-1}sHz}$, which is adopted from Madau and Dickinson (2014).

$$\mathrm{SFR} = \kappa_{UV} \times L_{\nu,UV} \quad \mathrm{M_\odot yr^{-1}} \tag{3.16}$$

Having built the complete formalism, this model is then applied to CDM and three WDM cosmologies, namely 1.5, 3 and 5 keV respectively as follows. First of all, Sheth-Tormen halo mass functions are considered corresponding to the latter cosmologies (Dayal, Mesinger, and Pacucci, 2015). These WDM halo mass functions include both the effect of free-streaming and varying δ_c. For $z = 5$ and 10, these halo mass functions are shown in Fig. 3.3 for CDM, 1.5 ,3 and 5 keV WDM respectively, clearly showing the suppression due to the different WDM cosmologies. The complete set of calculations shown above are applied to each dark matter halo across halo mass range of the Sheth-Tormen halo mass functions in the redshift range of $z = 5 - 12$.

Besides the observables UV LF, SFRD and SMD, the ejected gas mass density and ejected metal mass density are calculated. f_* will be tuned to match the observations and f_w is assumed to be 10%.

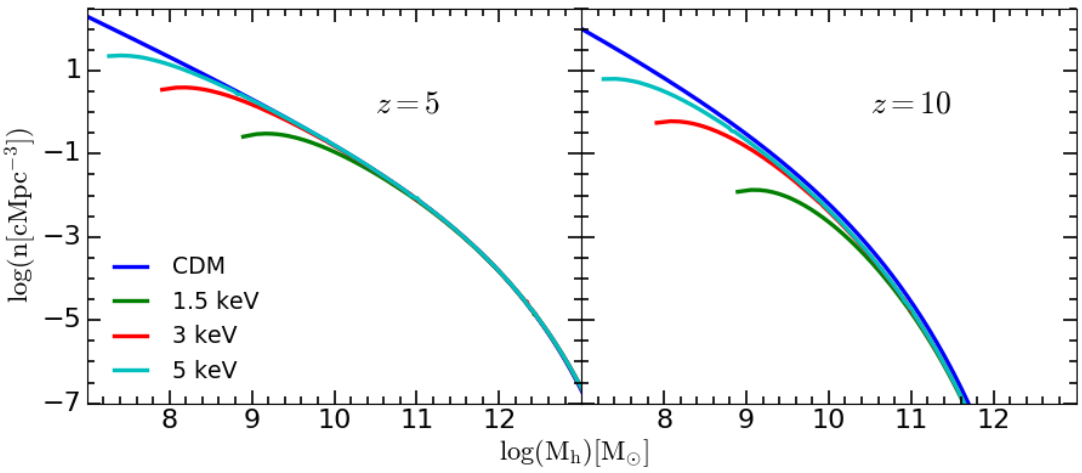

FIGURE 3.3: Shet-Tormen halo mass functions for CDM, 1.5, 3 and 5 keV WDM respectively, as indicated by the different colors. In the left panel, halo mass functions are shown for $z = 5$ and in the right panel for $z = 10$. These WDM halo mass functions include both the effect of free-streaming and variation in δ_c.

3.2 UV LF

Having a model that evaluates M_{UV} for each galaxy belonging to the mass range of the halo mass functions provides us directly with theoretical UV LFs. As the UV LF resembles a powerful probe to compare theoretical number densities of galaxies to observations, the extent of

newly young UV luminous stellar mass assembled in galaxies thus plays an important role and enters with the star formation efficiency variable f_*. The strong dependence of the UV LF on f_*, allows us to tune this parameter in order to match the observed UV LF. A least squares like fashion as explained in the following is used to find the star formation efficiency that best matches the observed UV LFs. First of all, the theoretical UV LFs are interpolated in each cosmology to obtain the theoretical number density of galaxies that corresponds to the observed M_{UV}. For each M_{UV} corresponding to observations, the number density is averaged over all cosmologies. The previous step is justified as f_* is assumed to be a cosmology independent quantity. This method then determines the sum of the absolute differences between the theoretical and observed number densities, and finds the value of f_* that best matches the observed UV LF. For the latter, a range of realizations for f$_*$ is explored. The star formation efficiencies that best match the observed UV LF at $z = 5 - 10$ are listed in Table. 3.1.

TABLE 3.1: Star formation efficiencies matching observed UV LF's

z	f$_*$
5	0.00079
6	0.00098
7	0.00136
8	0.00212
9	0.00278
10	0.00297
11	0.00297†
12	0.00297†

† For $z = 11$ and 12 the same f_* as $z = 10$ is assumed.

This result shows that in order to match observations, f_* requires to decreases towards lower redshifts. From $z = 10$ to $z = 5$, f_* decreases by a factor of ≈ 3.8. This is a consequence of the static nature of this analytic approach, in which the assumption that each halo contains a cosmological gas mass fraction at each redshift, leads to overestimation of the total gas mass bound in dark matter halos that is available for star formation. Since in reality, in most galaxies more and more gas is ejected or consumed by star formation as time proceeds. This overestimation of the gas mass is also evident when one compares the results of this approach to the f_* that is found in Chapter 4 were we track the assembly history of galaxies using merger trees which is a factor of 12 to 44 higher. Since there are no observations at $z > 10$, f_* at is assumed to be the same as at $z = 10$ for redshifts above 10, this assumption is supported by the fact that the results show that f_* seems to evolve more slowly towards higher redshifts.

The resulting UV LF in the range of $z \approx 6 - 11$ for CDM and 1.5, 3 and 5 keV WDM, respectively are shown in Fig. 3.4 together with observationally inferred data. This shows that this analytic approach works well at reproducing the observed UV LF's. The abrupt change in the slope of the faint end of CDM at $z > 7$ marks the transition from $f_*^{eff} = f_*$ to $f_*^{eff} = f_*^{ej}$. A visual interpretation of the effect of the overestimation of the gas mass can be seen in Fig. 3.5. Here, UV LFs are shown that have been calculated using the value of f_* that is required to match the $z = 10$ UV LF across the entire redshift range. Towards lower redshifts, the amount of young UV luminous stellar mass in galaxies is overestimated that in turn results in a systematic shift to brighter UV magnitudes with respect to observations. In the following, we will see how these findings translate into the cosmological assembly of stellar mass.

3.3 Stellar mass density

Now that the model is tuned to match the observed UV LF, the stellar mass assembly is determined and compared to the observations. This will provide a view on the effect of different WDM cosmologies on the stellar mass budget of the universe, and hence will a better understanding of this analytical model. From the stellar mass function that was obtained by

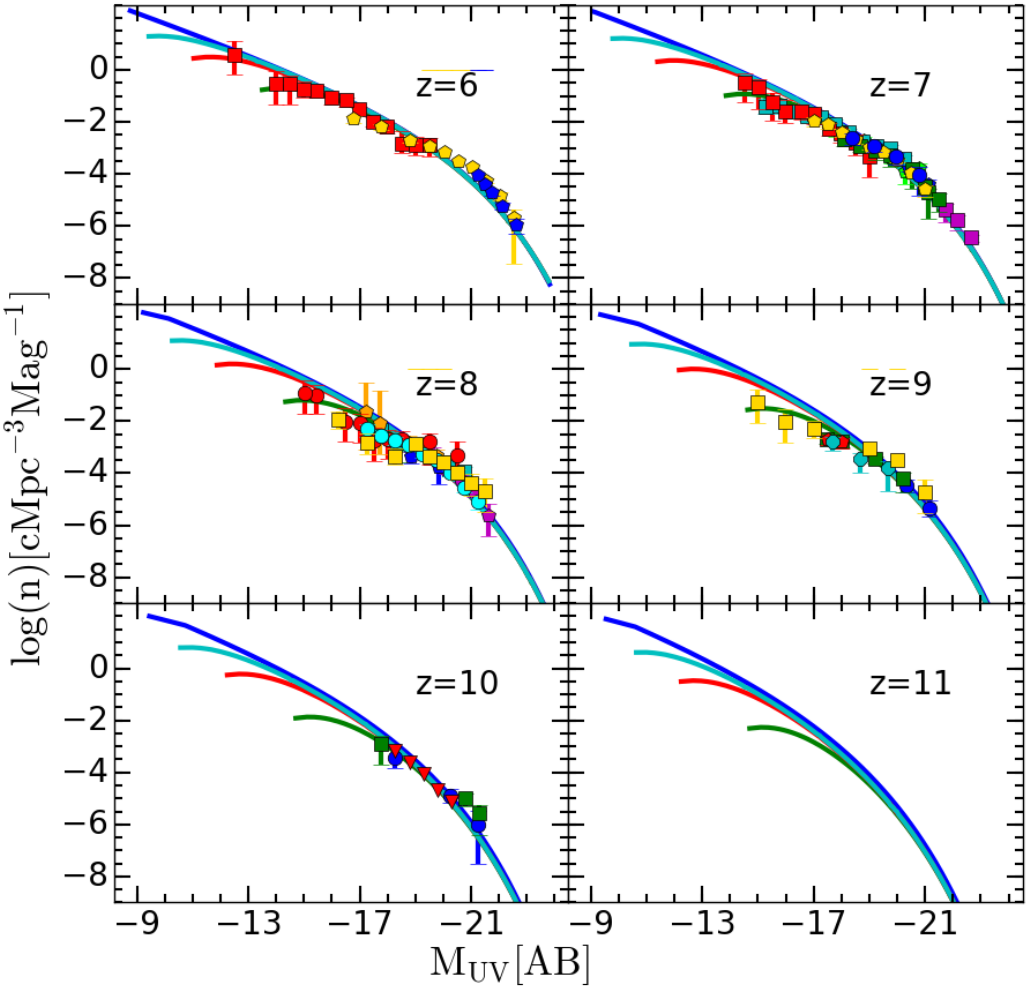

FIGURE 3.4: UV Luminosity functions CDM 1.5, 3, and 5 keV WDM respectively, in the redshift range of $z \approx 6-11$ as highlighted in each panel. In each panel, points show observational data- $z \simeq 6$: Bouwens et al. (2015) gold pentagons, Bowler et al., 2015 blue pentagons, Livermore, Finkelstein, and Lotz (2017) red squares, ; $z \simeq 7$: Castellano et al. (2010) blue pentagons, McLure et al. (2010) green squares, Oesch et al. (2010) blue circles, Bouwens et al. (2011) lime pentagons, McLure et al. (2013) gold pentagons, Bowler et al. (2014) magenta squares, Atek et al. (2015) cyan squares, Livermore, Finkelstein, and Lotz (2017) red squares; $z \simeq 8$: Bouwens et al. (2010) green circles , McLure et al. (2010) blue pentagons, Bouwens et al. (2011) cyan squares, Bradley et al. (2012) magenta pentagons, McLure et al. (2013) cyan circles, Atek et al. (2015) orange pentagons, Livermore, Finkelstein, and Lotz (2017) red circles, Ishigaki et al. (2017) gold squares; $z \simeq 9$: McLure et al. (2013) red pentagons, Oesch et al. (2013) cyan hexagons, McLeod, McLure, and Dunlop (2016) green squares, Bouwens et al. (2016a) blue circles, Ishigaki et al. (2017) gold squares; $z \simeq 10$: Bouwens et al. (2014b) blue circles, Oesch et al. (2014) green squares and Oesch et al. (2014) red triangles showing upper limits.

assigning a stellar mass to each dark matter halo, the stellar mass density is inferred by integrating the stellar mass function at each redshift as

$$SMD = \int_{M_{*l}}^{M_{*u}} n(M_*) dM_* \quad \mathrm{M_\odot cMpc^{-3}} \tag{3.17}$$

where n(M_*) indicates the stellar mass function, M_{*l} represents the stellar mass corresponding to the lowest halo mass of the halo mass function for each cosmology and M_{*u} represents the stellar mass corresponding to the most massive halo which is the same for each cosmology. The integration is performed using the Scipy module *scipy.integrate.simps* that makes use of Simpson's rule. The SMD is calculated for the case in which all galaxies contribute to the

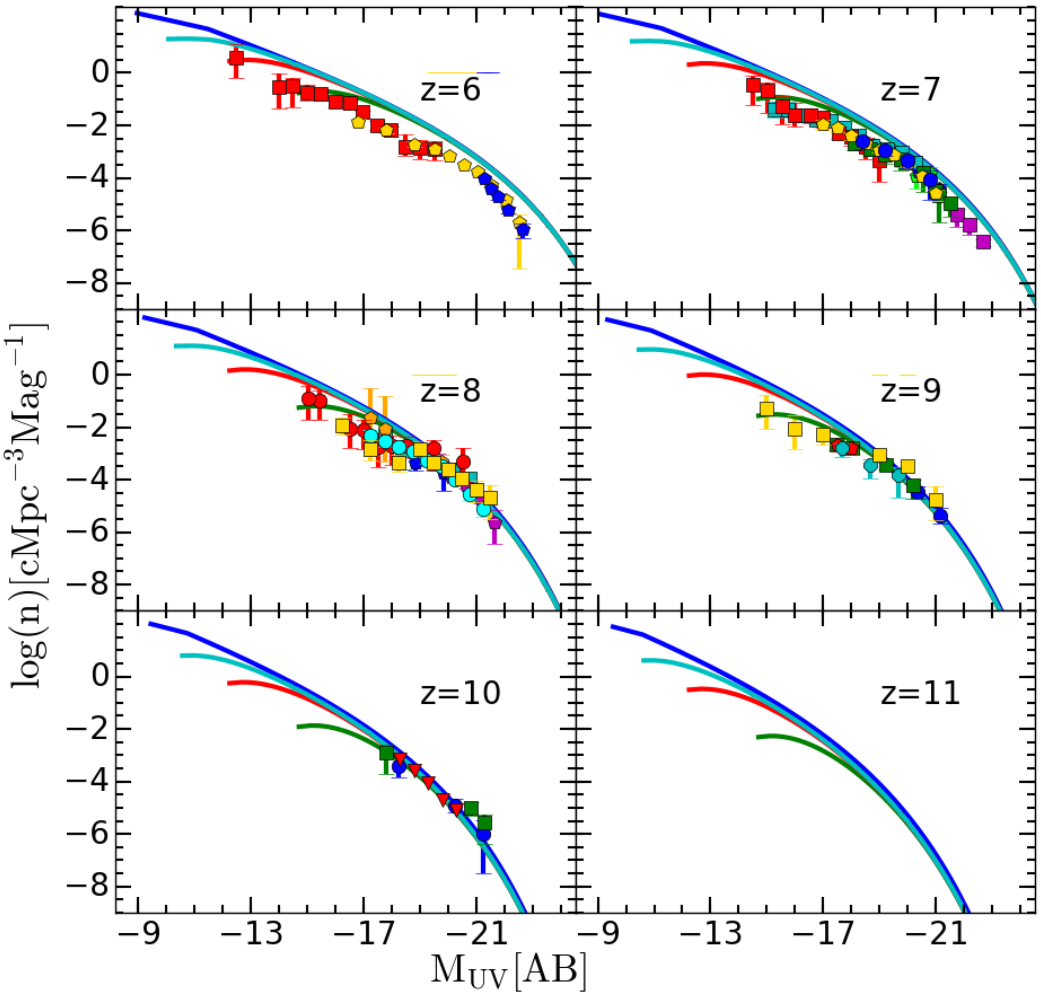

FIGURE 3.5: UV Luminosity functions CDM 1.5, 3, and 5 keV WDM respectively, in the redshift range of $z \approx 6-11$ as highlighted in each panel. In each panel, points show observational data- $z \simeq 6$: Bouwens et al. (2015) gold pentagons, Bowler et al., 2015 blue pentagons, Livermore, Finkelstein, and Lotz (2017) red squares, ; $z \simeq 7$: Castellano et al. (2010) blue pentagons, McLure et al. (2010) green squares, Oesch et al. (2010) blue circles, Bouwens et al. (2011) lime pentagons, McLure et al. (2013) gold pentagons, Bowler et al. (2014) magenta squares, Atek et al. (2015) cyan squares, Livermore, Finkelstein, and Lotz (2017) red squares; $z \simeq 8$: Bouwens et al. (2010) green circles , McLure et al. (2010) blue pentagons, Bouwens et al. (2011) cyan squares, Bradley et al. (2012) magenta pentagons, McLure et al. (2013) cyan circles, Atek et al. (2015) orange pentagons, Livermore, Finkelstein, and Lotz (2017) red circles, Ishigaki et al. (2017) gold squares; $z \simeq 9$: McLure et al. (2013) red pentagons, Oesch et al. (2013) cyan hexagons, McLeod, McLure, and Dunlop (2016) green squares, Bouwens et al. (2016a) blue circles, Ishigaki et al. (2017) gold squares; $z \simeq 10$: Bouwens et al. (2014b) blue circles, Oesch et al. (2014) green squares and Oesch et al. (2014) red triangles showing upper limits.

SMD and for the cases in which only galaxies brighter than $M_{UV} = -15$ and $M_{UV} = -18$ make up the SMD. This allows a view on which galaxies are the main contributers to the stellar mass assembly in different cosmologies and second, enables to compare the SMD to observational inferred measurements at $M_{UV} = -18$. The results for the SMD for which f_* is varied to match observed UV LF at $z = 5-10$ is shown in Fig. 3.6.

As a consequence of the declining f_* at $z < 10$, the build up of stellar mass occurs slower as compared to $z > 10$ where f_* taken to be constant. When all galaxies contributing to the SMD, the decreasing f_* in combination with a decline in f^*_{ej} towards lower redshifts causes the SMD to barely evolve with redshift at $z < 9$ in CDM and 5 keV WDM. When comparing these results to observations at $M_{UV} < -18$, it becomes clear that this approach underestimates the observed SMD by 1 to 2 orders of magnitude. This discrepancy is seen to be higher at lower redshifts and is understood by the fact that these star formation efficiencies are obtained by

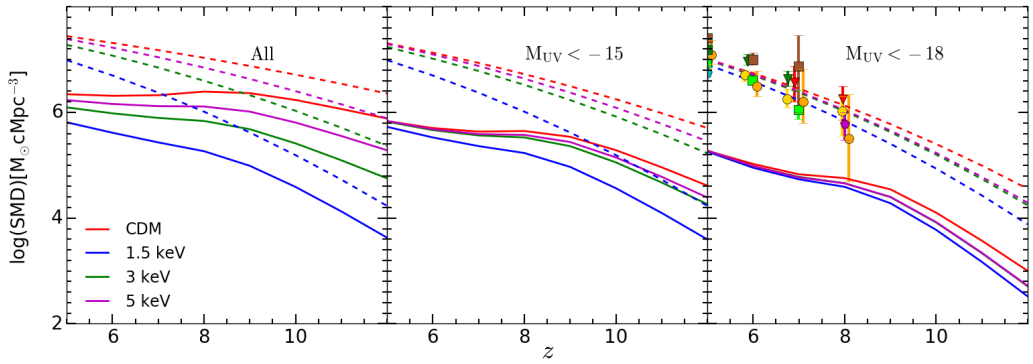

FIGURE 3.6: Stellar mass density as a function of redshift for all galaxies (left panel), galaxies with $M_{UV} < -15$ (middle panel) and $M_{UV} < -18$ (right panel). In each panel, the different colors indicate the different cosmologies. Solid lines indicate the case in which f_* is varied to match observed UV LF at $z = 5-10$ and dashed lines represent the case in which f_* is matched to the observed SMD. Points show SMD observations for a limiting magnitude of $M_{UV} = -18$: Yabe et al. (2009) green square, Labbé et al. (2010a) and Labbé et al. (2010b) red triangles, González et al. (2011) green triangles, Lee et al. (2012) cyan pentagon Labbe et al. (2013) magenta pentagon, Stark et al. (2013) yellow circles, Duncan et al. (2014) brown squares, Grazian et al. (2015) lime squares and Song et al. (2016) orange circles.

matching the observed UV LF for $z = 5 - 10$ which means that only young recently formed UV luminous stars are traced. Because of the latter, the earlier stellar generations which represent the bulk of the stellar mass towards lower redshifts that have significantly lower UV luminosities are not accounted for. This can be understood by considering the time evolution of the UV luminosity for a given stellar mass. The time evolution of the UV Luminosity (at 1500 Å) for a given stellar mass can be expressed as (Dayal et al., 2017)

$$L_{UV}(t) = L_{UV}(0) - 1.33log\left(\frac{t}{t_0}\right) + 0.462 \tag{3.18}$$

where $L_{UV}(0)$ is the initial UV luminosity, t is the time in yr and $t_0 = 2Myr$. This shows that over 20 Myrs of time the UV luminosity decreases an order of magnitude and for 200 Myr two orders of magnitude and further decreases as time proceeds. From this, it is evident that that the fraction of stellar mass being traced by UV decreases as time proceeds. Another point to make is that massive stars dominate the UV emission, whereas low mass stars dominate the stellar mass. The latter most likely contributes to the fact that the SMD is significantly under-estimated when the model is fitted to match the observed UV LF.

Besides the case in which f_* that is tuned to reproduce the UV LF's, we introduce the case in which f_* chosen to match the observed SMD. To match the observed SMD, a star formation efficiency of $f_* \approx 1.2\%$ is required over the entire redshift range. This is also shown in Fig. 3.6, comparing these results with the previous case highlights the difference between the total stellar mass present and the young stellar mass that is traced by strong UV emission. Another difference lies in the evolution of the SMD with redshift, which assembles more rapidly when the model matched matches the observed SMD as apposed to SMD in the case in which the model matches the observed UV LF. Therefore it will be important to distinguish between these two cases, since the stellar mass drives outflows and sets the metallicity, both of these physical quantities are discussed in the next section. As seen in Fig. 3.6, the relative difference between the total stellar mass and the stellar mass traced by UV declines when moving from $M_{UV} < -18$ to all galaxies contributing to the SMD. This is explained by the fact that more massive galaxies for which $M_{UV} < -18$ can form stars at a high efficiency as the ejection efficiency is never reached for these galaxies (Eq. 3.4). Low mass galaxies on the other hand can only form stars at their maximum ejection efficiency which is lower than f_*, thus reducing the difference between the two cases. In the remaining chapter, Cold and WDM cosmologies are compared for the case in which the model matches the observed SMD.

When galaxies with $M_{UV} < -18$ contribute to the SMD, no significant differences between the different cosmologies arise, as these mass scales are too large for WDM to have a significant effect. In the case of galaxies with $M_{UV} < -15$, the effect of WDM becomes evident. For this range of galaxy masses, 1.5 keV WDM starts to diverge from the other cosmologies as this mass range starts to probe the mass regime that suppressed by 1.5 keV WDM. At $z = 12$ CDM harbors $\approx$ 1.5 dex more stellar mass as compared to 1.5 keV WDM reducing to $\approx$ 0.5 dex at $z = 6$. Also 3 keV WDM starts to show a small digression from CDM at high redshift. When considering the contribution of all galaxies to the SMD, significant differences arise between CDM and WDM cosmologies clearly highlighting the increasing mass scale of suppression with decreasing WDM particle mass. It is here that 1.5 keV starts to shows its strong suppressive nature that results in a SMD that is more than 2 dex lower compared to CDM at $z \approx 12$, reducing to $\approx$ 0.75 dex at $z = 6$. These significant differences arise because of the fact that the majority of the stellar mass in CDM resides in low mass galaxies with $M_{UV} > -15$ that are heavily suppressed in 1.5 keV WDM. In 1.5 keV WDM, the stellar mass resides in galaxies for which $M_{UV} < -15$. The latter can be nicely seen by the result that the SMD attributed to all galaxies is identical to the case of $M_{UV} < -15$ for 1.5 keV WDM. The impact of WDM on the SMD becomes more dominant at increasing redshift, and is ascribed to the delay in structure formation in WDM due to the suppression of low mass halos, whereas CDM already had time to assemble structure through the presence of low mass halos. This delay in structure formation causes structure formation to proceed more rapid in WDM as compared to CDM. This is clearly visible when considering the slope of the SMD with redshift, one concludes that it becomes steeper with respect to CDM when approaching lighter particle WDM cosmologies.

3.4 Ejected gas mass density

Having studied the cosmic assembly of stellar mass in different cosmologies, we will see how this translates into the evolution of the total gas mass ejected from galaxies. The ejected gas mass density is obtained in the same manner as the SMD, expect now we are integrating over the ejected gas mass function (galaxy number density as a function of ejected gas mass)

$$\rho_{g,ej} = \int_{M^l{}_{g,ej}}^{M^u{}_{g,ej}} n(M_{g,ej}) dM_{g,ej} \quad M_\odot cMpc^{-3} \tag{3.19}$$

where n($M_{g,ej}$) indicates the ejected gas mass function (number density of galaxies as a function of the ejected gas mass), $M^l{}_{g,ej}$ and $M^u{}_{g,ej}$ how the same meaning as described in the previous section. $\rho_{g,ej}$ for CDM, 1.5, 3 and 5 keV WDM at $z = 5 - 12$ is shown in Fig 3.7. For clarity, again both cases are shown that match the observed UV LF and SMD. Considering all galaxies contributing $\rho_{g,ej}$ for the case in which f_* is matched to the observed UV LFs shows the impact of a decline in f_* with redshift, as $\rho_{g,ej}$ barely evolves in 3 and 5 keV WDM at $z < 8$ and is even lower at $z < 8$ in CDM compared to $z > 8$.

The same trend in the relative differences between the cosmologies as with SMD arises, except that relative differences are more pronounced in $\rho_{g,ej}$. When only galaxies with $M_{UV} < -18$ contribute to the ejected gas mass, first signs of the effects of 1.5 keV WDM start to appear that translate into $\rho_{g,ej}$ at $z = 12$ that is $\approx$ 0.75 dex lower than CDM and towards lower z, the two cosmologies converge. 3 and 5 keV WDM show no notable differences with respect to CDM. In the case of $M_{UV} < -15$, 3 and 5 keV WDM start to peel away from CDM and 1.5 keV WDM again shows the strong suppression on the scales probed by this mass regime that manifests in $\rho_{g,ej}$ being $\approx$ 2 dex lower than CDM at $z = 12$ reducing to 0.85 dex at $z = 6$. Interestingly, $\rho_{g,ej}$ attributed to all galaxies is identical to the case of $M_{UV} < -15$ in 1.5 keV WDM, highlighting the dearth of halos at $M_{UV} > -15$. In addition, 1.5 keV WDM harbors 3.5 dex more ejected gas at $z = 12$ compared to CDM and $\approx$ 1.6 dex at $z = 5$. This large impact shows that low mass galaxies are the main contributers to the ejected gas mass budget. Compared to the SMD, WDM cosmologies have a stronger impact on $\rho_{g,ej}$, because low mass halos that are not present in the WDM cosmologies eject a gas mass that comprises a mass that is significantly larger than the small mass fraction of the initial gas that is turned into stars in these halos that is needed to eject all of their gas (Fig. 3.2).

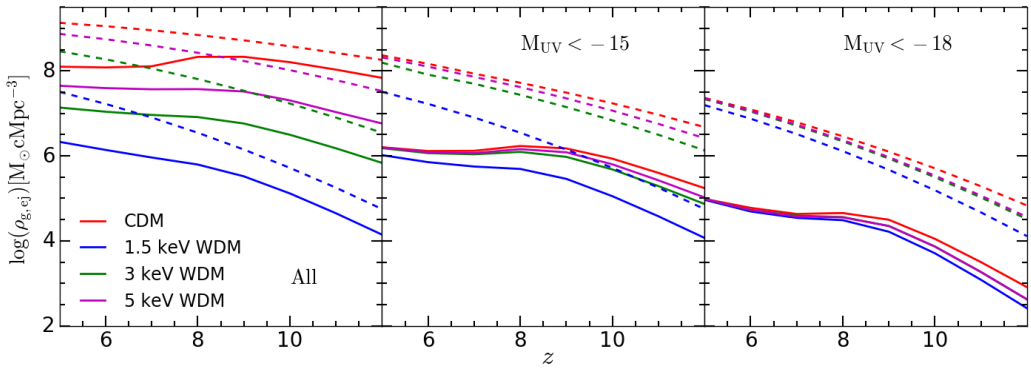

FIGURE 3.7: Ejected gas mass density as a function of redshift in CDM, 1.5, 3 and 5 keV WDM for all galaxies (left panel), galaxies with $M_{UV} < -15$ (middle panel) and $M_{UV} < -18$ (right panel), respectively. In each panel, the different colors indicate the different cosmologies. Solid lines indicate the case in which f_* is varied to match observed UV LF at $z = 5 - 10$ and dashed lines represent the case in which f_* is matched to the observed SMD.

3.5 Ejected metal Mass Density

Before the ejected metal mass is determined, we first consider the metallicity that is calculated according to Eq.3.9 separately for each halo mass. As we will see, the behavior of the metallicity in galaxies is different when considering the model matched to observed UV LFs or to the SMD. In Fig. 3.8 the resulting metallicities are shown as a function of halo mass at various redshifts for the latter two realizations. When the model is matched to observed UV LFs, we find that the metallicity only slightly changes with increasing halo mass for $z > 7$ for the lightest halos ($M_h < 10^{7.4} M_\odot$) and is constant over the entire remaining halo mass range as is the case of $z < 8$. The small variation in metallicty with increasing halo mass at these high redshifts is explained by the fact that $f_*^{eff} = f_{ej}^*$ for these halos, as soon as f_*^{eff} saturates to f^*, the metallicity stays constant because the stellar to gas mass ratio remains unchanged for any halo. The counterintuitive behavior in which the metallicity of a given halo mass lowers with decreasing redshift is because of the decreasing trend of f_* with redshift (Table. 3.1). For a constant and larger value of f_* in the case the model matches the observed SMD, a more intuitive result is found for the metallity. In the $M_h \approx 10^{7-8.6} M_\odot$ range however where the metallicity increases with halo mass over the entire redshift range and remains constant for $M_h > 10^{8.6}$ regardless of the redshift.

From the ejected metal mass of each halo (Eq. 3.10), the overall density of metals in the IGM is evaluated in the same manner as the SMD using the expression

$$\rho_{X,ej} = \int_{M_{X,ej}^l}^{M_{X,ej}^u} n(M_{X,ej}) dM_{X,ej} \quad M_\odot cMpc^{-3}. \tag{3.20}$$

The result of $\rho_{X,ej}$ is shown in Fig. 3.9 for CDM, 1.5, 3 and 5 keV WDM at $z = 5 - 12$. As expected, the relative differences between the different cosmologies are similar to that of the ejected gas mass. We note that in the case the stellar mass traces the observed UV LF, the effect of lower metallicity at lower redshift that is the result of the decline in f_* with redshift is strongly visible. The latter translates into a $\rho_{X,ej}$ that at $z < 9$ decrease for all cosmologies expect for 1.5 keV WDM were it remains approximately constant. This behavior also results in a relative difference between the two different realizations of the model that is up to an order of magnitude larger as compared to $\rho_{g,ej}$. Comparing CDM with 1.5 keV WDM, we find that when all galaxies contribute to the ejected metal mass, CDM harbors 3.5 dex more metal mass in the IGM at $z \approx 12$ and 1.3 dex at $z \approx 5$.
Using this analytic approach, we have shown first estimates of the impact 1.5, 3 and 5 keV WDM cosmologies have on the metal mass ejected into the IGM. In addition, this result indicates that galaxies with $M_{UV} > -15$ are the key metal polluters of the IGM, whereas in 1.5

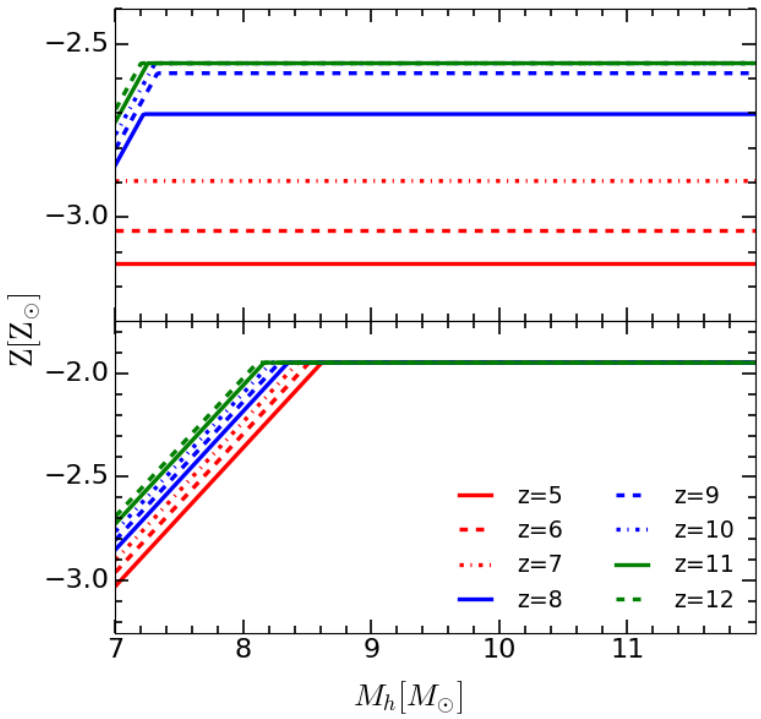

FIGURE 3.8: The gas metallicity as a function of halo mass in the redshift range of $z = 5-12$ as indicated by the different colors. The top panel indicates the metallicty for the case the model is matched to observed UV LF's, the bottom panel shows the results in case the model is matched to the observed SMD.

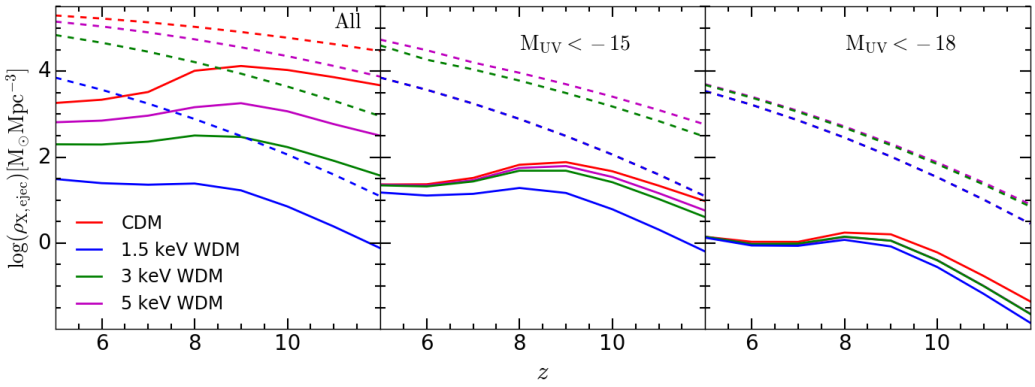

FIGURE 3.9: Ejected metal mass density as a function of redshift in CDM, 1.5, 3 and 5 keV WDM for all galaxies (left panel), galaxies with $\mathrm{M_{UV}} < -15$ (middle panel) and $\mathrm{M_{UV}} < -18$ (right panel), respectively. In each panel, the different colors indicate the different cosmologies. Solid lines indicate the case in which f_* is varied to match observed UV LF at $z = 5 - 10$ and dashed lines represent the case in which f_* is matched to the observed SMD.

keV WDM the key metal polluters are galaxies with $\mathrm{M_{UV}} < -15$. Given that 1.5 keV WDM shows the largest impact on the ejected metal mass, it is this cosmology that we will further pursue in this work. The latter provides a promising base for a further more realistic and precise investigation of the impact of WDM on the metal enrichment of the IGM in the following chapter.

Chapter 4

Semi-Analytic model

THe Semi-analytic approach allows the study of galaxy formation and evolution over cosmic time through a combination of dark matter halo merger trees and analytic recipes regarding baryonic physics that can by applied by hand. The main advantage of semi-analytic models lies in the fact that these are computationally inexpensive compared to detailed N-body/hydrodynamic simulations which accurately trace the formation of galaxies since N-body/hydrodynamic simulations take into account mutual and collective interactions of particles. Semi-analytic models allow for a fast and broad exploration of parameter space, whereas this is not possible with large N-body/hydro simulations. In the first part of this chapter, the construction of a merger tree is explained followed by the baryonic physics involved. In remaining of the chapter, the results are discussed.

4.1 Merger Tree

In order to study assembly of galaxies throughout cosmic time, a prescription describing the distribution and merging history of dark matter halos is needed. A graphical illustration of a merger tree is shown in Fig. 4.1. This figure highlights the formation of massive halos through the assembly (merging) of smaller halos. This highlights the complex merging history a massive halo might have had. At any instant, one generally refers to a parent halo when it is assembled through the merging of smaller halos, the progenitor halos. An example of some parent halos is indicated by the dashed horizontal line in Fig. 4.1. The basis of constructing a merger tree lies in the so called Extended Press Schechter (EPS) formalism or Excursion set formalism that has been developed by Bond et al. (1991). This formalism can derived in the same manner as the one of PS, expect that EPS has a different ansatz as a starting point. This ansatz consists of the assumption that *"the fraction of trajectories with a first upcrossing (FU) of the barrier $\delta_S = \delta_c(t)$ at $S > S_1 = \sigma^2(M_1)$ is equal to the mass fraction that at time t resides in halos with masses $M < M_1$"* (Bosch, 2017). A Graphical illustration of such a trajectory in (δ,S) space in view of the Extended Press Schechter theory is shown in Fig. 4.2, in which the horizontal lines indicate the collapse barrier (δ_c) at different times. The crossing of this barrier by a trajectory leads to a collapsed object with mass variance S_c. This leads to the following conditional EPS mass function

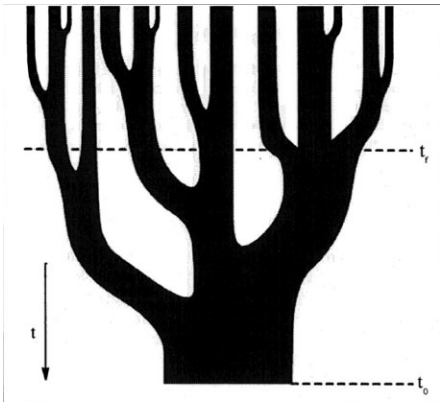

FIGURE 4.1: Graphical illustration of a merger tree in which time evolves from the top to bottom (Lacey and Cole, 1993).

$$f(M_1|M_2)dlnM_1 = \sqrt{\frac{2}{\pi}}\frac{\sigma_1^2(\delta_1-\delta_2)}{[\sigma_1^2-\sigma_2^2]^{\frac{3}{2}}} \times \exp\left[-\frac{1}{2}\frac{(\delta_1-\delta_2)^2}{(\sigma_1^2-\sigma_2^2)}\right]\left|\frac{d\ ln\ \sigma_1}{d\ ln\ M_1}\right| d\ ln\ M_1 \tag{4.1}$$

where $f(M_1|M_2)$ expresses the fraction of mass from halos of with mass M_2 at redshift z_2 that is contained in progenitor halos of mass M_1 at an earlier redshift z_1. δ_1 and δ_2 represent the linear density for collapse at these two redshifts. The root mean square linear density fluctuation extrapolated to $z = 0$ in spheres containing mass M is denoted by $\sigma(M)$ with $\sigma_1 = \sigma(M_1)$ and $\sigma_2 = \sigma(M_2)$.

In this work, the binary merger trees are constructed according to Parkinson, Cole, and Helly (2008) that provide an algorithm that is a modified version of the GALFORM algorithm presented in Cole et al. (2000). If one takes the limit of Eq. 4.2 in which $z_1 \to z_2$, we obtain the following equation that describes average mass fraction of a halo of mass M_2 which was in halos of mass M_1 at a slightly higher redshift z_1

$$\frac{df}{dz_1}\Big|_{z_1=z_2} d\ ln\ M_1\ dz_1 = \sqrt{\frac{2}{\pi}}\frac{\sigma_1^2}{[\sigma_1^2-\sigma_2^2]^{\frac{3}{2}}}\frac{d\delta_1}{dz_1}\left|\frac{d\ ln\ \sigma_1}{d\ ln\ M_1}\right| d\ ln\ M_1\ dz_1. \tag{4.2}$$

This shows that the mean number of progenitors of mass M_1 in which a halo of mass M_2 splits over a redshift interval dz_1 is given by

$$\frac{dN}{dM_1} = \frac{1}{M_1}\frac{df}{dz_1}\frac{M_2}{M_1}dz_1 \quad (M_1 < M_2). \tag{4.3}$$

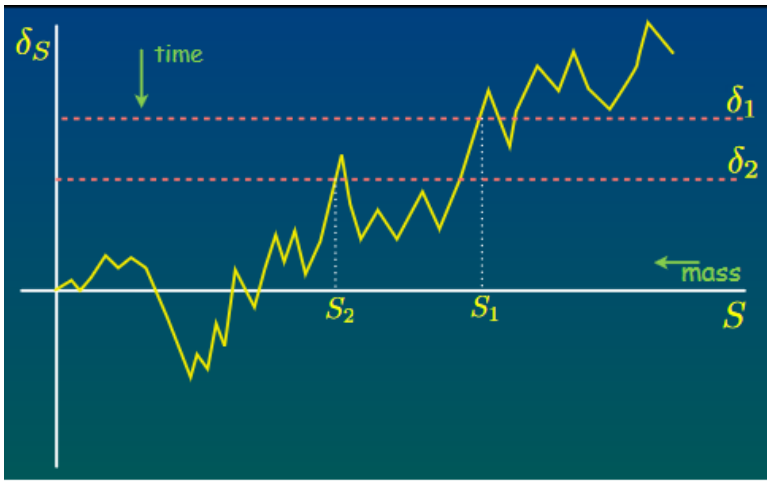

FIGURE 4.2: Graphical illustration of the Extended Press Schechter theory, where the plots shows a trajectory in (δ,S) space. The horizontal lines indicate the collapse barrier at different times. The crossing by a trajectory of this barrier leads to a collapsed object with mass variance S as indicates in the x-axis (Bosch, 2017).

To ensure that each halo only has two progenitors (binarity), the progenitor mass range under consideration is limited to $M_{res} < M_1 < M_2/2$, in which M_{res} specifies the resolution of the merger tree. In this work a resolution of $10^8 M_\odot$ is adopted. This allows us to calculate the mean number of progenitors with mass M_1 in the mass range just specified as

$$P = \int_{M_{res}}^{\frac{M_2}{2}} \frac{dN}{dM_1} dM_1 \tag{4.4}$$

and

$$F = \int_0^{M_{res}} \frac{dN}{dM_1}\frac{M_1}{M_2} dM_1 \tag{4.5}$$

represents the fraction of mass from progenitors below the resolution limit that makes up the final parent. The outcome of Eq. 4.4 and 4.5 depends on the redshift step that is taken through Eq. 4.3. Having the necessary equations, the merger is constructed as follows. At first, a mass and redshift z have to be selected for the final halos in the merger tree. Next, a redshift progression dz_1 is chosen such that P$\ll$1, this makes sure that these halos have 2 progenitors at redshift $z + dz$. Now, a random number H is generated in the interval 0 to 1. In the case of H>P, the main halo is not split in this time interval. However, to account mass that is accreted by halos that are not resolved, the mass over this times step is reduced by $M_2(1 - F)$. In the other case for which $H \leq P$, a random number is generated for M_1 in the range of $M_{res} < M_1 < M_2/2$, in order to form two new halos that have masses of M_1 and $M_2(1 - F) - M_1$. In either case, the mass accreted that resides in the parent halo is given by

$$M_{h,acc} = M_2 F \tag{4.6}$$

The procedure described above is repeated for each newly formed halo at each redshift, leading to the construction of a complete merger tree. For a better agreement of the merger tree with high-resolution N-body simulations, Parkinson, Cole, and Helly (2008) provide a modification to the algorithm of Cole et al. (2000). This modification consists the following substitution

$$\frac{dN}{dM_1} \Rightarrow \frac{dN}{dM_1} G(\sigma_1/\sigma_2, \delta_2/\sigma_2) \tag{4.7}$$

that modifies Eq. 4.3, where for simplicity, the following form is assumed

$$G(\sigma_1/\sigma_2, \delta_2/\sigma_2) = G_0 \left(\frac{\sigma_1}{\sigma_2}\right)^{\gamma_1} \left(\frac{\delta_2}{\sigma_2}\right)^{\gamma_2} \tag{4.8}$$

in which $G_0 = 0.57$, $\gamma_1 = 0.38$ and $\gamma_2 = -0.01$ respectively.

The above prescription to build a merger tree is based on ΛCDM. This prescription by itself however is not sufficient in order to construct merger trees in WDM cosmologies. To construct merger trees in WDM, several modification have to be implemented (Benson et al., 2013). These modifications presented in Benson et al. (2013) are highlighted below.

- ❊ Applying a WDM transfer function to the CDM power spectrum (m_X dependent)
- ❊ Variation of the critical overdensity for collapse δ_c in WDM (m_X dependent)
- ❊ Applying a sharp k-filter
- ❊ Numerically calibrated DM infall rates

The transfer function has to be implemented to take into account the suppression of power on small scales with respect to CDM as a consequence of free-streaming of WDM particles. The nature of the transfer function has been discussed in Section 1.5. A variation of the critical density is needed because of the fact that the velocity dispersion of WDM particles act as a pressure that renders the collapse more difficult on small scales. In Section 1.5 it is shown how δ varies with respect to CDM as a function of the WDM particles mass. As power is suppressed on small scales, it is important to reconsider the filter function. Using the standard real space top-hat filter adopted in CDM in the case of a small scale cut off in WDM, would result in an overestimate in the number of low mass halos, since in the case of the top hat filter, $\sigma(M)$ keeps increasing below the cutoff scale. For this reason, a sharp k-filer function is applied in the case of WDM to assure that the contribution of the long-wavelength modes (small scales) to $\sigma(M)$ remains constant below the cutoff scale. This sharp k-filter is given by

$$W(k|M) = \begin{cases} 1 & \text{when } k \leq k_s(M) \\ 0 & \text{when } k > k_s(M) \end{cases} \tag{4.9}$$

where $k_s = a/R$ and $R = (3M/4\pi\bar{\rho})$. In their work, Benson et al. (2013) choose a to match the location of the cutoff in the HMF to WDM N-body simulations a find a value of $a = 2.5$. In

CDM it is assumed that all mass resides in halos of a given scale, and thus the CDM progenitor mass function contains the overall mass of the parent halo. Since halos for example that are not resolved are accounted for as smooth accretion. Given the the suppression of low mass halos in WDM, the latter is not the case in WDM since, not all trajectories cross the barrier. These trajectories can be viewed as smooth accretion of mass that is not part of a collapsed halo. In WDM merger trees, one thus needs to numerically calibrate DM in-fall rates.

Modified binary merger-trees according to the recipe above were used that have been constructed for 800 (4000) galaxies at $z = 4$ in CDM (1.5 keV WDM), uniformly distributed in the halo mass range Log(M_h) = 9-13 with a resolution of $10^8 M_\odot$ (Dayal, Mesinger, and Pacucci, 2015). This is then scaled to match the Sheth Tormen HMF co-moving number densities at $z = 4$ which is then propagated along the entire merger tree.

In the following, the aspect of galaxy formation is considered by implementing baryonic physics into the dark matter halo merger tree constructed according to the above prescription.

4.2 Baryonic physics

Regarding the baryonic physics, the same formalism for the star formation efficiency, ejected (bound) gas mass is used as described in Section 3.1, however in this case, the detailed evolution of the baryonic content along the merger tree is tracked. In order to track the baryonic content of each DM halo, each individual DM halo is assigned a label to distinguish between different branches of the merger tree and to know which progenitors belong to a given parent halo. In addition, the merger tree allows us to determine whether a halo is the first progenitor of a branch.

The evolution of galaxies starts of course with the first progenitors, and since these halos have no merging history (progenitors), a gas mass is assigned to these first progenitors using a cosmological gas mass fraction

$$M_{g,i}(z) = \frac{\Omega_b}{\Omega_m} M_0(z) \tag{4.10}$$

where M_0 represents the DM mass corresponding to the first progenitor of a given branch. Further, the assumption is used that the accreted DM brings in a cosmological gas mass fraction of

$$M_{g,acc(z)} = \frac{\Omega_b}{\Omega_m} M_{h,acc}(z). \tag{4.11}$$

For each redshift step, the gas content of a given parent halo is determined by the gas mass that has been accreted during the previous time step, plus the gas mass that is brought in by its progenitors. The gas content of a given halo at redshift z is given by

$$M_{g,i}(z) = M_{g,acc}(z) + \sum M_{g,f}(z + \Delta z) \tag{4.12}$$

where the summation runs over the progenitors from the previous redshift and highlights the total gas mass brought in by its progenitors. This progenitor history is shaped by star formation events, gas outflows and accretion of gas. The final gas mass of a parent halo at a given redhsift in terms of the properties of its progenitors is given by $M_{g,f}(z) = \sum M_{g,i}(z + \Delta z) - \sum M_*(z+\Delta z) - \sum M_{g,ej}(z+\Delta z)$. The stellar mass assembled from the gas mass present in a given halo at redshift z ($M_{g,i}(z)$) is obtained through Eq.3.6 and the total stellar mass of a given halo at a given redshift is then given by the sum of the newly formed stellar mass and that brought in by its progenitors.

$$M_{*,tot}(z) = M_*(z) + \sum M_*(z + \Delta z) \tag{4.13}$$

To reconcile, this model consists of two (f_*,f_w) redshift and halo mass independent variables that are varied in order to match to observations. The total UV luminosity is the sum of the UV

luminosity corresponding the newly formed stars and that of the stellar mass that is brought in by progenitors.

$$L_{UV,tot}(z) = L_{UV}(z) + \sum L_{UV}(z + \Delta z) \tag{4.14}$$

The UV luminosity of a given stellar mass evolves with time according to (STARBURST99 (Leitherer et al., 1999))

$$log(L_{UV}(t)) = log(L_{UV}(0)) - 1.37log\left(\frac{t}{t_0}\right) + 0.363 \tag{4.15}$$

in which $L_{UV}(0)$ expresses the initial UV luminosity, t is the time in years and $t_0 = 2Myr$. For $Z_* = 20\%\ Z_\odot$ that is adopted in this work, $L_{UV}(0) = 10^{33.136} ergs^{-1}$ Å^{-1} (Leitherer et al., 1999). To fit the above baryonic components into a global cosmological context, we want to calculate the cosmological density of any given quantity x e.g. stellar mass (SMD) or ejected gas mass density ($\rho_{gas,ej}$) and is given by

$$\rho_x = c\sum n(M_h)x(M_h) \quad \mathrm{M_\odot cMpc^{-3}} \tag{4.16}$$

where the sum adds the contribution of all halos in the merger at a given redshift and c is a rescaling constant that takes into account the distribution of 800(4000) halos over 4 dex of halo mass, and therefore the constant c is $1/200$ for CDM and $1/1000$ for 1.5 keV WDM.

4.3 Cosmological content of $\mathrm{C_{IV}}$ in the IGM $\Omega_{\mathrm{C_{IV}}}$

Now that we have model that tracks the cosmological evolution of the ejected gas mass, we want to connect this to the metal enrichment of the IGM. This means that we have to estimate the amount of metals that has been ejected into the IGM. First of all, the crucial assumption is made in which all metals are assumed to be perfectly mixed with gas. In this work, a halo mass and redshift independent gas phase metallicity of $Z = 20\%\ Z_\odot$ is assumed for each galaxy. This assumption of 20% is based on the mean gas phase metallicity obtained from observations (Madau and Fragos, 2017). The same metallicity is assumed for stars ($Z_* = 20\% Z_\odot$). For high redshifts, this assumption of constant metallicity will most likely result in an over-estimation of the amount of metals present at the highest redshifts considered. An additional point to make is that the observed mean gas phase metallicity is biased towards larger halo masses, by applying the assumption of a constant metallicity to low mass halos that generally have lower metallicities, will result in an over-estimated metal content in low mass halos.

Given the ejected gas mass density, an estimate of the metal enrichment of the IGM can be made using $\mathrm{C_{IV}}$ as a probe that can be observed at high z using quasar spectra. In this work, we define the following relation that determines the universal mass density of $\mathrm{C_{IV}}$ in the IGM

$$\rho_{\mathrm{C_{IV}}}(z) = \rho_{gas,ej}(z) \times Z_{gas} \times f\left(\frac{C}{Z}\right) \times f\left(\frac{C_{IV}}{C}\right)(z) \quad \mathrm{M_\odot cMpc^{-3}} \tag{4.17}$$

in which Z_{gas} is the gas phase metallicity, $f\left(\frac{C}{Z}\right)$ represents the mass fraction of metals that is in C and $f\left(\frac{C_{IV}}{C}\right)$ expresses the fraction of C that is in the triply ionized sate $\mathrm{C_{IV}}$. This direct conversion from the ejected gas mass into the ejected metal mass is justified by the assumption of perfect metal mixing. To obtain $f\left(\frac{C}{Z}\right)$, SNII are assumed to be the main producers of dust in this work. This means that the contribution from AGB stars is neglected, which leads to an under-estimation of the amount of metals present, specifically towards lower redshifts where stars have had sufficient time to evolve into the AGB phase (Tornatore et al., 2007). For the analysis of the metals produced by SNII, simulated yields of core collapse SN from Nomoto et al. (2006) are used. They provide yields for stars with of $Z_* = 20\%Z_\odot$ in the mass range of $13 - 40M_\odot$ for many different metals. For each stellar mass, $f\left(\frac{C}{Z}\right)$ is determined by dividing the C yields by the sum of all metal yields and is plotted in Fig. 4.3. As the lightest stars that produce SN II explosions have a mass of $\approx 8M_\odot$, $f\left(\frac{C}{Z}\right)$ as a function of

stellar mass is extrapolated to $8M_\odot$[1]. Whereas stars with $\geq 40M_\odot$ collapse to black halos and have no significant contribution to the ammount of metals present. This extrapolation at $8M_\odot$ is achieved through fitting a function to the data using least squares [2]. The fitted function is shown in Fig. 4.3.

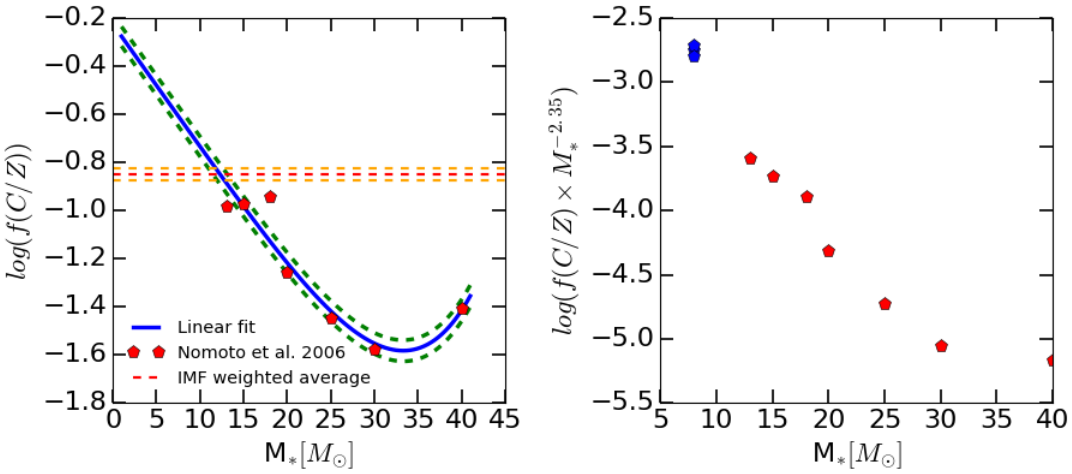

FIGURE 4.3: Left panel: log of $f\left(\frac{C}{Z}\right)$ as a function of stellar mass. Red pentagons indicate the $f\left(\frac{C}{Z}\right)$ obtained using yields from Nomoto et al. (2006). The blue line indicates the fit to the data, the red dotted line shows the IMF weighted $f\left(\frac{C}{Z}\right)$ and dotted green lines indicate the 1σ margin respectively. Right panel: Log of the $f\left(\frac{C}{Z}\right)$ multiplied by the corresponding $M_*^{-2.35}$ as a function of stellar mass. The blue pentagon indicates $f\left(\frac{C}{Z}\right)$ extrapolated at $8M_\odot$ together with its uncertainty and red pentagons again indicate data obtained from Nomoto et al. (2006). It is this plot that is integrated to obtain the IMF weighted $f\left(\frac{C}{Z}\right)$ for $8-40M_\odot$.

The next step consists of determining the Salpeter IMF averaged $f\left(\frac{C}{Z}\right)$ over the mass range of $8-40M_\odot$. The IMF averaged $f\left(\frac{C}{Z}\right)$ is calculated according to Eq. 4.18. To get an impression of the weight of $f\left(\frac{C}{Z}\right)$ for a given stellar mass, $M^{-2.35}f\left(\frac{C}{Z}\right)$ is plotted as a function of the stellar mass in the right panel of Fig. 4.3 .

$$\left\langle f\left(\frac{C}{Z}\right)\right\rangle = \frac{\int_{8M_\odot}^{40M_\odot} M^{-2.35} f\left(\frac{C}{Z}\right)(M)dM}{\int_{8M_\odot}^{40M_\odot} M^{-2.35}dM} \tag{4.18}$$

This also shows that the low mass end of stars that produce SNII dominate the production of carbon. This results in a value of $f\left(\frac{C}{Z}\right) = 0.141^{+0.09}_{-0.08}$ that is not far from the value of 0.178 adopted in Ryan-Weber et al. (2009). The last ingredient required to calculate the density of C_{IV} in the IGM is $f\left(\frac{C_{IV}}{C}\right)$. For this, a redshift dependent value for $f\left(\frac{C_{IV}}{C}\right)$ is assumed, for the fact that the UV background builds up with time and is different at earlier times due do to the different ionization state of the IGM. We let $f\left(\frac{C_{IV}}{C}\right)$ evolve with redshift according to

$$log\left(f\left(\frac{C_{IV}}{C}\right)\right) = -0.35(1+z) + 1.45 \tag{4.19}$$

which results in $f\left(\frac{C_{IV}}{C}\right) = 0.5$ at $z = 4$ and decreases to $f\left(\frac{C_{IV}}{C}\right) = 0.009$ at $z = 9$ and approaches zero towards larger redshifts. This relation includes the range of values for $f\left(\frac{C_{IV}}{C}\right)$ that are found by Keating et al. (2016). The evolution with redshift of $f\left(\frac{C_{IV}}{C}\right)$ is shown in Fig. 4.4. And lastly, to relate this to observations, we convert $\rho_{C_{IV}}$ into $\Omega_{C_{IV}}$ as

$$\Omega_{C_{IV}}(z) = \frac{\rho_{C_{IV}}(z)}{\rho_{crit}(z)}. \tag{4.20}$$

[1]For the extrapolation to $8M_\odot$, the relation is assumed to evolve towards $8M_\odot$ as shown, as the shape of the relation below $13M_\odot$ is not known, this shape could be different and hence result in a lower carbon metal mass fraction.

[2]To obtain the fit to the data that was extrapolated at $8M_\odot$, the scipy.optimize.curve_fit module is used.

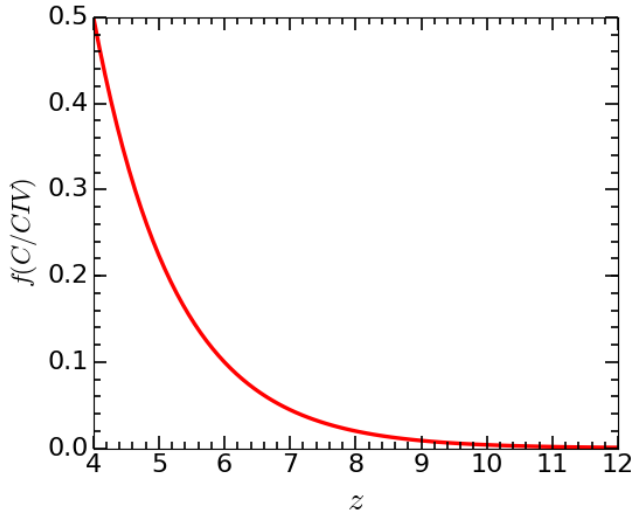

FIGURE 4.4: Redshift evolution of the fraction of carbon that is in the triply ionized state C_{IV}.

Since metals are expected to be concentrated in over-dense regions, we assume the metals to be homogeneously distributed across the IGM in order to infer the cosmological C_{IV} density.

4.4 Feedback prescriptions

Besides the included effect of internal SN feedback, which will be referred to as the fiducial model, the impact of a range of external feedback scenarios is considered. These external feedback scenarios consists of UV feedback that results in photoevaporation of gas from halos. In our case, UV feedback will result in a complete removal of gas from halos below a certain mass that are affected. Three different UV feedback prescriptions are explored, in which all halo masses are affected below $M_h < 10^9 M_\odot$, $v_c < 30 kms^{-1}$ and $v_c < 50 kms^{-1}$. In this model, the following expression for the circular velocity of any given halo is used

$$v_c(M_h, z) \approx [10 G M_h M_\odot H(z)]^{\frac{1}{3}} \propto M_h^{\frac{1}{3}} (1+z)^{\frac{1}{2}} \tag{4.21}$$

which is analogous to eq. 1.20. The redshift dependence of v_c results in an increase of the halo mass that is affected by the UV feedback with decreasing redshift. This is shown in Fig .4.5 in which the halo mass is plotted as a function of redshift that corresponds to $v_c = 30 kms^{-1}$ and $v_c = 50 kms^{-1}$. This trend can be viewed as an analogue to an increasing UVB towards lower redshift. For $v_c = 30 kms^{-1}$ this results in a complete removal of gas from halos with $M_h \leq 10^{8.6}$ at $z = 12$ to $M_h \leq 10^{9.1}$ at $z = 5$. Larger halo mass are affected in the case of $v_c = 50 kms^{-1}$ in which feedback acts on halos with $M_h \leq 10^{9.2}$ at $z = 12$ to $M_h \leq 10^{9.7}$ at $z = 5$. The $M_h = 10^9 M_\odot$ feedback case lies in between the constant v_c feedback cases for $z \geq 5.6$ in which the $v_c = 50 kms^{-1}$ affect larger halo masses with respect to the $M_h = 10^9 M_\odot$ case and for $v_c = 30 kms^{-1}$ approaches the former case.

One however has to bear in mind that in principle, only galaxies embedded in ionized regions should be affect be UV feedback at any redshift. It follows from this assumption that the true case should lie between the fiducial and maximal UV suppression case considered in this work. At high redshift the true case most likely lies close to the fiducial model, since most of the universe is neutral and hence SN feedback will be dominant. As the universe becomes re-ionized towards lower redshifts, UV feedback becomes effective and the true case most likely shifts to the External UV feedback towards lower redshifts. Ideally, the evolution of the volume filling factor of ionized hydrogen with redshift should be taken into account.

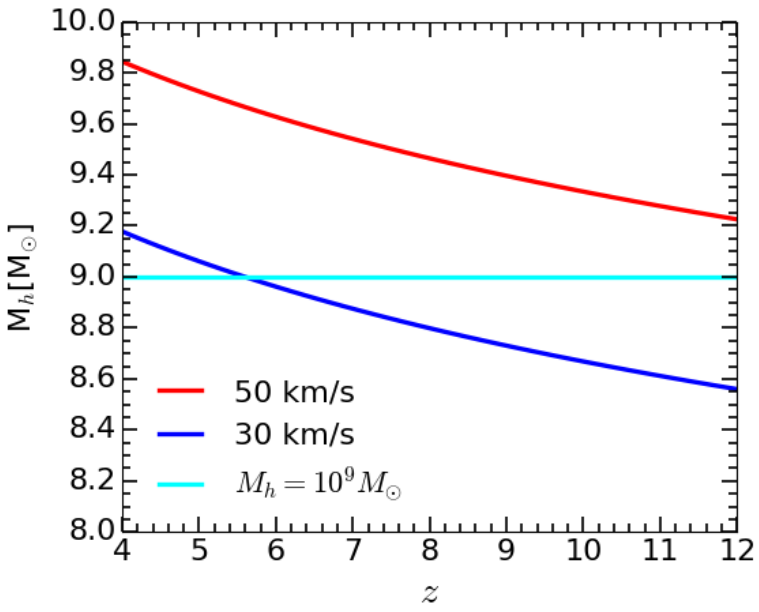

FIGURE 4.5: Halo mass corresponding to $\mathrm{v_c} = 30\,\mathrm{kms^{-1}}$ and $\mathrm{v_c} = 50\,\mathrm{kms^{-1}}$ as a function of redshift given by the blue and red lines respectively. For comparison, the constant case of $M_h = 10^9 M_\odot$ is shown in the form of the cyan line.

4.5 Feedback impact on UV LF

The number density of galaxies as a function of the rest frame UV magnitude (the UV LF) and its redshift evolution resemble a powerful probe to compare predicted galaxy abundances with observations. It is the UV LF to which the model is calibrated by exploring different realizations of f_* that strongly determines the stellar mass residing in massive halos and sets the bright end of the UV LF, whereas f_w largely determines the extents to which low mass halos can from stars and thus shapes the faint end of the UV LF. To match the model to the observed UV LF, an instantaneous star formation efficiency of $f_* = 0.035$ together with a SN II energy fraction coupling to the ISM of $f_w = 0.10$ is required. The resulting UV LF's for this model in the redshift range of $z \approx 6 - 12$ for both Cold and WDM are shown in Fig. 4.6. At each redshift, all feedback realizations for CDM and 1.5 keV WDM are plotted in the same panel in order to gather a good overview of the impact different cosmologies and feedback have on the UV LF. CDM will be discussed first followed by 1.5 keV WDM after which these two cosmologies are compared.

The lack of any external feedback causes the CDM fiducial model to harbor a large number of faint galaxies with $\mathrm{M_h} < 10^9 \mathrm{M_\odot}$ that are SN feedback limited as these halos can only form stars at their maximum allowed efficiency since $\mathrm{f_*^{eff}} = \mathrm{f_*^{ej}} < \mathrm{f_*}$ and thus are only able to transform a small fraction of their gas into stars. The M_{UV} of the fiducial model extend down to faint magnitudes of ≈ -12 at $z = 12$ and ≈ -10 at $z = 6$. As a consequence of the photo-evaporation of gas from low mass halos in the $\mathrm{M_h} < 10^9 \mathrm{M_\odot}$ feedback scenario, the UV LF starts to digress from the fiducial model at $\mathrm{M_{UV}} \approx -15.5$ at $z = 12$ and $\mathrm{M_{UV}} \approx -12.6$ at $z = 6$. In the case of feedback with $\mathrm{v_{circ}} < 30\mathrm{kms^{-1}}$, the cutoff in galaxy number density at $z = 12$ occurs at $\mathrm{M_{UV}} \approx -13.7$ and at $z = 6$ when $\mathrm{M_{UV}} \approx -12.6$. We note that the $\mathrm{v_{circ}} < 30\mathrm{kms^{-1}}$ feedback model peels away from the fiducial model at fainter magnitudes compared to the $\mathrm{M_h} < 10^9 \mathrm{M_\odot}$ model at high redshifts and diverge at about the same magnitude at $z \approx 6$. The fact that the UV magnitudes at which the $\mathrm{M_h} < 10^9 \mathrm{M_\odot}$ and $\mathrm{v_{circ}} < 30\mathrm{kms^{-1}}$ models diverge from the fiducial model approach one other at lower redshifts, is a consequence of the the constant cutoff in circular velocity that results in an increase in halo mass that is affected by feedback with decreasing redshift as explained in Section. 4.4. With $\mathrm{v_{circ}} < 50\mathrm{kms^{-1}}$ that corresponds to $\mathrm{M}_h > 10^{9.2} M_\odot$ at $z = 12$, the opposite trend occurs towards lower redshifts in

which UV magnitude at which the UV LF starts to peel away with respect to the $10^9 M_\odot$ feedback case becomes brighter. For galaxies brighter than the ones effected by $\mathrm{v_{circ}} < 50\mathrm{kms}^{-1}$ UVB, all models are nearly indistinguishable and occurs below $\mathrm{M_{UV}} < -15.8$ at $z = 12$ and $\mathrm{M_{UV}} < -15.2$ at $z = 6$. The fiducial, $\mathrm{M_h} < 10^9\mathrm{M_\odot}$ and $\mathrm{v_{circ}} < 30\mathrm{kms}^{-1}$ model are in excellent agreement with observations. Given the present observational data of the $z \simeq 6 - 7$ UV LF faint end, leads us to suspect that a conservative UVB feedback scenario of $\mathrm{v_{circ}} < 50\mathrm{kms}^{-1}$ in CDM over suppresses the presence of low mass galaxies.

When considering the 1.5 keV WDM fiducial model, the effects of increasing power suppression on smaller scales and in consequence the delay in structure formation become evident. The lack of small scale structure at $z = 12$ translates in a relatively modest and smooth decline in abundance of the faint end with respect to the bright end. As structure assembles towards lower redshifts, the decline in the number density of low mass galaxies becomes steeper and highlights the UV magnitude below which power is substantially suppressed by the nature of 1.5 keV WDM. The UV LF of the $\mathrm{M_h} < 10^9\mathrm{M_\odot}$ feedback model peels away from the fiducial model at $\mathrm{M_{UV}} \leq -16.7$ at $z = 12$ and $\mathrm{M_{UV}} \leq -14.7$ at $z = 6$. Considering the $\mathrm{v_{circ}} < 30\mathrm{kms}^{-1}$ case, we find that this model digresses from the fiducial model at $\mathrm{M_{UV}} \leq -15.5$ at $z = 12$ and the cutoff at $z = 6$ again occurs at the same magnitude as the $\mathrm{M_h} < 10^9\mathrm{M_\odot}$ feedback model. As previously, the $\mathrm{v_{circ}} < 50\mathrm{kms}^{-1}$ realization sets the boundary below which all models are identical and occurs below $\mathrm{M_{UV}} \leq -17.7$ when $z = 12$ and $\mathrm{M_{UV}} \leq -16.3$ at $z = 6$. The v_c cutoffs behave in analogy to the CDM case. Observations are matched by the fiducial, $\mathrm{M_h} < 10^9\mathrm{M_\odot}$ and $\mathrm{v_{circ}} < 30\mathrm{kms}^{-1}$ model, whereas the combined effect of the suppression of low mass halos due to the nature of 1.5 kev WDM and a conservative UVB feedback strongly indicates an over-suppression of galaxies in $\mathrm{v_{circ}} < 50\mathrm{kms}^{-1}$.

Comparing CDM with 1.5 keV WDM, we note that due to the presence of low mass (faint) galaxies in the CDM fiducial model and small scale structure suppression in 1.5 kev WDM, makes the fiducial model render the largest relative difference in number density of low mass galaxies. And as a consequence of a delay structure formation, the relative difference in the number density of galaxies is largest at high redshift and becomes lower with decreasing redshift. The latter is true for all feedback models considered in this work. As opposed to the fiducial model, the least difference in relative number density of galaxies between CDM and 1.5 keV WDM is encountered in the $\mathrm{v_{circ}} < 50\mathrm{kms}^{-1}$ model where this difference at high redshift is dominated by the delay of structure formation in WDM. The lowest relative difference encountered in the number density of galaxies between CDM and 1.5 keV WDM in the case of $\mathrm{v_{circ}} < 50\mathrm{kms}^{-1}$ feedback is because the feedback suppression of the formation of galaxies in CDM mimmicks the effect of the lack of small scale structure in 1.5 keV WDM. These findings show that the relative number density of galaxies in CDM versus 1.5 keV WDM decreases with feedback scenarios in which increasingly larger halo masses are affected by feedback. This highlights the presence of a degeneracy between the effect of feedback in CDM and the effect of power suppression solely due to 1.5 keV WDM. Comparing the bright end of the UV LF towards $z = 6$ between the two cosmologies shows that 1.5 keV WDM hosts a slightly larger number density of brighter galaxies. The latter is merely a consequence of the delay in structure formation that causes the assembled stellar mass to be younger and in turn brighter towards lower redshifts. The younger and in turn brighter stellar mass assembled in 1.5 keV WDM, in addition explains the brighter UV magnitudes in 1.5 keV at which the feedback models peel away from the fiducial model with respect to CDM.

Comparing the bright end of all models to observations, shows that the number densities of bright galaxies towards $z \approx 6$ in this model slightly over-predicts observations. This discrepancy is most likely due to the fact that we ignore dust that contributes to extinction causing our galaxies to be brighter than observed ones.

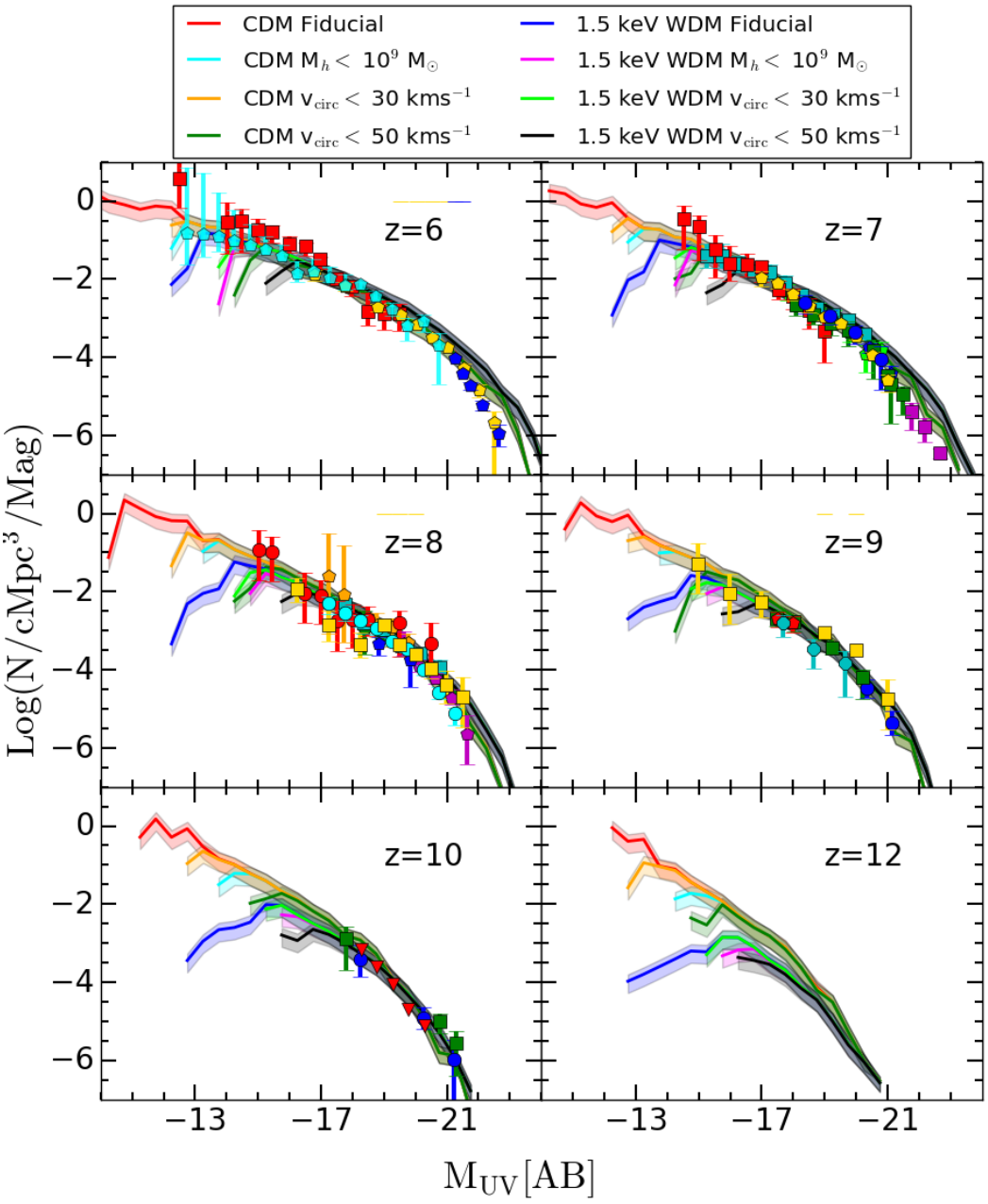

FIGURE 4.6: UV Luminosity Functions for z=6, 7, 8, 9, 10 and 12 respectively. Different colors indicate various feedback schemes in CDM and 1.5 keV WDM as highlighted in the legend on top of the figure. The shaded regions indicate the 1 σ confidence interval. In each panel, points show observational data- $z \simeq 6$: Bouwens et al. (2015) gold pentagons, Bowler et al., 2015 blue pentagons, Bouwens et al. (2016b) cyan pentagons, Livermore, Finkelstein, and Lotz (2017) red squares, ; $z \simeq 7$: Castellano et al. (2010) blue pentagons, McLure et al. (2010) green squares, Oesch et al. (2010) blue circles, Bouwens et al. (2011) yellow pentagons, McLure et al. (2013) gold pentagons, Bowler et al. (2014) magenta squares, Atek et al. (2015) cyan squares, Livermore, Finkelstein, and Lotz (2017) red squares; $z \simeq 8$: Bouwens et al. (2010) green circles , McLure et al. (2010) blue pentagons, Bouwens et al. (2011) cyan squares, Bradley et al. (2012) magenta pentagons, McLure et al. (2013) cyan circles, Atek et al. (2015) orange pentagons, Livermore, Finkelstein, and Lotz (2017) red circles, Ishigaki et al. (2017) gold squares; $z \simeq 9$: McLure et al. (2013) red pentagons, Oesch et al. (2013) cyan hexagons, McLeod, McLure, and Dunlop (2016) green squares, Bouwens et al. (2016a) blue hexagons, Ishigaki et al. (2017) gold squares; $z \simeq 10$: Bouwens et al. (2014b) blue circles, Oesch et al. (2014) green squares and Oesch et al. (2014) red triangles showing upper limits.

4.6 Feedback impact on the stellar mass density

A solid test for any model concerning galaxy formation is presented by the the stellar mass density (SMD) and how it evolves with redshift. Having varied the two free parameters f_* and f_w to match the UV LF as explained above, the resulting theoretical SMD is studied and compared to observational data. To gather a clear picture to what extent observed galaxies and faint galaxies that are yet unaccessible to observations contribute to the SMD at high redshift, we show how feedback affects the SMD when all galaxies contribute to the SMD, galaxies with $\mathrm{M_{UV}} \leq -15$ and $\mathrm{M_{UV}} \leq -18$. The resulting stellar mass densities are shown in Fig. 4.7. CDM is treated first followed by 1.5 keV WDM that in turn allows us to compare the two cosmologies. We find that all feedback prescriptions are nearly indistinguishable

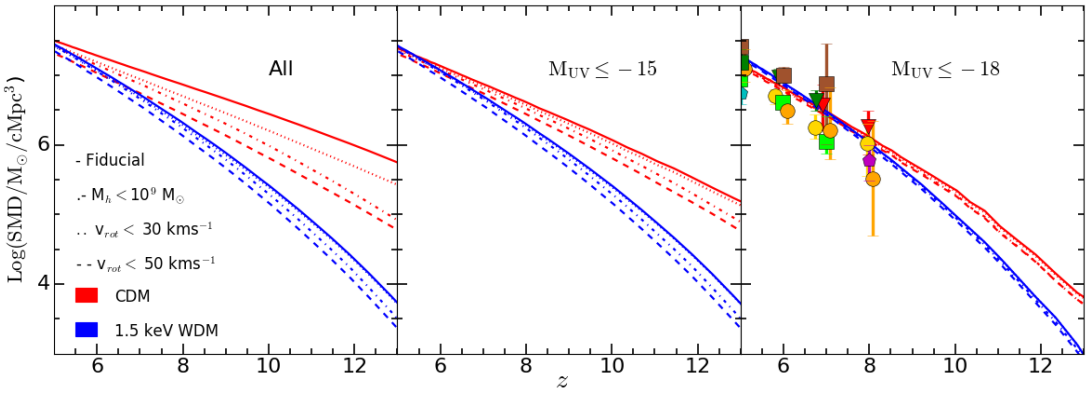

FIGURE 4.7: The stellar mass density as a function of redshift for a contribution to the SMD from all galaxies (left panel), for galaxies that are brighter than $\mathrm{M_{UV}} = -15$ (middle panel) and $\mathrm{M_{UV}} = -18$ (right panel). The red(blue) lines indicate CDM(1.5 keV WDM) where different line-styles indicate different feedback prescriptions: Fiducial model (solid line), UVB feedback with $\mathrm{M_h} < 10^9 \mathrm{M_\odot}$ (dashed-dotted line), $\mathrm{v_{circ}} < 30 \mathrm{kms^{-1}}$ (dotted lines) and $\mathrm{v_{circ}} < 50 \mathrm{kms^{-1}}$ (dashed line). Data points indicate the SMD that has been obseved for M_{UV} <-18: Yabe et al. (2009) green square, Labbé et al. (2010a) and Labbé et al. (2010b) red triangles, González et al. (2011) green triangles, Lee et al. (2012) cyan pentagon, Labbe et al. (2013) magenta pentagon, Stark et al. (2013) yellow circles, Duncan et al. (2014) brown squares, Grazian et al. (2015) lime squares, Song et al. (2016) orange circles.

when considering the contribution to the SMD solely from massive bright galaxies for which $\mathrm{M_{UV}} \leq -18$. This is explained by the fact that most stellar mass is brought in by progenitors that are not affected by UV feedback, whereas low mass galaxies for example in the fiducial model barely contribute to the stellar mass build up of these massive galaxies as these are as they only produce stars at their maximum efficiency of $\mathrm{f_*^{eff}} = \mathrm{f_*^{ej}} < \mathrm{f_*}$ and bring in only a small fraction stellar mass compared to that of the parent of the major branch. A schematic representation of this is provided in Fig. 4.8. In this illustration, it can be seen that low mass progenitors labeled by a,A,b and C respectively, constitute a small mass fraction of the larger parent of the major branch that is highlighted in purple. In terms of stellar mass they are even less significant, and feedback suppressing star formation in these low mass halos barely affects the stellar mass assembly of the major branch. Subtle differences arise when we consider the contribution of galaxies with $\mathrm{M_{UV}} \leq -15$. In this case we start to enter the mass regime in which feedback starts to act. We note that the fiducial and $\mathrm{v_{circ}} < 30 \mathrm{kms^{-1}}$ models are nearly identical for the fact that the these two feedback prescriptions do not affect this halo mass range as opposed to feedback with $\mathrm{v_{circ}} < 50 \mathrm{kms^{-1}}$ that results in a downturn in the SMD. A complete picture of the assembly of stellar mass in the universe and of the effect of different feedback scenarios arises when we consider the stellar mass contribution from all galaxies. In case of the fiducial model, the SMD smoothly increases with almost two orders of magnitude ($10^{5.75-7.5} M_\odot cMpc^{-3}$) over the 900 Myr in the range of $z = 5 - 13$. We find that significant differences arise due to the stronger external UV feedback at which the stellar mass density progressively decreases as a consequence of the downturn in low mass halos that are feedback suppressed.

External UV feedback has to strongest effect at high redshift, for the reason that in the first $\approx$ 350 Myr after the big bang, larger structures have not had sufficient time to assemble and the majority of the stellar mass thus resides in low mass halos at high redshift. Feedback with $\mathrm{v_{circ}} < 50\mathrm{kms}^{-1}$ results in a downturn of an order of magnitude in the SMD at $z \approx 13$ with respect to the fiducial model and reduces to 0.1 dex at $z \approx 5$. With increasing UV feedback, the assembly of the stellar mass in the universe is delayed which in turn results in steeper slopes of the SMD with redshift as larger halos need more time to assemble. This is also evident when regarding the increasing slope of the fiducial model when moving from the all galaxies contributing to the SMD to only bright galaxies with $M_{UV} < -18$. In the case of $\mathrm{v_{circ}} < 50\mathrm{kms}^{-1}$, the evolution of the SMD remains that same when comparing the SMD for all galaxies and galaxies with $M_{UV} < -15$. This highlights that the stellar mass resides in galaxies with $M_{UV} < -15$ in the $\mathrm{v_{circ}} < 50\mathrm{kms}^{-1}$ cosmology. In light of the fiducial model, we find that the stellar mass content on the universe is dominated by low mass halos with $M_{UV} > -15$. Further, all feedback models for $\mathrm{M_{UV}} \leq -18$ match observations that are obtained at the same magnitude limit.

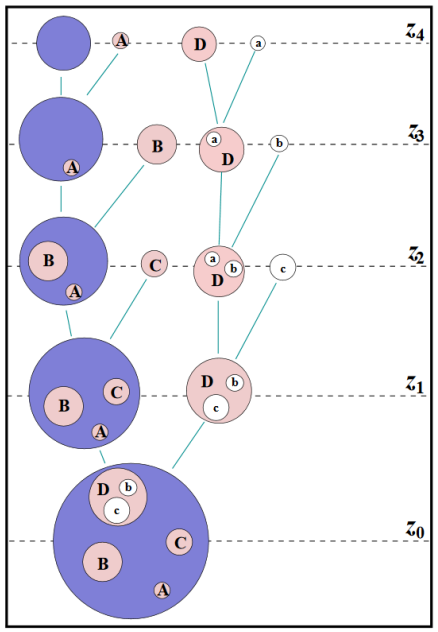

FIGURE 4.8: Schematic representation of a major branch of a given part of a merger tree. This shows that the parent halo of the major branch (shown in purple) dominates the mass, in which the low mass progenitors only contribute minorly to the assembled mass of the larger halo (Giocoli et al., 2010).

When considering 1.5 keV WDM for $\mathrm{M_{UV}} \leq -15$ and $\mathrm{M_{UV}} \leq -18$, we find a similar behavior as in the case of CDM between the different feedback models and attribute this to the same underlying reasoning. The suppressive nature of 1.5 keV WDM becomes evident when we compare the SMD in the fiducial model attributed to all galaxies with that of $\mathrm{M_{UV}} \leq -15$. The fact that the latter two cases are close to being identical, shows that galaxies with $\mathrm{M_{UV}} \geq -15$ are strongly suppressed solely by the nature 1.5 keV WDM. The delay in structure formation ascribed to the lack of small scale structure followed by an accelerated assembly, results in assembly of about 4 orders of magnitude ($10^{3.5-7.4} M_{\odot} cMpc^{-3}$) in the SMD proceeding from $z = 5$ to 13. This is because galaxies in WDM require more time assemble through larger progenitors that are less affected by feedback. As in the case of CDM, all feedback cases in 1.5 keV WDM match the observed SMD.

First of all we note that due to the initial delay in structure formation in 1.5 keV WDM, the build up of structure in turn is progressively accelerated with respect to CDM. This is why over $z = 5 - 13$ 1.5 keV WDM assembles four order of magnitude ($10^{3.5-7.4} M_{\odot} cMpc^{-3}$), whereas for CDM this is two order of magnitude ($10^{5.75-7.5} M_{\odot} cMpc^{-3}$). The relative difference of the SMD in 1.5 keV WDM with respect to CDM between the different feedback models for galaxies with $\mathrm{M_{UV}} < -18$ is only moderate. CDM harbors a factor of about 6 more stellar mass at $z = 13$ and being identical at $z \approx 7$. On the other hand, relative difference in SMD between the two cosmologies considered become interesting when considering all galaxies. The relative difference is the largest for the fiducial model, and resembles the suppression of low mass galaxies in 1.5 keV WDM. In the case of the fiducial model, CDM hosts two orders of magnitude more stellar mass than 1.5 keV WDM at $z = 13$ and being close to identical at $z = 5$. As we progress to stronger feedback scenarios, the relative difference between CDM and WDM decreases. This shows that feedback in CDM is partly degenerate with the effect power suppression due to the nature of 1.5 keV WDM. In the case of $\mathrm{v_{circ}} < 50\mathrm{kms}^{-1}$ feedback, the relative difference in SMD is reduced to a factor of ≈ 20 at $z \approx 13$. In the CDM fiducial model, the majority of stellar mass resides in galaxies with $M_{UV} > -15$, and turns

around for 1.5 keV WDM that hosts most of its stellar mass in galaxies with $M_{UV} < -15$. Given the current observations, the SMD can not be used to disentangle Cold and 1.5 keV WDM.

4.7 Feedback impact on the ejected gas mass density

Having matched the model for both CDM and 1.5 keV WDM to observations, provides us with a solid base to study the impact of feedback and 1.5 keV WDM on the ejected gas mass density ($\rho_{gas,ej}$) that in turn allows us to study the metal enrichment of the IGM in the next section. The resulting $\rho_{gas,ej}$ for CDM and 1.5 keV WDM in the redhsift range of $z \approx 5-13$ are shown in Fig. 4.9 for the contribution of all galaxies, galaxies with $\mathrm{M_{UV}} \leq -15$ and $\mathrm{M_{UV}} \leq -18$. First, our attention is aimed at CDM. In the fiducial model when considering all galaxies, $\rho_{gas,ej}$ is a factor of ≈ 40 larger than the SMD at $z \approx 13$ and a factor of ≈ 20 at $z \approx 5$. This indicates the large contribution of gas that is ejected from the shallow potential wells of low mass galaxies through SN II feedback. This large contribution of low mass galaxies to $\rho_{gas,ej}$ results in a larger effect of feedback as compared to the SMD. At $z \approx 13$ the fiducial models harbors a factor of ≈ 40 more ejected gas as compared to $\mathrm{v_{circ}} < 50\mathrm{kms}^{-1}$ UVB feedback reducing to a factor of ≈ 6 at $z = 5$. The overall behavior of the effect of feedback is similar to SMD. The contribution of low mass galaxies to $\rho_{gas,ej}$ becomes evident when proceeding to the magnitude cuts. Comparing $\rho_{gas,ej}$ from all galaxies with that from galaxies brighter then $M_{UV} = -18$ at $z \approx 13$, shows a difference of 2.5 orders of magnitude. Interestingly, in the case of a magnitude cut of -18, the effect of feedback is significantly more present compared to the case of the SMD in which all models are nearly indistinguishable. This is again explained with the aid of Fig. 4.8, even though these low mass galaxies barely contribute to the stellar mass assembly of massive galaxies, they do eject a significant amount of gas, and this leads to the difference in the UVB feedback when these low mass halos are affected by feedback.

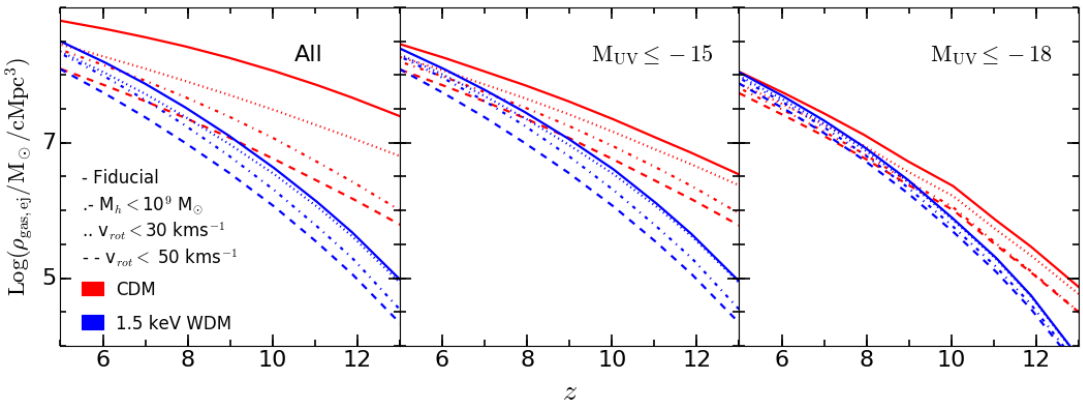

FIGURE 4.9: The ejected gas mass density as a function of redshift for a contribution to the ejected gas mass density from all galaxies (left panel), for galaxies that are brighter than $\mathrm{M_{UV}} = -15$ (middle panel) and $\mathrm{M_{UV}} = -18$ (right panel). The red(blue) lines indicate CDM(1.5 keV WDM) where different line-styles indicate different feedback prescriptions: Fiducial model (solid line), UVB feedback with $\mathrm{M_h} < 10^9\mathrm{M}_\odot$ (dashed-dotted line), $\mathrm{v_{circ}} < 30\mathrm{kms}^{-1}$ (dotted lines) and $\mathrm{v_{circ}} < 50\mathrm{kms}^{-1}$ (dashed line).

Due to the dearth of low mass halos in 1.5 keV WDM, feedback prescriptions have less effect as compared to CDM. In which the fiducial model regarding all galaxies, contains only ≈ 4 times more ejected gas mass compared to the $\mathrm{v_{circ}} < 50\mathrm{kms}^{-1}$ case. A consequence of the lack of low mass halos in 1.5 keV WDM, is that all models are nearly identical when comparing all galaxies contributing to $\rho_{gas,ej}$ and a magnitude cut of -15. Comparing between CDM and 1.5 keV WDM when all galaxies contribute to $\rho_{gas,ej}$ in the case of the fiducial model, $\rho_{gas,ej}$ is ≈ 2.4 order of magnitude larger at $z \approx 13$ reducing to a factor of 2 at $z = 5$. Whereas for galaxies with $\mathrm{M_{UV}} = -18$ this difference reduces to an order or magnitude at $z = 13$ and no difference at $z = 5$. We also note that due to the delay in (and accelerated) structure formation in 1.5 keV WDM, $\rho_{gas,ej}$ increases 3.5 orders of magnitude ($10^{5-8.5} M_\odot cMpc^{-3}$)

over the course of $z \approx 5 - 13$. Whereas in the case of CDM this is 1.3 orders of magnitude ($10^{7.4-8.7} M_{\odot} cMpc^{-3}$). In the following section, we will discuss how this translates into the IGM metal enrichment.

4.8 Metal enrichment of the IGM

After having probed the evolution of $\rho_{gas,ej}$, the formalism of Section. 4.3 is now applied to get an estimate of the metal enrichment of the IGM. The metal enrichment estimate consist of $\Omega_{C_{IV}}$ that has been observationally determined up to $z \approx 6$ using quasar spectra. $\Omega_{\mathrm{C_{IV}}}$ is shown for CDM and 1.5 keV WDM in the redhsift range of $z \approx 5 - 13$ in Fig. 4.10 for the contribution of all galaxies, galaxies with $\mathrm{M_{UV}} \leq -15$ and $\mathrm{M_{UV}} \leq -18$. First of all, it is important to note that all relative differences of all models are identical to that of $\rho_{gas,ej}$, since the conversion from $\rho_{gas,ej}$ to $\Omega_{C_{IV}}$ involves only a scaling which is assumed to be cosmology independent. Regarding the latter, in 1.5 keV WDM the metal enrichment of the IGM is delayed and accelerated with respect to CDM.

Observations at $z > 5$ are only matched in the CDM fiducial model, when all galaxies contribute to $\Omega_{C_{IV}}$. All other models in CDM and 1.5 keV in the case of all galaxies match observations at $z < 5$, they however underestimate the observed $\Omega_{\mathrm{C_{IV}}}$ at $z > 5$. When considering the magnitude cuts of -15 and -18, the models progressively underestimate observations. This implies that within the caveats of this model, this result shows that galaxies with $M_{UV} \geq -15$ dominate the contribution to the mass density of $\mathrm{C_{IV}}$ at $z > 5$ and thus are essential in providing sufficient metals to match the observed mass density of $\mathrm{C_{IV}}$.

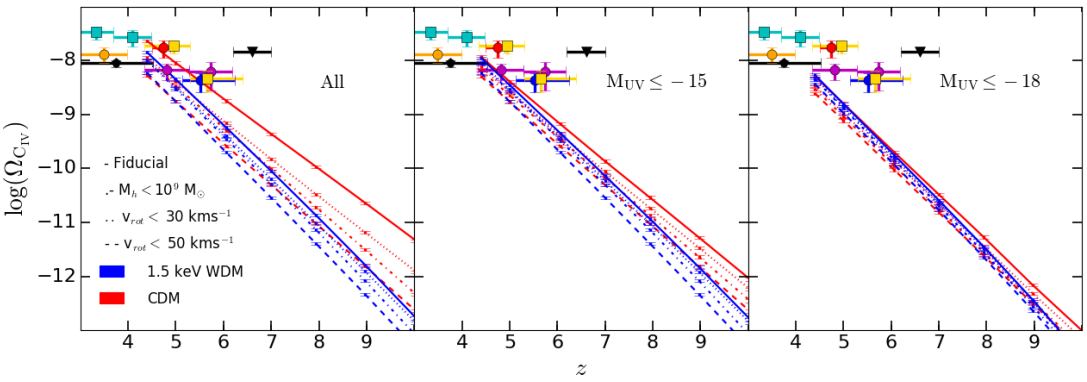

FIGURE 4.10: The cosmological content of $\mathrm{C_{IV}}$ in the IGM ($\Omega_{\mathrm{C_{IV}}}$) as a function of redshift for a contribution to the ejected gas mass density from all galaxies (left panel), for galaxies that are brighter than $\mathrm{M_{UV}} = -15$ (middle panel) and $\mathrm{M_{UV}} = -18$ (right panel). The red(blue) lines indicate CDM(1.5 keV WDM) where different line-styles indicate different feedback prescriptions: Fiducial model (solid line), UVB feedback with $\mathrm{M_h} < 10^9 \mathrm{M_\odot}$ (dashed-dotted line), $\mathrm{v_{circ}} < 30 \mathrm{kms^{-1}}$ (dotted lines) and $\mathrm{v_{circ}} < 50 \mathrm{kms^{-1}}$ (dashed line). Errorbars indicate the uncertainty in the extrapolated yield. Points indicate observational data: Pettini et al. (2003) red circle, D'Odorico et al. (2010) orange circle, Simcoe et al. (2011) gold squares, Cooksey et al. (2013) black pentagon, D'Odorico et al. (2013) magenta circles, Boksenberg and Sargent (2015) cyan squares, D'iaz et al. (2016) blue circle Bosman et al. (2017) black triangle showing an upper limit.

These results for the metal enrichment of the IGM show a degeneracy between the nature of dark matter and the baryonic feedback prescriptions that have been explored in this work. This emphasizes the fact that a dearth of low mass halos (in light WDM models) has a similar impact as increasing the external (UV) feedback in the CDM model. Given the current observations, we can within the caveats of the model rule out 1.5 keV WDM and all CDM scenarios except the fiducial one.

Chapter 5

Conclusion

In this work, the impact of 1.5 keV WDM on the metal enrichment of the IGM has been investigated and was motived by the fact that the number of low mass halos is suppressed in light particle WDM cosmologies. Since low mass halos are thought to be effective at polluting the IGM with metals in light of their shallow potential wells, one naturally expects less metal in the IGM in WDM. First of all, we have shown the dearth of low mass halos in WDM with respect to CDM in terms of the DM halo mass density for 1.5, 3 and 5 keV WDM respectively, in which 1.5 keV WDM causes the strongest effect on the number of low mass halos. The first part of this work consisted of an analytical approach to gain familiarity with the physics involved in galaxy formation and in addition to get a rough estimate of impact different WDM cosmologies have on the metal mass ejected into the IGM.

The last and main part of this work was devoted to the determination of the metal enrichment of the IGM using a semi-analytical model with which the assembly history of each galaxy is tracked and in turn provided a more accurate estimate of the ejected metal mass. In each cosmology, we explored four different feedback scenarios, SN feedback (fiducial model) and external UV feedback that results in a complete removal of baryons in halos with a mass below, $M_h < 10^9 M_\odot$, $v_c < 30 kms^{-1}$ and $v_c < 50 kms^{-1}$. In this approach we focused on CDM and 1.5 keV WDM since it results in the largest dearth of low mass halos.

In this model, two redshift and halo mass independent parameters, the star formation efficiency f_* and the SNII energy available to drive winds f_w have been varied to match observations. A combination of $f_* = 3.5\%$ and $f_w = 10\%$ was needed to match observations. We have investigated the effect of feedback on the UV LF, SMD and $\rho_{gas,ej}$ in CDM and 1.5 keV WDM and show a degeneracy between the nature of dark matter and the baryonic feedback prescriptions considered in this work. In other words, external feedback in CDM has a similar effect as the suppression of low mass halos in 1.5 keV WDM. The main contributers to the SMD and $\rho_{gas,ej}$ in CDM are galaxies with $M_{UV} \geq -15$ and shifts to halos with $M_{UV} \leq -15$ in 1.5 keV WDM.

The metal enrichment of the IGM has been quantified in terms of the triply ionized carbon C_{IV} mass that allowed us to compare the results to observations. The only model that matches C_{IV} observations at $z > 5$ is the CDM fiducial model, when all galaxies contribute to $\Omega_{C_{IV}}$. Within the caveats of this model, this result shows that galaxies with $M_{UV} > -15$ dominate the contribution to the mass density of C_{IV} at $z > 5$ in CDM and thus are essential in providing sufficient metals to the IGM. Galaxies with $M_{UV} < -15$ in 1.5 keV WDM on the other hand dominate the contribution to $\Omega_{C_{IV}}$. In 1.5 keV WDM, the metal enrichment of the IGM is delayed and in turn accelerated with respect to CDM as a consequence of the lack of small scale structure at high redshift.

Within the caveats of this model, we can rule out 1.5 keV WDM and all CDM scenarios except the fiducial one.

Acknowledgements

First of all, I would like to thank you Pratika for all your time, effort and honesty. I really enjoyed the scientific discussions we have had :). And I know that this is my field of interest. Thank you for having granted me the opportunity to go to EWASS, it was a very nice and usefull experience. I really look forward to the 4 years ahead of us in which the experience and knowledge I have gathered over the last year will be proven to be usefull.

Thank you Eifion, Frits, Folkert (was nice to grow these plants ;)), Nikki, Maik for the pleasant time in the office, and of course I thank all of my other fellow students not listed here for the enjoyable atmosphere.

Mama, Florian en Papa, Ik dank jullie van harte voor jullie ondersteuning en aanmoediging!!

Bibliography

Adhikari, R. et al. (2017). "A White Paper on keV sterile neutrino Dark Matter". In: *Journal of Cosmology and Astroparticle Physics* 1, 025, p. 025. DOI: 10.1088/1475-7516/2017/01/025. arXiv: 1602.04816 [hep-ph].

A.Peacock, John (2010). *Cosmological Physics*. Cambridge University Press.

Atek, H. et al. (2015). "Are Ultra-faint Galaxies at z = 6-8 Responsible for Cosmic Reionization? Combined Constraints from the Hubble Frontier Fields Clusters and Parallels". In: ApJ 814, 69, p. 69. DOI: 10.1088/0004-637X/814/1/69. arXiv: 1509.06764.

Barkana, R., Z. Haiman, and J. P. Ostriker (2001). "Constraints on Warm Dark Matter from Cosmological Reionization". In: ApJ 558, pp. 482–496. DOI: 10.1086/322393. eprint: astro-ph/0102304.

Barkana, R. and A. Loeb (2001). "In the beginning: the first sources of light and the reionization of the universe". In: *Physics Reports* 349, pp. 125–238. DOI: 10.1016/S0370-1573(01)00019-9. eprint: astro-ph/0010468.

Baugh, C. M. (2006). "A primer on hierarchical galaxy formation: the semi-analytical approach". In: *Reports on Progress in Physics* 69, pp. 3101–3156. DOI: 10.1088/0034-4885/69/12/R02. eprint: astro-ph/0610031.

Baur, J. et al. (2016). "Lyman-alpha forests cool warm dark matter". In: *Journal of Cosmology and Astroparticle Physics* 8, 012, p. 012. DOI: 10.1088/1475-7516/2016/08/012. arXiv: 1512.01981.

Becker, G. D. et al. (2015). "Evidence of patchy hydrogen reionization from an extreme Lyα trough below redshift six". In: MNRAS 447, pp. 3402–3419. DOI: 10.1093/mnras/stu2646. arXiv: 1407.4850.

Benson, A. J. (2010). "Galaxy formation theory". In: Phys. Rep. 495, pp. 33–86. DOI: 10.1016/j.physrep.2010.06.001. arXiv: 1006.5394.

Benson, A. J. et al. (2013). "Dark matter halo merger histories beyond cold dark matter - I. Methods and application to warm dark matter". In: MNRAS 428, pp. 1774–1789. DOI: 10.1093/mnras/sts159. arXiv: 1209.3018.

Birrer, S., A. Amara, and A. Refregier (2017). "Lensing substructure quantification in RXJ1131-1231: A 2 keV lower bound on dark matter thermal relic mass". In: *ArXiv e-prints*. arXiv: 1702.00009.

Bode, P., J. P. Ostriker, and N. Turok (2001). "Halo Formation in Warm Dark Matter Models". In: *The Astrophysical Journal* 556, pp. 93–107. DOI: 10.1086/321541. eprint: astro-ph/0010389.

Boksenberg, A. and W. L. W. Sargent (2015). "Properties of QSO Metal-line Absorption Systems at High Redshifts: Nature and Evolution of the Absorbers and New Evidence on Escape of Ionizing Radiation from Galaxies". In: ApJS 218, 7, p. 7. DOI: 10.1088/0067-0049/218/1/7. arXiv: 1410.3784.

Bond, J. R. et al. (1991). "Excursion set mass functions for hierarchical Gaussian fluctuations". In: ApJ 379, pp. 440–460. DOI: 10.1086/170520.

Bosch, Frank van den (2017). *Theory of Galaxy Formation Lecture 10: Merger Trees & Halo Bias*. URL: http://www.astro.yale.edu/vdbosch/astro610_lecture10.pdf (visited on 07/06/2017).

Bosman, S. E. I. et al. (2017). "A deep search for metals near redshift 7: the line-of-sight towards ULAS J1120+0641". In: *ArXiv e-prints*. arXiv: 1705.08925.

Bouwens, R. J. et al. (2010). "z $\sim$ 7 Galaxy Candidates from NICMOS Observations Over the HDF-South and the CDF-South and HDF-North Goods Fields". In: *Astrophysical Journal* 725, pp. 1587–1599. DOI: 10.1088/0004-637X/725/2/1587. arXiv: 1003.1706.

Bouwens, R. J. et al. (2011). "Ultraviolet Luminosity Functions from 132 z $\simeq$ 7 and z $\simeq$ 8 Lyman-break Galaxies in the Ultra-deep HUDF09 and Wide-area Early Release Science WFC3 IR Observations". In: ApJ 737, 90, p. 90. DOI: 10.1088/0004-637X/737/2/90. arXiv: 1006.4360 [astro-ph.CO].

Bouwens, R. J. et al. (2014a). "A Census of Star-forming Galaxies in the Z ˜ 9-10 Universe based on HST+Spitzer Observations over 19 Clash Clusters: Three Candidate Z ˜ 9-10 Galaxies and Improved Constraints on the Star Formation Rate Density at Z ˜ 9.2". In: ApJ 795, 126, p. 126. DOI: 10.1088/0004-637X/795/2/126. arXiv: 1211.2230.

Bouwens, R. J. et al. (2014b). "UV Luminosity Functions at redshifts z˜4 to z˜10: 11000 Galaxies from HST Legacy Fields". In: *ArXiv:1403.4295*. arXiv: 1403.4295.

Bouwens, R. J. et al. (2015). "UV Luminosity Functions at Redshifts z $\sim$ 4 to z $\sim$ 10: 10,000 Galaxies from HST Legacy Fields". In: ApJ 803, 34, p. 34. DOI: 10.1088/0004-637X/803/1/34. arXiv: 1403.4295.

Bouwens, R. J. et al. (2016a). "The Bright End of the z $\sim$ 9 and z $\sim$ 10 UV Luminosity Functions Using All Five CANDELS Fields*". In: ApJ 830, 67, p. 67. DOI: 10.3847/0004-637X/830/2/67. arXiv: 1506.01035.

Bouwens, R. J. et al. (2016b). "The z˜6 Luminosity Function Fainter than -15 mag from the Hubble Frontier Fields: The Impact of Magnification Uncertainties". In: *ArXiv e-prints*. arXiv: 1610.00283.

Bowler, R. A. A. et al. (2014). "The bright end of the galaxy luminosity function at z $\simeq$7: before the onset of mass quenching?" In: MNRAS 440, pp. 2810–2842. DOI: 10.1093/mnras/stu449. arXiv: 1312.5643 [astro-ph.CO].

Bowler, R. A. A. et al. (2015). "The galaxy luminosity function at z $\simeq$ 6 and evidence for rapid evolution in the bright end from z $\simeq$ 7 to 5". In: MNRAS 452, pp. 1817–1840. DOI: 10.1093/mnras/stv1403. arXiv: 1411.2976.

Boylan-Kolchin, M., J. S. Bullock, and M. Kaplinghat (2011). "Too big to fail? The puzzling darkness of massive Milky Way subhaloes". In: *Monthly Notices of the Royal Astronomical Society* 415, pp. L40–L44. DOI: 10.1111/j.1745-3933.2011.01074.x. arXiv: 1103.0007 [astro-ph.CO].

— (2012). "The Milky Way's bright satellites as an apparent failure of ΛCDM". In: *Monthly Notices of the Royal Astronomical Society* 422, pp. 1203–1218. DOI: 10.1111/j.1365-2966.2012.20695.x. arXiv: 1111.2048 [astro-ph.CO].

Bradley, L. D. et al. (2012). "The Brightest of Reionizing Galaxies Survey: Constraints on the Bright End of the z ˜ 8 Luminosity Function". In: ApJ 760, 108, p. 108. DOI: 10.1088/0004-637X/760/2/108. arXiv: 1204.3641 [astro-ph.CO].

Castellano, M. et al. (2010). "The bright end of the z ˜ 7 UV luminosity function from a wide and deep HAWK-I survey". In: A&A 524, A28, A28. DOI: 10.1051/0004-6361/201015195. arXiv: 1007.5396 [astro-ph.CO].

Ciardi, B. and A. Ferrara (2005). "The First Cosmic Structures and Their Effects". In: Space Sci. Rev. 116, pp. 625–705. DOI: 10.1007/s11214-005-3592-0. eprint: astro-ph/0409018.

Cole, S. et al. (2000). "Hierarchical galaxy formation". In: MNRAS 319, pp. 168–204. DOI: 10.1046/j.1365-8711.2000.03879.x. eprint: astro-ph/0007281.

Colless, M. (1999). "First results from the 2dF Galaxy Redshift Survey". In: *Philosophical Transactions of the Royal Society of London Series A* 357, p. 105. DOI: 10.1098/rsta.1999.0317. eprint: astro-ph/9804079.

Cooksey, K. L. et al. (2013). "Precious Metals in SDSS Quasar Spectra. I. Tracking the Evolution of Strong, 1.5 $<$ z $<$ 4.5 C IV Absorbers with Thousands of Systems". In: ApJ 763, 37, p. 37. DOI: 10.1088/0004-637X/763/1/37. arXiv: 1204.2827.

Dayal, P., A. Ferrara, and J. S. Dunlop (2013). "The physics of the fundamental metallicity relation". In: MNRAS 430, pp. 2891–2895. DOI: 10.1093/mnras/stt083. arXiv: 1202.4770.

Dayal, P., A. Mesinger, and F. Pacucci (2015). "Early Galaxy Formation in Warm Dark Matter Cosmologies". In: ApJ 806, 67, p. 67. DOI: 10.1088/0004-637X/806/1/67. arXiv: 1408.1102.

Dayal, P. et al. (2014). "Essential physics of early galaxy formation". In: *Monthly Notices of the Royal Astronomical Society* 445, pp. 2545–2557. DOI: 10.1093/mnras/stu1848. arXiv: 1405.4862.

Dayal, P. et al. (2017). "Reionization and Galaxy Formation in Warm Dark Matter Cosmologies". In: ApJ 836, 16, p. 16. DOI: 10.3847/1538-4357/836/1/16. arXiv: 1501.02823.

Dayal, Pratika (2016). *Formation and Evolution of Galaxies*. Lecture Course University of Groningen.

de Souza, R. S. et al. (2013). "Constraints on warm dark matter models from high-redshift long gamma-ray bursts". In: *Monthly Notices of the Royal Astronomical Society* 432, pp. 3218–3227. DOI: 10.1093/mnras/stt674. arXiv: 1303.5060 [astro-ph.CO].

Del Popolo, A. and M. Le Delliou (2014). "A unified solution to the small scale problems of the ΛCDM model II: introducing parent-satellite interaction". In: *Journal of Cosmology and Astroparticle Physics* 12, 051, p. 051. DOI: 10.1088/1475-7516/2014/12/051. arXiv: 1408.4893.

— (2017). "Small Scale Problems of the ΛCDM Model: A Short Review". In: *Galaxies* 5, p. 17. DOI: 10.3390/galaxies5010017. arXiv: 1606.07790.

D'iaz, C. G. et al. (2016). "Tracking the chemical history of the Universe: the density of CIV at z$\sim$ 6". In: *Boletin de la Asociacion Argentina de Astronomia La Plata Argentina* 58, pp. 54–56.

Dodelson, S. and L. M. Widrow (1994). "Sterile neutrinos as dark matter". In: *Physical Review Letters* 72, pp. 17–20. DOI: 10.1103/PhysRevLett.72.17. eprint: hep-ph/9303287.

D'Odorico, V. et al. (2010). "The rise of the C iv mass density at z = 2.5". In: MNRAS 401, pp. 2715–2721. DOI: 10.1111/j.1365-2966.2009.15856.x. arXiv: 0910.2126 [astro-ph.CO].

D'Odorico, V. et al. (2013). "Metals in the IGM approaching the re-ionization epoch: results from X-shooter at the VLT". In: MNRAS 435, pp. 1198–1232. DOI: 10.1093/mnras/stt1365. arXiv: 1306.4604.

Du, X., C. Behrens, and J. C. Niemeyer (2017). "Substructure of fuzzy dark matter haloes". In: *Monthly Notices of the Royal Astronomical Society* 465, pp. 941–951. DOI: 10.1093/mnras/stw2724. arXiv: 1608.02575.

Duncan, K. et al. (2014). "The mass evolution of the first galaxies: stellar mass functions and star formation rates at $4 < z < 7$ in the CANDELS GOODS-South field". In: MNRAS 444, pp. 2960–2984. DOI: 10.1093/mnras/stu1622. arXiv: 1408.2527.

Dunlop, J. S. (2013). "Observing the First Galaxies". In: *The First Galaxies*. Ed. by T. Wiklind, B. Mobasher, and V. Bromm. Vol. 396. Astrophysics and Space Science Library, p. 223. DOI: 10.1007/978-3-642-32362-1_5. arXiv: 1205.1543.

Esa (2017). *Planck and the Cosmic Microwave Background*. URL: http://www.esa.int/var/esa/storage/images/esa_multimedia/images/2013/03/planck_cmb/12583930-4-eng-GB/Planck_CMB.jpg (visited on 10/06/2017).

Fields, B. D. (2011). "The Primordial Lithium Problem". In: *Annual Review of Nuclear and Particle Science* 61, pp. 47–68. DOI: 10.1146/annurev-nucl-102010-130445. arXiv: 1203.3551 [astro-ph.CO].

Garrison-Kimmel, S. et al. (2013). "Can feedback solve the too-big-to-fail problem?" In: *Monthly Notices of the Royal Astronomical Society* 433, pp. 3539–3546. DOI: 10.1093/mnras/stt984. arXiv: 1301.3137 [astro-ph.CO].

Giocoli, C. et al. (2010). "The substructure hierarchy in dark matter haloes". In: MNRAS 404, pp. 502–517. DOI: 10.1111/j.1365-2966.2010.16311.x. arXiv: 0911.0436.

González, V. et al. (2011). "Evolution of Galaxy Stellar Mass Functions, Mass Densities, and Mass-to-light Ratios from z ˜ 7 to z ˜ 4". In: ApJl 735, L34, p. L34. DOI: 10.1088/2041-8205/735/2/L34. arXiv: 1008.3901 [astro-ph.CO].

Grazian, A. et al. (2015). "The galaxy stellar mass function at $3.5 \leq z \leq 7.5$ in the CANDELS/UDS, GOODS-South, and HUDF fields". In: A&A 575, A96, A96. DOI: 10.1051/0004-6361/201424750. arXiv: 1412.0532.

Greif, T. H. et al. (2007). "The First Supernova Explosions: Energetics, Feedback, and Chemical Enrichment". In: ApJ 670, pp. 1–14. DOI: 10.1086/522028. arXiv: 0705.3048.

Hasegawa, K. and B. Semelin (2013). "The impacts of ultraviolet radiation feedback on galaxies during the epoch of reionization". In: MNRAS 428, pp. 154–166. DOI: 10.1093/mnras/sts021. arXiv: 1209.4143.

Hogg, D. W. et al. (2002). "The K correction". In: *ArXiv Astrophysics e-prints*. eprint: astro-ph/0210394.

Hu, W., R. Barkana, and A. Gruzinov (2000). "Fuzzy Cold Dark Matter: The Wave Properties of Ultralight Particles". In: *Physical Review Letters* 85, pp. 1158–1161. DOI: 10.1103/PhysRevLett.85.1158. eprint: astro-ph/0003365.

Hui, L. et al. (2017). "Ultralight scalars as cosmological dark matter". In: *Physical Review D* 95.4, 043541, p. 043541. DOI: 10.1103/PhysRevD.95.043541. arXiv: 1610.08297.

Inoue, K. T. et al. (2015). "Constraints on warm dark matter from weak lensing in anomalous quadruple lenses". In: *Monthly Notices of the Royal Astronomical Society* 448, pp. 2704–2716. DOI: 10.1093/mnras/stv194. arXiv: 1409.1326.

Iršič, V. et al. (2017). "New Constraints on the free-streaming of warm dark matter from intermediate and small scale Lyman-α forest data". In: *ArXiv e-prints*. arXiv: 1702.01764.

Ishigaki, M. et al. (2017). "Full-Data Results of Hubble Frontier Fields: UV Luminosity Functions at $z \sim 6 - 10$ and a Consistent Picture of Cosmic Reionization". In: *ArXiv e-prints*. arXiv: 1702.04867.

IYE, Masanori (2011). "Subaru studies of the cosmic dawn". In: *Proceedings of the Japan Academy Series B,Physical and Biological Sciences* 87.

Jethwa, P., V. Belokurov, and D. Erkal (2016). "The upper bound on the lowest mass halo". In: *ArXiv e-prints*. arXiv: 1612.07834.

Keating, L.C. et al. (2016). "Testing the effect of galactic feedback on the IGM at z $\sim$ 6 with metal-line absorbers". In: MNRAS 461, pp. 606–626. DOI: 10.1093/mnras/stw1306. arXiv: 1603.03332.

Kennedy, R. et al. (2014). "Constraining the warm dark matter particle mass with Milky Way satellites". In: *Monthly Notices of the Royal Astronomical Society* 442, pp. 2487–2495. DOI: 10.1093/mnras/stu719. arXiv: 1310.7739.

Klypin, A. et al. (1999). "Where Are the Missing Galactic Satellites?" In: *The Astrophysical Journal* 522, pp. 82–92. DOI: 10.1086/307643. eprint: astro-ph/9901240.

Koposov, S. E. et al. (2009). "A Quantitative Explanation of the Observed Population of Milky Way Satellite Galaxies". In: *The Astrophysical Journal* 696, pp. 2179–2194. DOI: 10.1088/0004-637X/696/2/2179. arXiv: 0901.2116.

Kroupa, P. (2002). "The Initial Mass Function of Stars: Evidence for Uniformity in Variable Systems". In: *Science* 295, pp. 82–91. DOI: 10.1126/science.1067524. eprint: astro-ph/0201098.

Labbé, I. et al. (2010a). "Star Formation Rates and Stellar Masses of z = 7-8 Galaxies from IRAC Observations of the WFC3/IR Early Release Science and the HUDF Fields". In: ApJl 716, pp. L103–L108. DOI: 10.1088/2041-8205/716/2/L103. arXiv: 0911.1356 [astro-ph.CO].

Labbé, I. et al. (2010b). "Ultradeep Infrared Array Camera Observations of Sub-L* z ˜ 7 and z ˜ 8 Galaxies in the Hubble Ultra Deep Field: the Contribution of Low-Luminosity Galaxies to the Stellar Mass Density and Reionization". In: ApJl 708, pp. L26–L31. DOI: 10.1088/2041-8205/708/1/L26. arXiv: 0910.0838 [astro-ph.CO].

Labbe, I. et al. (2013). "The Spectral Energy Distributions of z $\sim$ 8 Galaxies from the IRAC Ultra Deep Fields: Emission Lines, Stellar Masses, and Specific Star Formation Rates at 650 Myr". In: *Astrophysical Journal letters* 777, L19, p. L19. DOI: 10.1088/2041-8205/777/2/L19. arXiv: 1209.3037 [astro-ph.CO].

Lacey, C. and S. Cole (1993). "Merger rates in hierarchical models of galaxy formation". In: MNRAS 262, pp. 627–649. DOI: 10.1093/mnras/262.3.627.

Lee, K.S. et al. (2012). "How Do Star-forming Galaxies at z $\sim$ 3 Assemble Their Masses?" In: ApJ 752, 66, p. 66. DOI: 10.1088/0004-637X/752/1/66. arXiv: 1111.1233.

Leitherer, C. et al. (1999). "Starburst99: Synthesis Models for Galaxies with Active Star Formation". In: ApJS 123, pp. 3–40. DOI: 10.1086/313233. eprint: astro-ph/9902334.

Livermore, R. C., S. L. Finkelstein, and J. M. Lotz (2017). "Directly Observing the Galaxies Likely Responsible for Reionization". In: ApJ 835, 113, p. 113. DOI: 10.3847/1538-4357/835/2/113. arXiv: 1604.06799.

Lopez-Honorez, L. et al. (2017). "Constraints on warm dark matter from the ionization history of the Universe". In: *ArXiv e-prints*. arXiv: 1703.02302.

Mac Low, M.-M. and A. Ferrara (1999). "Starburst-driven Mass Loss from Dwarf Galaxies: Efficiency and Metal Ejection". In: ApJ 513, pp. 142–155. DOI: 10.1086/306832. eprint: astro-ph/9801237.

Macciò, A. V. et al. (2012). "Cores in warm dark matter haloes: a Catch 22 problem". In: *Monthly Notices of the Royal Astronomical Society* 424, pp. 1105–1112. DOI: 10.1111/j.1365-2966.2012.21284.x. arXiv: 1202.1282.

Madau, P. and M. Dickinson (2014). "Cosmic Star-Formation History". In: ARA&A 52, pp. 415–486. DOI: 10.1146/annurev-astro-081811-125615. arXiv: 1403.0007.

Madau, P. and T. Fragos (2017). "Radiation Backgrounds at Cosmic Dawn: X-Rays from Compact Binaries". In: ApJ 840, 39, p. 39. DOI: 10.3847/1538-4357/aa6af9. arXiv: 1606.07887.

Madau, P., S. Shen, and F. Governato (2014). "Dark Matter Heating and Early Core Formation in Dwarf Galaxies". In: *The Astrophysical Journal* 789, L17, p. L17. DOI: 10.1088/2041-8205/789/1/L17. arXiv: 1405.2577.

McLeod, D. J., R. J. McLure, and J. S. Dunlop (2016). "The z = 9-10 galaxy population in the Hubble Frontier Fields and CLASH surveys: the z = 9 luminosity function and further evidence for a smooth decline in ultraviolet luminosity density at z$\geq$ 8". In: MNRAS 459, pp. 3812–3824. DOI: 10.1093/mnras/stw904. arXiv: 1602.05199.

McLure, R. J. et al. (2010). "Galaxies at z = 6-9 from the WFC3 IR imaging of the Hubble Ultra Deep Field". In: MNRAS 403, pp. 960–983. DOI: 10.1111/j.1365-2966.2009.16176.x. arXiv: 0909.2437 [astro-ph.CO].

McLure, R. J. et al. (2013). "A new multifield determination of the galaxy luminosity function at z = 7-9 incorporating the 2012 Hubble Ultra-Deep Field imaging". In: MNRAS 432, pp. 2696–2716. DOI: 10.1093/mnras/stt627. arXiv: 1212.5222 [astro-ph.CO].

Menci, N. et al. (2016a). "A Stringent Limit on the Warm Dark Matter Particle Masses from the Abundance of z = 6 Galaxies in the Hubble Frontier Fields". In: *The Astrophysical Journal* 825, L1, p. L1. DOI: 10.3847/2041-8205/825/1/L1. arXiv: 1606.02530.

Menci, N. et al. (2016b). "Constraining the Warm Dark Matter Particle Mass through Ultra-deep UV Luminosity Functions at z=2". In: *The Astrophysical Journal* 818, 90, p. 90. DOI: 10.3847/0004-637X/818/1/90. arXiv: 1601.01820.

Moore, B. et al. (1999a). "Cold collapse and the core catastrophe". In: *Monthly Notices of the Royal Astronomical Society* 310, pp. 1147–1152. DOI: 10.1046/j.1365-8711.1999.03039.x. eprint: astro-ph/9903164.

Moore, B. et al. (1999b). "Dark Matter Substructure within Galactic Halos". In: *The Astrophysical Journal* 524, pp. L19–L22. DOI: 10.1086/312287. eprint: astro-ph/9907411.

Murray, S. G., C. Power, and A. S. G. Robotham (2013). "HMFcalc: An online tool for calculating dark matter halo mass functions". In: *Astronomy and Computing* 3, pp. 23–34. DOI: 10.1016/j.ascom.2013.11.001. arXiv: 1306.6721 [astro-ph.CO].

Navarro, J. F., C. S. Frenk, and S. D. M. White (1996). "The Structure of Cold Dark Matter Halos". In: *The Astrophysical Journal* 462, p. 563. DOI: 10.1086/177173. eprint: astro-ph/9508025.

Nomoto, K. et al. (2006). "Nucleosynthesis yields of core-collapse supernovae and hypernovae, and galactic chemical evolution". In: *Nuclear Physics A* 777, pp. 424–458. DOI: 10.1016/j.nuclphysa.2006.05.008. eprint: astro-ph/0605725.

Oesch, P. A. et al. (2010). "z ~ 7 Galaxies in the HUDF: First Epoch WFC3/IR Results". In: ApJl 709, pp. L16–L20. DOI: 10.1088/2041-8205/709/1/L16. arXiv: 0909.1806 [astro-ph.CO].

Oesch, P. A. et al. (2013). "Probing the Dawn of Galaxies at z ~ 9-12: New Constraints from HUDF12/XDF and CANDELS data". In: ApJ 773, 75, p. 75. DOI: 10.1088/0004-637X/773/1/75. arXiv: 1301.6162 [astro-ph.CO].

Oesch, P. A. et al. (2014). "The Most Luminous z ~ 9-10 Galaxy Candidates Yet Found: The Luminosity Function, Cosmic Star-formation Rate, and the First Mass Density Estimate at 500 Myr". In: ApJ 786, 108, p. 108. DOI: 10.1088/0004-637X/786/2/108. arXiv: 1309.2280.

Oppenheimer, B. D., R. Davé, and K. Finlator (2009). "Tracing the re-ionization-epoch intergalactic medium with metal absorption lines". In: MNRAS 396, pp. 729–758. DOI: 10.1111/j.1365-2966.2009.14771.x. arXiv: 0901.0286.

Pacucci, F., A. Mesinger, and Z. Haiman (2013). "Focusing on warm dark matter with lensed high-redshift galaxies". In: *Monthly Notices of the Royal Astronomical Society* 435, pp. L53–L57. DOI: 10.1093/mnrasl/slt093. arXiv: 1306.0009 [astro-ph.CO].

Parkinson, H., S. Cole, and J. Helly (2008). "Generating dark matter halo merger trees". In: MNRAS 383, pp. 557–564. DOI: 10.1111/j.1365-2966.2007.12517.x. arXiv: 0708.1382.

Peñarrubia, J. et al. (2012). "The Coupling between the Core/Cusp and Missing Satellite Problems". In: *The Astrophysical Journal* 759, L42, p. L42. DOI: 10.1088/2041-8205/759/2/L42. arXiv: 1207.2772.

Pettini, M. et al. (2003). "The C IV Mass Density of the Universe at Redshift 5". In: ApJ 594, pp. 695–703. DOI: 10.1086/377043. eprint: astro-ph/0305413.

Planck Collaboration et al. (2016). "Planck 2015 results. XIII. Cosmological parameters". In: A&A 594, A13, A13. DOI: 10.1051/0004-6361/201525830. arXiv: 1502.01589.

Press, W. H. and P. Schechter (1974). "Formation of Galaxies and Clusters of Galaxies by Self-Similar Gravitational Condensation". In: ApJ 187, pp. 425–438. DOI: 10.1086/152650.

Ryan-Weber, E. V. et al. (2009). "A downturn in intergalactic CIV as redshift 6 is approached". In: MNRAS 395, pp. 1476–1490. DOI: 10.1111/j.1365-2966.2009.14618.x. arXiv: 0902.1991 [astro-ph.CO].

Salpeter, E. E. (1955a). "The Luminosity Function and Stellar Evolution." In: ApJ 121, p. 161. DOI: 10.1086/145971.

— (1955b). "The Luminosity Function and Stellar Evolution." In: ApJ 121, p. 161. DOI: 10.1086/145971.

Schechter, P. (1976). "An analytic expression for the luminosity function for galaxies." In: ApJ 203, pp. 297–306. DOI: 10.1086/154079.

Schneider, A. et al. (2014). "Warm dark matter does not do better than cold dark matter in solving small-scale inconsistencies". In: *Monthly Notices of the Royal Astronomical Society* 441, pp. L6–L10. DOI: 10.1093/mnrasl/slu034. arXiv: 1309.5960.

Schultz, C. et al. (2014). "The high-z universe confronts warm dark matter: Galaxy counts, reionization and the nature of dark matter". In: *Monthly Notices of the Royal Astronomical Society* 442, pp. 1597–1609. DOI: 10.1093/mnras/stu976. arXiv: 1401.3769.

Sheth, R. K., H. J. Mo, and G. Tormen (2001). "Ellipsoidal collapse and an improved model for the number and spatial distribution of dark matter haloes". In: MNRAS 323, pp. 1–12. DOI: 10.1046/j.1365-8711.2001.04006.x. eprint: astro-ph/9907024.

Silk, J. (2017). "Feedback by Massive Black Holes in Dwarf Galaxies". In: *ArXiv e-prints*. arXiv: 1703.08553.

Silk, J., A. Di Cintio, and I. Dvorkin (2013). "Galaxy formation". In: *ArXiv e-prints*. arXiv: 1312.0107 [astro-ph.CO].

Silk, J. and G. A. Mamon (2012). "The current status of galaxy formation". In: *Research in Astronomy and Astrophysics* 12, pp. 917–946. DOI: 10.1088/1674-4527/12/8/004. arXiv: 1207.3080 [astro-ph.CO].

Simcoe, R. A. et al. (2011). "Constraints on the Universal C IV Mass Density at z $\sim$ 6 from Early Infrared Spectra Obtained with the Magellan FIRE Spectrograph". In: ApJ 743, 21, p. 21. DOI: 10.1088/0004-637X/743/1/21. arXiv: 1104.4117.

Song, M. et al. (2016). "The Evolution of the Galaxy Stellar Mass Function at z = 4-8: A Steepening Low-mass-end Slope with Increasing Redshift". In: ApJ 825, 5, p. 5. DOI: 10.3847/0004-637X/825/1/5. arXiv: 1507.05636.

Spergel, D. N. and P. J. Steinhardt (2000). "Observational Evidence for Self-Interacting Cold Dark Matter". In: *Physical Review Letters* 84, pp. 3760–3763. DOI: 10.1103/PhysRevLett.84.3760. eprint: astro-ph/9909386.

Springel, V. and L. Hernquist (2003). "Cosmological smoothed particle hydrodynamics simulations: a hybrid multiphase model for star formation". In: MNRAS 339, pp. 289–311. DOI: 10.1046/j.1365-8711.2003.06206.x. eprint: astro-ph/0206393.

Stark, D. P. et al. (2013). "Keck Spectroscopy of 3 < z < 7 Faint Lyman Break Galaxies: The Importance of Nebular Emission in Understanding the Specific Star Formation Rate and

Stellar Mass Density". In: ApJ 763, 129, p. 129. DOI: 10.1088/0004-637X/763/2/129. arXiv: 1208.3529 [astro-ph.CO].

Steidel, C. C. et al. (1999). "Lyman-Break Galaxies at z$\sim$4 and the Evolution of the Ultraviolet Luminosity Density at High Redshift". In: ApJ 519, pp. 1–17. DOI: 10.1086/307363. eprint: astro-ph/9811399.

Stoughton, C. et al. (2002). "Sloan Digital Sky Survey: Early Data Release". In: AJ 123, pp. 485–548. DOI: 10.1086/324741.

Susa, H. and M. Umemura (2004). "The Effects of Early Cosmic Reionization on the Substructure Problem in Galactic Halos". In: ApJl 610, pp. L5–L8. DOI: 10.1086/423199. eprint: astro-ph/0406305.

Tan, W.-W., F. Y. Wang, and K. S. Cheng (2016). "Constraining Warm Dark Matter Mass with Cosmic Reionization and Gravitational Waves". In: *The Astrophysical Journal* 829, 29, p. 29. DOI: 10.3847/0004-637X/829/1/29. arXiv: 1607.03567.

Tornatore, L. et al. (2007). "Chemical enrichment of galaxy clusters from hydrodynamical simulations". In: MNRAS 382, pp. 1050–1072. DOI: 10.1111/j.1365-2966.2007.12070.x. arXiv: 0705.1921.

Viel, M. et al. (2013). "Warm dark matter as a solution to the small scale crisis: New constraints from high redshift Lyman-α forest data". In: *Physical Review D* 88.4, 043502, p. 043502. DOI: 10.1103/PhysRevD.88.043502. arXiv: 1306.2314.

Weinberg, D. H. et al. (2015). "Cold dark matter: Controversies on small scales". In: *Proceedings of the National Academy of Science* 112, pp. 12249–12255. DOI: 10.1073/pnas.1308716112. arXiv: 1306.0913.

White, S. D. M. and M. J. Rees (1978). "Core condensation in heavy halos - A two-stage theory for galaxy formation and clustering". In: MNRAS 183, pp. 341–358. DOI: 10.1093/mnras/183.3.341.

Wright, E. L. (2006). "A Cosmology Calculator for the World Wide Web". In: PASP 118, pp. 1711–1715. DOI: 10.1086/510102. eprint: astro-ph/0609593.

XDF (2017). *The eXtreme Deep Field*. URL: http://xdf.ucolick.org/images.html (visited on 07/13/2017).

Yabe, K. et al. (2009). "The Stellar Populations of Lyman Break Galaxies at z $\sim$ 5". In: ApJ 693, pp. 507–533. DOI: 10.1088/0004-637X/693/1/507. arXiv: 0811.2041.